Physik-Department
Lehrstuhl für Experimentalphysik E21

Investigation of the chemical vicinity of defects in Mg and AZ31 with positron coincident Doppler broadening spectroscopy

Dissertation

Martin Stadlbauer

Fakultät für Physik der Technischen Universität München
Lehrstuhl für Experimentalphysik E21

Investigation of the chemical vicinity of defects in Mg and AZ31 with positron coincident Doppler broadening spectroscopy

Dipl.-Phys. Univ. Martin Stadlbauer

Vollständiger Abdruck der von der Fakultät für Physik der Technischen Universität München zur Erlangung des akademischen Grades eines

Doktors der Naturwissenschaften (Dr. rer. nat.)

genehmigten Dissertation.

Vorsitzender:		Univ.-Prof. Dr. Peter Vogl
Prüfer der Dissertation:	1.	Univ.-Prof. Dr. Klaus Schreckenbach
	2.	Univ.-Prof. Dr. Rudolf Gross

Die Dissertation wurde am 31.01.2008 bei der Technischen Universität München eingereicht und durch die Fakultät für Physik am 10.3.2008 angenommen.

Dedicated to my beloved parents

Ottilie Stadlbauer
Romuald Stadlbauer

Contents

Zusammenfassung

In der vorliegenden Arbeit wurden zwei Hauptziele erreicht: Erstens wurde das koinzidente Positronen Doppler Spektrometer (CDBS) an der hochintensiven Positronenquelle NEPOMUC aufwändig erweitert, um eine bessere Ortsauflösung für Messungen von zweidimensionalen Defektverteilungen zu erhalten und um Proben mit flachen Haftstellen für Positronen wie z. B. in Magnesium zu untersuchen. Zweitens wurde als Anwendung dieses Spektrometers die chemische Umgebung von Defekten in der industriell genutzten magnesiumbasierten Legierung AZ31 anhand von ionenbestrahlten Proben untersucht und mit SRIM-Simulationen verglichen. Der Einbau eines brillanzerweiternden Remoderators an NEPOMUC im April 2006 ermöglichte es erstmals, einen kleineren Positronenstrahlfokus zu erreichen, was aber eine komplette Neukonstruktion der Linsen und der Probenkammer des existierenden CDBS erforderlich machte. Basierend auf detaillierten Simulationen mit dem Finite-Elemente Programm COMSOL wurde der Strahldurchmesser am Probenort minimiert, um eine bessere Ortsauflösung zu erhalten. Erste Messungen mit dem umgebauten Spektrometer zeigten, dass verglichen mit der ersten Version des CDBS, welches im Rahmen einer Diplomarbeit entwickelt wurde, ein sechs mal kleinerer Strahlfokus erreicht werden konnte. Mit einem Wert von $0,3\,\mathrm{mm}$ wurde damit eine sub-mm Auflösung erzielt. Außerdem wurde das CDBS mit einem Kryostaten ausgestattet, um am Probenort Flüssigstickstofftemperatur zu erreichen, während die Probe im Vakuum für Messungen der lateralen Defektverteilungen gescannt werden kann. Damit wird die Untersuchung von flachen Positronhaftstellen ermöglicht.
Defekte und ihre chemische Umgebung in ionenbestrahltem Magnesium und der magnesiumbasierten Legierung AZ31 wurden dann auf atomarer Basis mit dem CDBS untersucht. In den entsprechenden Spektren muss die chemische Information sorgfältig vom Beitrag der Defekte getrennt werden. Dafür wurden Proben aus ausgeheiltem Mg mit Mg-Ionen bestrahlt, um ausschließlich Defekte zu erzeugen. Zusätzlich wurde eine Al- und Zn-Ionenbestrahlung an weiteren Mg-Proben durchgeführt, um den Einfluss sowohl der Defekte als auch der implantierten Ionen zu messen. Die bestrahlte Fläche der Proben wurde mit orts- und tiefenaufgelöster Doppler-Verbreiterungs-Spektroskopie (DBS) der Positronenannihilationsstrahlung untersucht und mit SRIM-Simulationen verglichen, wobei sich eine

exzellente Übereinstimmung ergab. Die Untersuchung der chemischen Umgebung von Defekten in AZ31 wurde mit CDBS an mit Mg-Ionen bestrahltem AZ31 durchgeführt. Der weit vom Maximum entfernt gelegene Teil der Annihilationslinie in diesen Proben wurde verglichen, welcher aufgrund des Beitrags von lokalisierten kernnahen Elektronen entsteht und somit ein für das jeweilige chemische Element charakteristisches Signal liefert. In diesen entsprechend normierten Spektren wurde kein Unterschied zwischen bestrahltem Mg und AZ31 gefunden, was zeigt, dass sich trotz der hohen Beweglichkeit von Defekten in AZ31 keine Cluster aus Legierungsbestandteilen und Defekten bilden, im Gegensatz zu z. B. Fe-Cu-Stählen, die unter Beschuss mit schnellen Neutronen zu einer Cu-Cluster-Bildung neigen. DBS und CDBS-Messungen an einer mit Zn-Ionen bestrahlten Mg-Probe bei Flüssigstickstofftemperatur führten dann zur Interpretation, dass wenigstens zwei unterschiedliche Defekttypen durch die Ionenbestrahlung erzeugt wurden.

Summary

Within the scope of the present work, two main goals have been achieved: Firstly, the coincident Doppler broadening spectrometer (CDBS) at the high intense positron source NEPOMUC has been elaborately improved in order to increase the spatial resolution for defect mapping measurements and to investigate samples with shallow positron trapping sites which are present e. g. in magnesium. Secondly, as an application, the chemical vicinity of defects in the industrially used magnesium based alloy AZ31 has been examined by means of the detailed investigation of ion-irradiated specimen with positron annihilation spectroscopy.
The installation of a brightness enhancing remoderation facility at NEPOMUC in April 2006 allowed to achieve a smaller positron beam focus and therefore the lens system and the sample chamber of the existing CDBS had to be completely redesigned. Detailed simulations with the finite-element simulation tool COMSOL were used to optimize the focal diameter of the positron beam at the sample position in order to increase the spatial resolution. First measurements of the spectrometer performance revealed a six times smaller focus compared to the first version of the CDBS, which was developed within a diploma thesis. With a value of 0.3 mm, sub-mm resolution has now been reached. The CDBS has been furthermore equipped with a sample cooling unit in order to reach liquid nitrogen temperature, maintaining the feature of scanning the sample for defect mapping. The investigation of shallow traps is therefore now possible.
Defects and their chemical surrounding in ion irradiated magnesium and the magnesium based alloy AZ31 were then investigated on an atomic scale with the CDBS. In the respective spectra the chemical information and the defect contribution have been thoroughly separated. For this purpose, samples of annealed Mg were irradiated with Mg-ions in order to create exclusively defects. In addition Al- and Zn-ion irradiations on Mg-samples were performed in order to create samples with both defects and impurity atoms. The ion irradiated area on the samples was investigated with laterally and depth resolved positron Doppler broadening spectroscopy (DBS) and compared with SRIM-simulations of the vacancy distribution. An excellent agreement was found. The investigation of the chemical vicinity of crystal defects in AZ31 was performed with CDBS on Mg-ion irradiated AZ31 with Mg-ion irradiated Mg. The outer tail of the energy distribution in the annihilation radiation

line in those samples was compared revealing the signal from the high momenta of inner shell electrons characteristic for the chemical element. In these spectra no difference was observed for properly normalized data between ion-irradiated Mg and AZ31. Despite the high defect mobility, no formation of solute-vacancy complexes was found due to the ion irradiation in contrast to for example Fe-Cu-alloys after fast neutron bombardment, where Cu-vacancy complexes are formed. DBS- as well as CDBS-measurements on a Zn-ion irradiated Mg-sample at liquid nitrogen temperature led to the educated guess that at least two different types of defects were produced by the irradiation procedure.

1 Introduction

Positron spectroscopy is a well-established tool to investigate lattice defects in solids [1, 2, 3, 4]. It has been widely used to investigate metals, alloys [5], semiconductors [6] and insulators [7]. Since positrons are trapped efficiently in most crystal defects [3], defect spectroscopy with positrons has gained more and more interest in condensed matter physics. During the last decade, Coincident Doppler Broadening Spectroscopy (CDBS) has become an important technique to distinguish between different elements in the vicinity of crystal defects [8, 9, 10]. Thus, for example the formation process of precipitates in alloys like nuclear reactor pressure vessel steels was successfully investigated in order to gain a deeper understanding of their embrittlement [11, 12]. It is also possible to monitor the formation of nanoclusters in binary alloys like Al-Sn during isochronal annealing [13].
After implantation into a sample, positrons thermalize within picoseconds and diffuse over hundreds of lattice spacings [4] until they annihilate with an electron either directly or after being trapped in crystal defects. In the center of mass system, two 511 keV γ-quanta are emitted in opposite directions, whereas in the lab system the electron momentum causes a deviation from the 180° angular correlation and an energy shift of the 511 keV-quanta due to the Doppler effect. The momentum of the thermalized positron is negligible.
The shape of the annihilation line reveals the electron momentum distribution at the annihilation sites. Electrons with 7.08 eV [14] at the Fermi-level in magnesium for example cause a Doppler shift of 1.3 keV of the emitted annihilation quanta whereas e.g. the localized core electrons in the 2s shell with an binding energy of 88.6 eV [15] lead to a larger Doppler shift of 4.8 keV. For this reason, regions of the annihilation line with high Doppler shifts represent the momentum distribution of localized core electrons and hence allow a distinction between different elements. Since positrons are efficiently trapped in crystal defects, their chemical vicinity can be therefore measured with high accuracy.
The present work focuses on the investigation of the chemical vicinity of defects in Mg and the Mg-based alloy AZ31 after defects have been created by ion implantation. Magnesium based alloys experience an increasing interest in industrial applications due to their low density and high rigidity. These features are not only crucial in car industry and aerospace engineering where energy efficiency enforces the use of light materials but also for the development of lightweight but durable portable electronic devices such as digital cameras, laptops and cell phones. The

mechanical properties of these materials are strongly correlated with the microscopic structure. Especially the chemical vicinity of open volume defects is of major interest since deviations from the stoichiometry lead to unfavorable precipitation processes and inhomogeneities. The wrought alloy AZ31, which consists of Mg with 3 wt. % Al and 1 wt. % Zn, is commonly used for lightweight metal sheets.
The respective measurements have been performed with the CDB-spectrometer at the high intense positron source NEPOMUC at the research reactor FRM-II Heinz Meier-Leibnitz [16]. This spectrometer was developed within the scope of a Diploma thesis [17] and first measurements of its performance and on thermally treated brass have shown its abilities [18]. Due to the installation of a luminosity enhancing remoderation device in 2006 and special demands related with the trapping of positrons in Mg, fundamental improvements of this spectrometer have become necessary.
Firstly the general properties of positrons and their most important applications in condensed matter physics are briefly reviewed. Then the Doppler broadening technique is elucidated in detail, followed by an elaborate description of the CDB-spectrometer at NEPOMUC and its improvement with all necessary simulations and measurements concerning its performance such as spatial resolution and achievable count rate. Doppler broadening and coincident Doppler broadening measurements at room temperature of Mg- and AZ31 samples irradiated with Mg-, Al- and Zn-ions are then presented. Firstly the irradiated region in the center of the samples is investigated with laterally resolved DB-measurements and compared with preceding SRIM-simulations of the produced defect distribution. Afterward, CDBS-measurements of ion irradiated Mg are presented in order to investigate whether the implanted ions form vacancy clusters and agglomerate in their vicinity. The respective spectra are used to analyze the CDB-spectra of Mg-ion irradiated AZ31, thus allowing a deeper insight into the chemical surrounding of the defects in this ternary alloy at room temperature. Finally DB- and CDB-measurements on a Zn-ion irradiated Mg-sample at liquid nitrogen temperature are presented which allow to draw conclusions concerning the produced defect structure followed by a conclusion and an outlook.

2 Positrons as microprobes in condensed matter physics

2.1 General properties of the positron

In 1930, P. A. M. Dirac postulated the positron as the antiparticle of the electron in order to explain negative energy states in his famous Dirac-equation which combines quantum mechanics with the theory of relativity [19].
Anderson experimentally discovered the positron two years later by investigating particle traces with a cloud chamber in a magnetic field. A lead plate inside the chamber was used to determine the direction of the observed traces, since the respective particles loose energy while passing through the plate. This energy loss and the thickness of the plate are directly correlated, such that the mass and the charge of the discovered particle can be determined by measuring the radii of the traces in front of and behind the plate. Due to the obtained values it became obvious, that they originated from a "positive electron" [20, 21, 22].
Electron and Positron as matter and antimatter particles have the same mass and spin, but opposite charge and magnetic moment. Both particles are stable in vacuum. Table 2.1 outlines the physical properties of the positron.

spin	1/2
rest mass	$m_0 = 0.0005485799092(4)\,\mathrm{u}$ [23]
rest energy	$E_0 = 510.998910(13)\,\mathrm{keV}$ [24]
charge	$q = 1.6021917(70) \cdot 10^{-19}\,\mathrm{C}$ [25]
magnetic moment	$\mu = 1.001159658(4) \cdot \mu_\mathrm{B}$ [25]
lifetime in vacuum	$> 2 \cdot 10^{21}\,\mathrm{a}$ [26]

Table 2.1: Physical properties of the positron.

In gases, at the surface of metals or in insulating materials positrons and electrons can form a hydrogen-like bound state which is called "positronium" or "Ps" [27, 28]. The reduced mass of this system amounts to $1/2\,\mathrm{m_e}$ and the distance scale is two times larger than in hydrogen. The ground state of Ps is either a spin-singlet (para Ps) with $m = 0$ or a triplet (ortho Ps) with $m = -1, 0, 1$ which annihilate due

to spin conservation into two or three gamma quanta respectively with lifetimes of roughly 100 ps and 140 ns [29].

2.2 Implantation of positrons into solids

2.2.1 Thermalization

If positrons of some keV energy are implanted into a solid they thermalize within several picoseconds. This is possible, since even for the positron sources with the currently highest available intensities (typically some $10^8\,\mathrm{s}^{-1}$ [30]) the average lifetime is still short enough and therefore the Pauli-principle does not have any influence (see also section 2.2.2). Various energy loss mechanisms contribute to this thermalization procedure depending on the energy of the positron during this process [3]. For the highest energies the dominating mechanism is ionization of the host atoms by collisions with localized core electrons [31]. In case of metals, electron-hole excitations become the predominant process for lower energies together with plasmon excitations above the respective energy threshold [32]. Finally, when the energy of the positron is reduced below roughly 50 meV, phonon scattering is the most important energy loss process.
A good approximation for the distribution of the implanted positrons is the Makhovian implantation profile which was originally set up for electrons [33, 3]. The transmission probability of the electrons (or positrons) is given as

$$\eta(z) \approx \exp\left[-\left(\frac{z}{z_0}\right)^m\right] \tag{2.1}$$

and hence the implantation profile results in

$$P(z) = \frac{\partial}{\partial z}\left[1-\eta(z)\right] = \frac{m z^{m-1}}{z_0^m}\exp\left[-\left(\frac{z}{z_0}\right)^m\right] \tag{2.2}$$

where m is a dimensionless parameter and z_0 is related to the mean penetration depth $\bar{z}$ by

$$z_0 = \frac{\bar{z}}{\Gamma\left[(1/m)+1\right]}\ . \tag{2.3}$$

$\Gamma(x)$ is the Gamma-function. The mean penetration depth is $\bar{z} = \frac{A}{\rho}E^n$ where A and n are material dependent parameters and the energy E is given in keV.
As an example, the respective values for aluminum are $A = 3.7\,\mu\mathrm{g/cm^2keV^{-n}}$,

$n = 1.67$ and $m = 1.92$ [34]. In figure 2.1 the Makhovian implantation profiles for positrons into aluminum with 9, 17 and 26 keV are plotted. With increasing implantation energy these profiles become broader which deteriorates the depth resolution in energy dependent measurements (see section 2.4 and chapter 3).

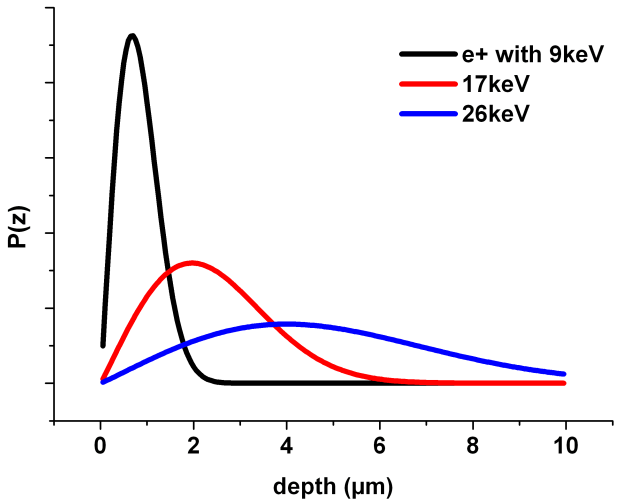

Figure 2.1: Makhovian implantation profile for positrons with various energies in aluminum.

2.2.2 Diffusion and trapping

As described above, positrons scatter mainly with phonons after thermalization. In metals the acoustic longitudinal phonons dominate this process [35]. The total diffusion length of a positron in a delocalized Bloch-state, i. e. in a defect free lattice, depends on the lifetime τ_{e^+} and on the diffusion constant D_+

$$L_+ = \sqrt{D_+ \cdot \tau_{e_+}} \ . \tag{2.4}$$

The diffusion constant D_+ is proportional to $T^{-1/2}$, since the contribution of phonon scattering drops with $T^{3/2}$ and the thermal energy of the positron is $3/2k_BT$ [3]. Consequently, the temperature dependence of the diffusion constant is described as follows:

$$D_+(T) = D_+(300K) \cdot \left(\frac{T}{300K}\right)^{-\frac{1}{2}} \tag{2.5}$$

with D_+ as theoretically determined and material-dependent parameter. The temperature dependent diffusion length of positrons in defect free magnesium is plotted in figure 2.2 with $D_+(300K) = 0.5\,\mathrm{cm}^2/\mathrm{s}$ for constant lifetime τ_{e^+} [36].

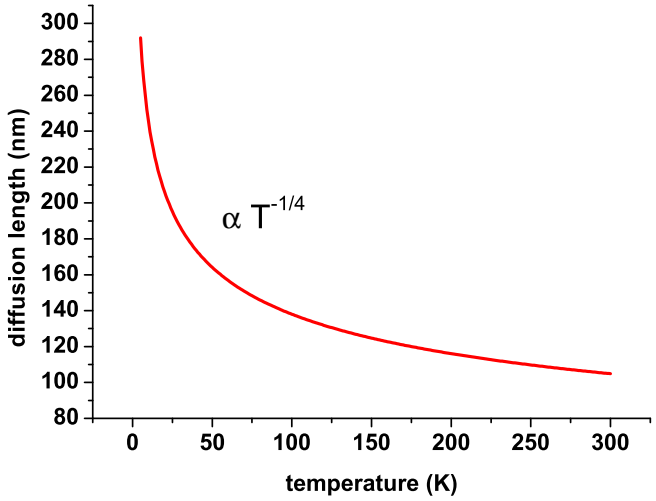

Figure 2.2: Diffusion length L_+ of positrons in defect free magnesium as a function of the temperature T in K as calculated in [36].

Many open volume defects such as vacancies or dislocations cause an attractive potential for the positrons due to the missing positive charge of the ion core. Therefore, the positron wave function is localized in such defects if its energy eigenvalue is lower than in the delocalized state. This mechanism is called "trapping" [3], during which the energy is transfered via phonon excitation to the crystal. In case of so-called shallow traps, like negatively charged ions in semiconductors or lattice distortions, a trapped positron can escape from the trap by thermal activation, called "detrapping". Consequently, if shallow traps are to be investigated, the temperature of the sample has to be reduced such that $3/2k_\mathrm{B}T$ drops below the depth of the trap.
The mathematical description of the trapping process is given by the trapping model with the following rate equations in case of a single defect type [37]:

$$\frac{df_\mathrm{b}}{dt} = -\lambda_\mathrm{b} f_\mathrm{b} - \kappa f_\mathrm{b} + f_\mathrm{i} \tag{2.6}$$

$$\frac{df_\mathrm{t}}{dt} = -\lambda_\mathrm{t} f_\mathrm{t} + \kappa f_\mathrm{b} \tag{2.7}$$

where f_b and f_t are the probabilities that the positron is in undisturbed lattice (bulk) or trapped at a certain time t. λ_b and λ_t represent the annihilation rates of free and trapped positrons, κ is the trapping rate and f_i denotes the number of positrons entering the sample per unit time. The model can be generalized with detrapping by introducing $-\eta f_\mathrm{t}$ with η as the detrapping rate.
The trapping rate is connected to the unitless defect concentration (number of defects per atom) via $\kappa = \nu c_\mathrm{t}$, where ν is the trapping coefficient. In principle, it is difficult to determine experimental values for κ and η since the absolute defect concentration is usually hard to measure. Theoretical models have shown, that the trapping coefficient for vacancies in metals lies in the range of 10^{14} to $10^{15}\,\mathrm{s}^{-1}$ [38]. It is therefore possible to detect monovacancy concentrations down to 10^{-7} per atom, since the trapping coefficient is five orders of magnitudes larger than the annihilation rate in the unperturbed lattice ($\tau_\mathrm{b} = 1 \cdot 10^{-10}\,\mathrm{s} = 1/\lambda_\mathrm{b}$) [3]. This enormous sensitivity is the main advantage of positron annihilation spectroscopy.
Table 2.2 gives an overview of typical time scales for positrons.

	Time	Reference
Scattering or diffraction	$\sim 10^{-15}\,\mathrm{s}$	[31]
Deceleration to Fermi energy	$\sim 10^{-13}\,\mathrm{s}$	[32]
Thermalization to $\sim \frac{3}{2}k_BT$	$\sim 10^{-12}\,\mathrm{s}$	[31]
Diffusion in bulk	$\sim 1 \cdot 10^{-10}\,\mathrm{s}$	[2]
Lifetime in monovacancies	$\sim 2 \cdot 10^{-10}\,\mathrm{s}$	[2]
Lifetime in vacancy clusters	$\sim 4 \cdot 10^{-10}\,\mathrm{s}$	[38]
Lifetime in surface states	$\sim 4 - 6 \cdot 10^{-10}\,\mathrm{s}$	[39]
Ps singlet (vacuum)	$\sim 1.25 \cdot 10^{-10}\,\mathrm{s}$	[40]
Ps triplet (vacuum)	$\sim 1.42 \cdot 10^{-7}\,\mathrm{s}$	[40]
Lifetime in vacuum	$> 2 \cdot 10^{21}\,\mathrm{a}$	[26]

Table 2.2: Time scales for positrons.

2.3 Annihilation and observables

Positrons annihilate either in bulk or in defects with differing lifetimes as described above in the trapping model. Due to the thermalization of the positron its momentum can be neglected in most cases.[1] Annihilation into one, two, three or more

[1] In case of trapping in defects with a deep well, the confinement of the positron leads to an uncertainty of its momentum due to the Heisenberg principle. It causes a so-called confinement peak in CDB-spectra which will be explained in section 3.3.

γ-quanta are in principle possible but the two photon decay is the most probable process. The cross section of the three photon decay is suppressed by a factor of $\alpha = 1/137$ due to the additional vertex in the Feynman-graph and is therefore two orders of magnitude smaller than the two photon decay. In case of the annihilation into a single γ-quantum a third particle such as a neighboring nucleus or an electron has to absorb the recoil momentum [2]. This process is very improbable, since in the respective qed-calculation for the cross section—besides the factor $\alpha = 1/137$ for every additional vertex in the Feynman-graph—an additional factor $\lambda_C^3 \rho$ has to be taken into account, where λ_C is the Compton wavelength of the electron and ρ denotes the density of surrounding atoms or electrons.
The following section will only deal with the two photon annihilation, since only this process is of relevance for the present work.

2.3.1 Positron lifetime

For low positron energies the cross section for annihilation is given by [2]:

$$\sigma = \frac{\pi r_0^2 c}{v} \tag{2.8}$$

and therefore the annihilation probability is

$$\Gamma = \sigma v n_\mathrm{e} = \pi r_0^2 c n_\mathrm{e} \tag{2.9}$$

with $r_0 = e^2/m_0 c^2$ as the classical electron radius and v as the velocity of the positron. As a consequence the positron lifetime $\tau = 1/\Gamma$ is inversely proportional to the electron density n_e at the annihilation site and independent from the velocity v. Due to this simple relation, different defect types like monovacancies, vacancy clusters or dislocations lead to a characteristic positron lifetime, and can therefore be distinguished [41]. The outstanding usefulness of positron lifetime measurements results from this feature. Nevertheless some drawbacks have to be put up with. Firstly, if several defect types are present, their differently pronounced contribution to the lifetime spectra necessitates a deconvolution including the background, the resolution function of the spectrometer and a possible influence of structure material in the vicinity of the positron source if it lies in the solid angle of the detector [42, 43, 44]. Secondly, a start signal is needed to measure the lifetime. It can be obtained either by using a ^{22}Na-source which emits a 1275 keV-photon simultaneously with the positron (see section 2.4.1) or by bunching a DC-positron beam [45]. Thirdly, due to the independence of the positron lifetime from the electron momentum, investigations of the chemical vicinity of defects are not possible with this technique.

2.3.2 Momentum-related observables

In the center of mass system of the moving electron-positron system, the emitted annihilation quanta are constrained to collinearity and an equally distributed total energy of $1022\,\mathrm{keV} - E_\mathrm{b}$ due to conservation of momentum and energy. E_b is the binding energy of the electron and the positron in the solid [46].
The transformation into the reference frame of the observer, i. e. the lab-system, leads to two experimentally accessible observables which can be used to determine the electron momentum distribution in the solid: a deviation from collinearity and a Doppler shift of the emitted γ-quanta (see figure 2.3).

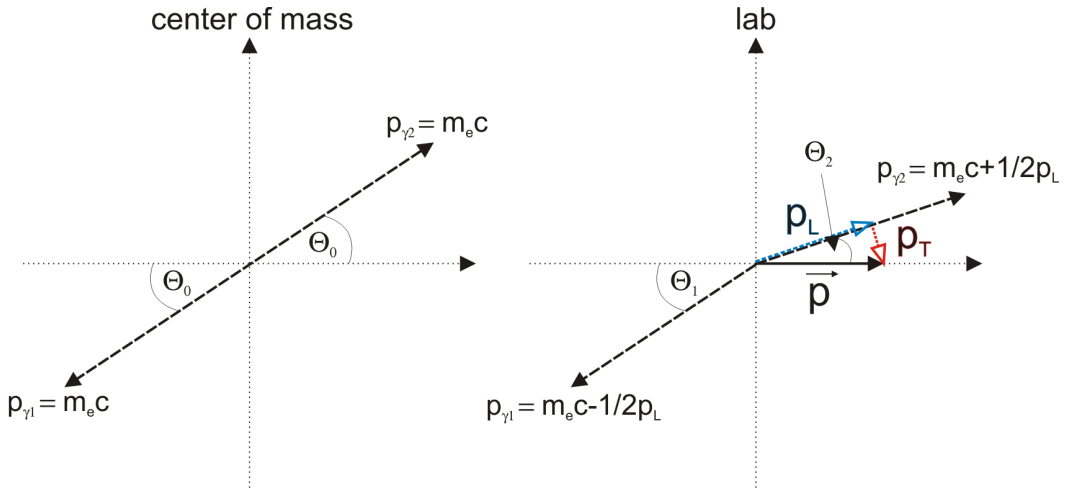

Figure 2.3: Momentum conservation

The deviation from collinearity—called Angular correlation of the annihilation radiation (ACAR)—results from the transversal momentum of the electron and can be directly derived from figure 2.3:

$$\sin \delta\theta = \sin\left(\Theta_1 - \Theta_2\right) \approx \Theta_1 - \Theta_2 \approx \frac{p_\mathrm{T}}{m_0 c} \,. \tag{2.10}$$

For example electrons from the Fermi surface of magnesium with an energy of 7.08 eV ($5.1 \cdot 10^{-3}\,\mathrm{m_0 c}$) lead to a deviation of 5.1 mrad for γ-emission perpendicular to the electron momentum [14]. Anger cameras are usually used as position sensitive detectors to measure 2D-ACAR [47]. In order to resolve the structure of the Fermi surface, a system resolution of $\delta\Theta \approx 0.5\,\mathrm{mrad}$ is needed and therefore the distance between the detector and the source has to be several meters, since the intrinsic resolution of an anger camera amounts to $\sim 4\mathrm{mm}$. Due to the resulting low count rates, long measurement times are necessary.
The longitudinal momentum of the electron-positron system causes a Doppler-

shift which is widely used to investigate the electron momentum distribution in the sample. A detailed description of this technique is given in chapter 3, since the measurements in the present work have been achieved by Doppler-broadening spectroscopy.

2.4 Positron beams

2.4.1 Production of positrons

Monoenergetic positron beams are available either as lab based systems with integrated intensities up to $10^6\,\mathrm{s}^{-1}$ or at large scale facilities with about a factor of 100 higher intensities [48]. The physical principle of positron production is different for both cases. Lab based beams use positrons from radioactive sources, and large scale facilities gain their high intensity from pair-production.

Radioactive isotopes

The most convenient way to produce positrons is to use β^+-emitting radioactive isotopes, which are neutron deficient and therefore decay according to ${}^A_Z X \rightarrow {}^A_{Z-1}Y + e^+ + \nu_e$. The energy from this decay is continuously distributed between positron and electron neutrino. Electron capture (EC) competes with this process and transforms a proton in the respective nucleus via $p + e^- \rightarrow n + \nu_\mathrm{e}$ into a neutron. The ratio between emitted positrons and the total number of conversions is called branching ratio. In order to obtain high-intense positron beams, isotopes with high branching ratios are favorable.
A very common one is ^{22}Na due to its long half life of 2.6 a, 90 % branching ratio and its commercial availability [49]. The endpoint energy of the emitted positrons amounts to 544 keV. A fast decaying but easy to produce isotope is ^{64}Cu ($T_{1/2} = 12.6\,\mathrm{h}$), since it can be obtained by irradiating ^{63}Cu with thermal neutrons in a research reactor [50].

Pair-production

Photons with energies above 1022 keV can be transformed via $\gamma \rightarrow e^+ + e^-$ into mass. The energy exceeding this value is arbitrarily transferred to both particles in order to fulfill conservation of energy. Due to momentum conservation, pair-production only takes place in the Coulomb field of another charged particle. In

the field of nuclei with the charge Ze, the cross section for pair-production below 20 MeV is approximately $\sigma \propto Z^2$ [51, 52]. Therefore, high-Z materials are advantageous as converter for the production of high intense positron beams.
Two basic setups allow the production of the necessary high intensity and energy γ-field. The first one uses a linear electron accelerator (LINAC), whose electron beam with energies of at least 100 MeV is focused on a target with an efficient heat sink [53, 54] where the stopped electrons produce bremsstrahlung. The second possible method is to use either directly the γ-radiation from a research reactor [55] or to convert the respective thermal neutrons via (n, γ)-reactions into high energy γ-radiation [16]. The latter design is based on a concept by B. Krusche and K. Schreckenbach [56].

2.4.2 Moderation and remoderation

Radioactive isotopes as well as accelerator or reactor driven sources emit a continuously distributed positron energy spectrum. The adjustment of the implantation profile for depth resolved measurements enforces the use of monoenergetic positrons. The usage of a simple $\mathbf{E} \times \mathbf{B}$-filter would reduce the phase space volume unacceptably [4]. A process called moderation overcomes this problem. Thermalized positrons can diffuse to the surface, if their thermalization site is close to the surface. Some metals like tungsten or platinum have a negative work function for positrons[2], which causes a reemission perpendicular to the surface with a sharp energy distribution only broadened due to thermal smearing. It is therefore possible to moderate positrons and to obtain a monoenergetic beam. Several different setups are possible. The most common ones are based on transmission or reflection geometries. In transmission moderators the positrons from the primary source penetrate a thin single or polycrystalline foil of the moderating material with several MeV energy (in case of for example isotope-based beams) and a certain fraction is reemitted on the opposite side with the respective work function of some eV [58]. The thickness of the moderator foil is adapted to the energy spectrum of the positron source and amounts typically to some µm [50]. In reflection geometry the positrons are reemitted from the moderator in the same half space where the source is located [59]. So-called self-moderated beams use only positrons which have been already moderated in the source material. This technique is applicable for pair-production sources, since some converter materials are also suited for moderation due to their negative work function. The efficiency of all above mentioned setups amounts to 10^{-3} at maximum.
In some cases an additional brightness enhancement of the positron beam is required if for example a small focus has to be achieved. The monoenergetic positron

[2]The work function for positrons in tungsten is -2.9 eV and for platinum -1.95 eV [57].

beam can be then remoderated with efficiencies up to 30 % [48]. Again, transmission and reflection geometries are possible setups [60, 61].
In order to increase the remoderation efficiency, positrons can be remoderated with gas at low pressures. A novel gas remoderation unit is being currently developed at NEPOMUC, which uses elastic scattering, vibrational/rotational excitations, electronic excitation and direct ionization in gases (e. g. nitrogen) at a pressure of ~ 0.1 mbar [62].

2.4.3 The high intensity positron beam NEPOMUC

In 2004, the intense positron source NEPOMUC at the nuclear research reactor Heinz Maier-Leibnitz (FRM-II) in Garching became operational. This source is based on the pair-production principle via the reaction $^{113}\mathrm{Cd}(\mathrm{n_{th}},\gamma)^{114}\mathrm{Cd}$ to produce γ-radiation. ^{113}Cd with a natural abundance of 12.2% has been chosen due to its high cross section of 26000 barn for thermal neutron capture. The deexcitation-energy of 9.05 MeV is released as a γ-cascade, where on average 2.3 γ's with energies higher than 1.5 MeV per captured thermal neutron are emitted [16].

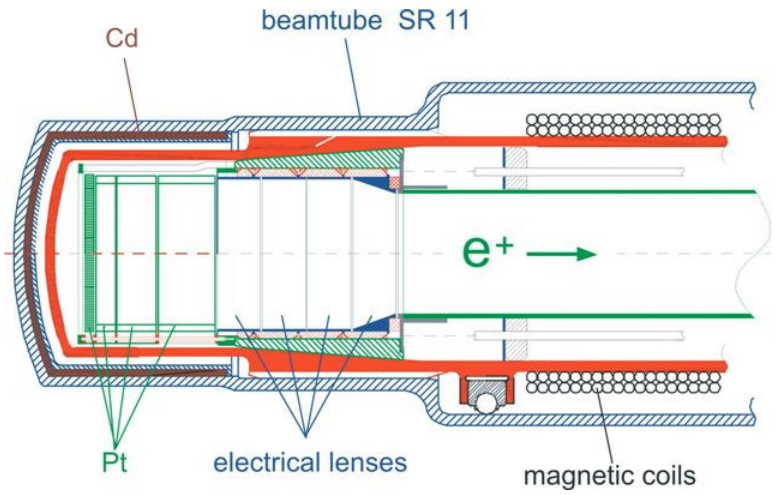

Figure 2.4: Design of the high intense positron source NEPOMUC. Thermal neutrons from the reactor excite ^{113}Cd which emits high energy γ-radiation. A honeycomblike platinum-structure converts the γ-quanta into positrons and moderates them. Electrical lenses are used to shape a beam which is then guided magnetically [63].

Figure 2.4 shows the general setup of the in-pile positron source NEPOMUC. Inside the beamtube SR11 at the research reactor FRM-II, a cadmium cap with 110 mm diameter and 95 mm length is installed near the maximum of the thermal neutron flux. The inner part contains an electrically insulated honeycomblike structure and several rings consisting of platinum which are used to convert the γ-radiation via

pair-production into positrons and electrons. They also serve as positron moderators. By applying a positive voltage between 15 V and 1 kV, the positrons are accelerated into a subsequent system of titanium lenses, which reduce the diameter of the positron beam and release it into a region with a magnetic guiding field of $\sim 6\,\mathrm{mT}$ [64].
The beam is then guided through three bendings in the concrete wall of the reactor pool in order to screen the accessible part of NEPOMUC from fast neutrons, γ-radiation, fast electrons and fast positrons. The intensity of the monoenergetic beam at the first accessible point amounts to $\sim 10^8\,\mathrm{e^+ s^{-1}}$ [30].
Until April 2007, all experiments at NEPOMUC have been performed with this primary moderated beam. Due to design challenges concerning radiation stability of the insulating materials near the reactor core and cooling of the platinum structure, which reaches a temperature of $\sim 350\,^\circ\mathrm{C}$ (radiation heating), the diameter of the positron beam was roughly 7 mm (FWHM) with an energy spread of $\sim 60\,\mathrm{eV}$ at 1 keV beam energy [65].
Since May 2007, a remoderation stage with a tungsten single crystal in reflection geometry has been installed with a total efficiency of 5% [61]. It decreases the beam diameter to $\sim 2\,\mathrm{mm}$ (FWHM), and the energy spread is reduced to the thermal energy spread of the remoderating tungsten crystal.

3 Doppler broadening spectroscopy of the positron annihilation radiation

3.1 Fundamentals

The annihilation of positrons with electrons leads to a Doppler shift of the annihilation radiation as already mentioned in section 2.3.2. It results from the transformation from the center of mass system of the electron-positron pair into the lab system (see also figure 2.3).
In the following section a general expression is derived which correlates the momentum of the annihilated electron with the Doppler-shift of the emitted γ-quanta[1].
If a source emits electromagnetic waves with a frequency of ν_0 and moves either toward (index 1) or away (index 2) from the observer, the formulas for the longitudinal Doppler effect are given as [66]

$$\nu_1 = \nu_0 \sqrt{\frac{c + v_\mathrm{l}}{c - v_\mathrm{l}}} \quad \text{and} \quad \nu_2 = \nu_0 \sqrt{\frac{c - v_\mathrm{l}}{c + v_\mathrm{l}}} \quad \text{respectively ,} \tag{3.1}$$

where v_l is the longitudinal velocity component of the source. For a transversal movement with respect to the emission direction of the electromagnetic waves, the transversal Doppler effect is described by

$$\nu' = \nu_0 \sqrt{1 - \frac{{v_\mathrm{t}}^2}{c^2}} \ , \tag{3.2}$$

with v_t as the transversal component of the velocity.
In the context of annihilation of electron and positron, ν_0 represents the frequency of the unshifted 511 keV-quanta and v_l and v_t the velocity components of the electron. The influence of the transversal and the longitudinal momentum of the electron are

[1] The velocity of the positron is neglected due to its thermalization.

determined via a first-order Taylor series approximation for small v_l and v_t, which results in

$$\nu_{1,2} = \nu_0 \pm \frac{\nu_0}{c} v_\mathrm{l} + \mathrm{O}(v_\mathrm{l}^2) \sim \nu_0 \left(1 \pm \frac{v_\mathrm{l}}{c}\right) \tag{3.3}$$

for the longitudinal contribution and

$$\nu' = \nu_0 + \mathrm{O}(v_\mathrm{t}^2) \sim \nu_0 \tag{3.4}$$

for the transversal part. The second order contribution in the latter case is $\frac{\nu_0 {v_t}^2}{2c^2}$ and consequently, the transversal momentum of the electron can be neglected, whereas the longitudinal momentum causes a pronounced Doppler shift.
In terms of total energy and momentum, the energy shift of the emitted photons is then given by

$$E_{1,2} = \frac{1}{2} E'_\mathrm{tot} \left(1 \pm \frac{p_\mathrm{l}}{2m_0 c}\right), \tag{3.5}$$

with $p_\mathrm{l} = 2m_0 v_\mathrm{l}$ as the longitudinal momentum of the electron-positron-system. The total energy E'_tot in the lab system results from the relativistic transformation $E'_\mathrm{tot} = E_\mathrm{tot}/\sqrt{1 - v^2/c^2}$ with $E_\mathrm{tot} = 2m_0c^2 - E_\mathrm{b}$ as the total rest energy minus the binding energy of the positron-electron-system in the solid. E_b is small for electrons with low momenta and plays only a role for localized electrons in shells with small main quantum number n [46].
Assuming that $E'_\mathrm{tot} \sim E_\mathrm{tot}$ and $E_b \sim 0$, the total energy of both emitted annihilation photons in the lab system follows from equation (3.5):

$$E_\mathrm{tot} = E_{\gamma_1} + E_{\gamma_2} = (511\,\mathrm{keV} - \Delta E)_1 + (511\,\mathrm{keV} + \Delta E)_2 = 1022\,\mathrm{keV}\ , \tag{3.6}$$

with $\Delta E = \frac{c p_\mathrm{l}}{2} = \sqrt{\frac{1}{2} E_0 E_\mathrm{kin,l}}$ as the Doppler-shift.
The annihilation line is symmetrically Doppler-broadened around the 511 keV-peak due to p_l. For example an electron moving with a kinetic energy of 10 eV along the direction of the photon emission causes a Doppler-shift of 1.6 keV.

Assuming a detector with infinitely good energy resolution, the intensity distribution depending on the measured Doppler-shift ΔE resulting from a free electron gas with the dispersion relation $E = \frac{\hbar^2 k^2}{2m}$ at $T = 0\,\mathrm{K}$ can be easily calculated. All

states in the reciprocal space from $p = 0$ up to the Fermi momentum $p = \hbar k_\mathrm{F}$ are occupied. The count rate in the ideal Doppler-detector per momentum interval Δp_l is then given as the volume of a disc perpendicular to the p_l-axis (see figure 3.1) for which $p_\mathrm{l} = \frac{2\Delta E}{c}$ is fulfilled. It results in

$$I(\Delta E) = \frac{dN}{d(\Delta E)} \propto \frac{\left(\hbar^2 {k_\mathrm{F}}^2 - {p_\mathrm{l}}^2\right) dp_\mathrm{l}}{d(\Delta E)} = \mathrm{const} \cdot \left(\hbar^2 {k_\mathrm{F}}^2 - \frac{4}{c^2}\Delta E^2\right) \ , \tag{3.7}$$

where N represents the number of occupied states. This equation shows that the projection of an isotropic momentum distribution in the reciprocal space onto the longitudinal component leads to a parabolic intensity dependence.

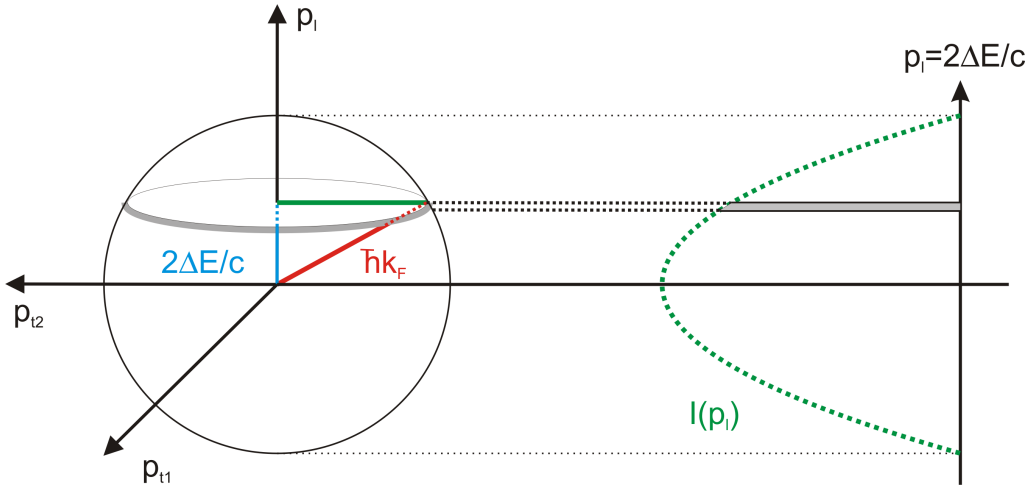

Figure 3.1: Projection of the momentum distribution of a free electron gas onto the longitudinal component p_l. The resulting intensity distribution I as a function of p_l or ΔE is negatively parabolic.

The model for a free electron gas is roughly applicable for conduction bands in metals and semiconductors in case of standard Doppler-broadening spectroscopy (see section 3.2), since in this case the energy resolution of the currently available detectors is to poor for resolving the structures near the border of the first Brillouin zone[2]. Therefore the conducting electrons of metals broaden the annihilation line as schematically shown in figure 3.1. The conduction band of magnesium for example results from the $3s^2$ electrons, whereas its valence band originates from the $2p^6$ orbitals.
The valence band can also be approximately described with a parabolic intensity

[2]This approximation is not longer valid, if a metallic single crystal is investigated with ACAR since the momentum resolution of ACAR is orders of magnitudes better than in Doppler-broadening measurements [2].

distribution. However, due to the larger binding energy, a stronger broadening of the annihilation line is observed.
Nevertheless, the contribution of localized core electrons can not be neglected, since their annihilation probability reaches up to several percents. In case of magnesium, the annihilation probability with $1s$ and $2s$ electrons as localized core electrons in the crystal is 0.032 and 1.56 % respectively [67]. Besides the main quantum number it also depends on the orbital shape and the crystal structure. Due to the higher binding energies of these electrons (for example 88.6 eV for the $2s$-electrons of magnesium), the above described parabolic broadening of the annihilation line is superimposed with a wide and non parabolic broadening, since the momentum distribution even of the s-orbital is non-parabolic. A detailed calculation of the contribution of valence and core electrons in copper and iron are presented in [68].

3.2 Doppler broadening spectroscopy - DBS

3.2.1 High resolution γ-spectroscopy with HPGe-detectors

In order to measure the broadening of the annihilation line, which lies in the range of some keV, γ-sensitive detectors with sufficient energy resolution are needed.
All γ-radiation detectors use the ionization capability of γ-quanta in matter to determine the energy deposited in the detector volume. Up to three processes occur, if a γ-quantum interacts with matter: photo effect, Compton effect and pair production. The latter one is not relevant for this work, since the energy of the annihilation radiation is well below the 1022 keV-threshold. The energy resolution of all kinds of γ-detectors depends among other influences like noise in the amplifier etc. mainly on the average number of primarily produced electron-ion or electron-hole pairs. In other words the energy resolution gets better, the less energy per ionization is necessary. Therefore, gas filled proportional counters with 15 to 30 eV ionization energy have a relatively poor energy resolution compared to semiconductor detectors, where only ~ 3 eV are needed per ionization[3] [69].
Semiconductor detectors are realized by producing a so-called PIN-junction with an intrinsic region between a positively and negatively doped contact. The thickness of the depletion zone, in which the electron-hole pairs are produced is proportional to $\sqrt{U/n}$, where n is the net impurity concentration and U the reverse bias voltage. Due to the minimum reachable impurity concentration in silicon and hence the limited maximum applicable bias voltage the maximum thickness of the depletion zone in a silicon pin-diode amounts to ~ 3 mm [70]. Consequently due to their

[3] Additionally, semiconductor detectors have a distinctively smaller so called Fano factor, which describes the variance in the number of produced charge carriers.

limited thickness, these detectors are only applicable for x-ray spectroscopy. In case of high energy γ-spectroscopy the efficiency would be less than a few %.
In contrary to that, germanium can be produced with much lower impurity concentrations compared to silicon and therefore thicknesses of depletion zones of several cm are achievable with bias voltages up to several kV, which allows the efficient detection of high energy γ-radiation. Commercially available high purity germanium detectors (HPGe-detectors) are capable to measure the 1.333 MeV γ-line of ^{60}Co with an absolute efficiency of several 10 % [70]. Due to the small band gap of $\sim$ 0.7 eV of germanium, thermal excitations at room temperature are not neglectable. The thermally excited charge carriers would lead to a destructive leakage current, if the high bias voltage is applied. To overcome this problem, the whole germanium crystal has to bee cooled to 77 K.
The energy resolution of these detectors varies with their efficiency. A detector with 30 % efficiency typically reaches for the ^{60}Co-line a resolution of $\sim$ 1.7 keV.
Measurements of the Doppler broadening of the positron annihilation line are usually performed with such detectors since these detectors achieve the best energy resolution of all γ-detectors.

3.2.2 The S-parameter: definition, error calculation and interpretation

The width of the annihilation line is correlated to the defect density in the sample material, due to the changing electron momentum distribution at the annihilation site [71]. Therefore a measurement parameter is defined in this section which is most commonly used to measure this width.
Since the energy resolution of high purity germanium detectors is of the same order of magnitude as the broadening, the measured annihilation lines are relatively featureless at least for low electron momenta, i. e. conduction electrons.
Figure 3.2 shows schematically the probability distribution of localized electrons in a perfect one dimensional crystal (the conduction electrons are not plotted in this picture). The thermalized positron is delocalized in a Bloch state due to the periodic potential and overlaps with the conduction electrons and also significantly with the wave functions of the localized core electrons. The latter ones lead to a relatively broad annihilation line since they are considerably faster than conduction and valence electrons as a consequence of their higher binding energy.
If there is a defect present within the diffusion region of the positron, it localizes at the defect site. Assuming an unchanged lattice constant, the annihilation probability with localized core electrons of the neighboring atoms is significantly reduced and therefore the annihilation line becomes more narrow resulting from the increased contribution of the slow conduction electrons. The corresponding spec-

trum is presented in figure 3.3 where the annihilation line of a defect rich material is plotted together with the one from an ideal crystal.

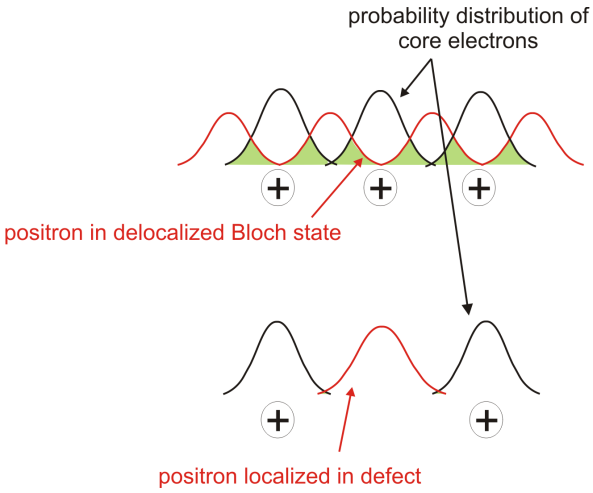

Figure 3.2: Schematic sketch of a delocalized positron in a Bloch state and the probability distribution of localized core electrons. The overlap between both decreases, if the positron localizes in a defect. If many defects are present, the contribution of high momentum electrons decreases which enables relative measurements of defect densities.

Since the annihilation line contains the information of the electron momentum distribution, a measurement parameter is required which determines the width of the annihilation line. Therefore the so called S-parameter is defined which represents the ratio between an arbitrarily chosen central region and the total count rate of the annihilation peak $S = \frac{A}{A+B}$(see figure 3.3) after subtraction of background (either linear or Compton-shaped). High S-values signal the presence of open volume defects whereas a defect free samples will show a low S-parameter.

In contrary to for example FWHM the S-parameter is more sensitive to the central region of the peak and therefore to the contribution of low momentum electrons [71]. A derivation of the statistical error of the S-parameter is given in appendix A. It amounts to

$$\Delta S = \sqrt{\frac{S(1-S)}{N}} \; . \tag{3.8}$$

The smallest error is achieved if $S = 0.5$ as explained in appendix A. Consequently the width of the central region $2E_S$ should be chosen such that the S-parameter values of a series of measurements are roughly 0.5 in order to obtain a maximum accuracy.
The energy resolution of γ-spectrometers with HPGe-detectors and the subsequent amplifiers depends strongly on the input count rate and the individual setup and

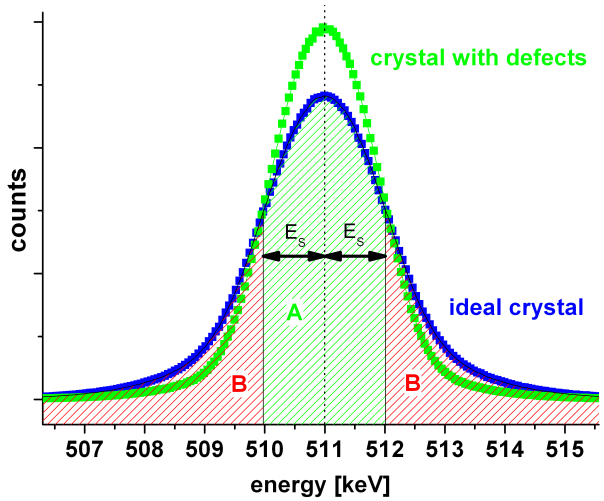

Figure 3.3: Definition of the S-parameter as a measure for the width of the annihilation line. An arbitrarily chosen central region is divided by the total number of counts such that values roughly around 0.5 are achieved (for details see text).

adjustment of the apparatus [72]. At high count rates, the resolving power of amplifiers or digital signal processors - both have been used in this project - deteriorates (see section 4). Since the energy resolution influences the peak width, the absolute values of S-parameter measurements are not comparable between different experimental setups. Therefore, the relative variations of the S-parameter are measured by comparing all results with the S-parameter of a reference sample. The width of the central region of the annihilation peak $2E_S$ as described in section 3.2.2 is chosen for one measurement of a series of measurements (for example the reference measurement), such that it equals to roughly 0.5 % due to error minimization. For all other measurements, E_S must not be modified.
The evaluation of the S-parameter has been performed with a program called MSPEC from Haaks [73]. It automatically determines the S-parameter of a series of measurements after E_S has been manually set with either a linear or a Compton-shaped background subtraction. The latter one is mathematically described as the convolution of a sharp step function due to small angle scattering in the detector surroundings with the shape of the resolution function of the Ge-detector which is well approximated with a Gauss distribution [74].

3.3 Coincident Doppler broadening spectroscopy - CDBS

The unique momentum distribution of localized core electrons allows to distinguish between different elements. Since positrons are efficiently trapped in defects, the chemical vicinity of them can be investigated (section 2.2.2).
The electron momentum distribution is in principle transfered to the shape of the annihilation line as described with equation (3.6). By analyzing its shape, the chemical surrounding of defects becomes accessible. Nevertheless such measurements are not possible with only one HPGe-detector due to distinctive contributions to the background, namely Compton scattering in the detector with escape of the scattered γ, incomplete charge collection and pile-up events. The first one results from γ-quanta, which reach the detector volume and get Compton-scattered, thus leading to an energy signal below 511 keV. Its contribution can be approximately described as a sharp step-function as mentioned in [74]. The second effect is called incomplete charge collection and is a consequence of charges, which haven't been fully swept to the electrodes of the detector. It affects the low energy side of the annihilation peak and is mathematically represented by an increasing exponential function convoluted with the detectors resolution function. The third background contribution comes from piled-up events and occurs, if two γ-quanta reach the detector within a very short period of time, such that the subsequent data acquisition system cannot distinguish between the respective signals. They are then counted as a single event with an energy above 511 keV and are described as a decreasing exponential function convoluted with the resolution function.
These background contributions bury most of the features of the annihilation peak and anticipate a more detailed analysis of the annihilation line except the determination of its width (see section 3.2.2). Moreover, the core annihilation probability lies typically in the range of a few % [67] and only the longitudinal projection of the electron momentum p_l in one dimension is determined by measuring the energy shift $\Delta E = \frac{cp_l}{2}$ of the emitted photons which causes the count rate to be low in the high momentum region.
By introducing a second HPGe-detector in collinear geometry, the background can be suppressed by many orders of magnitude [6]. Only events are taken into account, which are detected within a coincidence time window of for example 0.1 µs. These events are summed in a two dimensional plot, where the axes represent the energy scale of each detector respectively (see figure 3.4).

The position of the pixels in this figure represents the energies of the events detected in both detectors and the color indicates the number of counts. The annihilation peak is visible in the diagonal area which contains only events with a total energy of 1022 keV as described with equation (3.6). All events inside this region result from

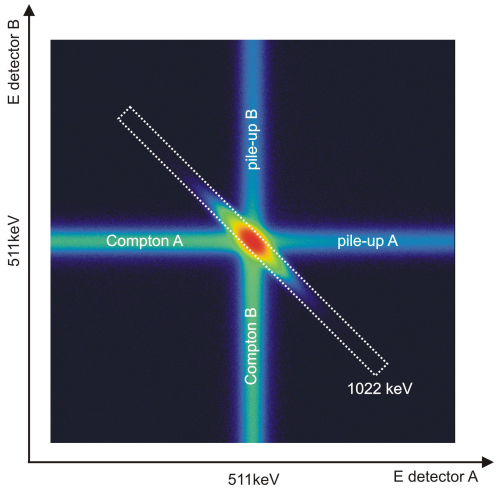

Figure 3.4: Two dimensional plot of two HPGe-detectors in coincidence analyzing the 511 keV-photopeak. The position of a pixel in this spectrum represents the energies of each detector and its color marks the number of counts. Besides the annihilation peak, a cross-like structure is visible. It results from Compton-scattered photons which have been observed by the respective detector and from piled-up events. The nearly background free diagonal area contains only events with a total energy of 1022 keV and is used for CDB-spectroscopy.

fully absorbed photons which have been detected accurately in the detectors and the subsequent signal chain. It is surrounded by a cross-like background-structure whose low energy parts stem from Compton-scattering in the sample or the detectors vicinity and incomplete charge collection whereas the events with energies above 511 keV result from pile-up.
By projecting the diagonal region onto one of the axes, a background free annihilation spectrum can be obtained. This technique is called coincident Doppler broadening spectroscopy or CDBS.

Data analysis of CDB-spectra

The projection of the annihilation line from the two dimensional plots as shown in figure 3.4 is performed by defining a diagonal region of interest (ROI) with a thickness, such that the contributions of the Compton and pile-up background can be neglected. All events within the ROI are then summed for constant channel (energy) in detector A or B, which equals a projection onto the respective energy axis. The projections in this work have been performed with the analyzing software MSPEC2D programmed by Haaks from HISKP in Bonn [73], using a total width of 1 keV for the ROIs.
In order to compare two materials, it is most convenient to chose a reference mate-

rial and to examine the relative differences between the respective spectra. This is done by normalizing the CDB-spectra of the reference material and the sample to equal area and to divide them by the reference spectrum channel by channel. The relative differences between both spectra appear then very distinctively as presented in figure 3.5. These curves are usually denoted as ratio curves or CDB-signatures. Assuming a symmetrical peak shape, the redshifted side is often mirrored at 511 keV and added to the blueshifted side in order to increase statistics.
The calculation of the error per channel (or energy) is performed with the Gaussian error propagation. A detailed description is given in appendix B.

Interpretation of CDBS-measurements

Although the unique electron momentum distribution of different elements allows in principle to distinguish between elements, an unambiguous assignment is often not possible, since the high momentum region of CDB-spectra is not only affected by the momentum distribution of the core electrons of a specific material, but also by the geometry of the annihilation site like the unperturbed lattice or defects. If a positron annihilates in a defect, the respective overlap of its wave function with the localized core electrons of the neighboring atoms changes distinctively and therefore alters the CDB-signature significantly in the high momentum region (i.e. high Doppler-shifts). Furthermore, the assumption, that a positron in a defect is fully thermalized is not necessarily true [75]. The confinement of positrons in potential barriers such as open volume defects results in a zero-point motion which blurs the Fermi cut off energy and causes so-called confinement peaks in the CDB-signatures when taking a defect free material as a reference. Consequently, the changes of the CDB-signatures in samples containing defects have to be thoroughly separated from the chemical contributions.
In principle there are two different possibilities to separate these contributions. Firstly, they can be separated by producing samples, were the possible origins of changes in the signature are separated from each other, i.e. a sample with only defects and one with defects and the chemical contribution. It is then possible to approach to the various influences experimentally. This technique has been applied in the present work [76].
Secondly, it is favorable to perform ab-initio calculations of the electron and positron momentum distribution, then projecting them onto the longitudinal momentum and convoluting this function with the resolution function of the measuring apparatus. In those theoretical considerations, the contributions of the lattice or defects and the chemical information can be separated. The comparison with CDB-experiments clarifies then the actual influences. In case of aluminum or Al-Mg-alloys this technique has been used successfully [75, 77]. But it is only practical, if the lattice structure of the investigated material is not too complex to simulate in ab-initio calculations. Therefore, it can not be satisfactorily applied to magnesium due to its hcp-structure [78].

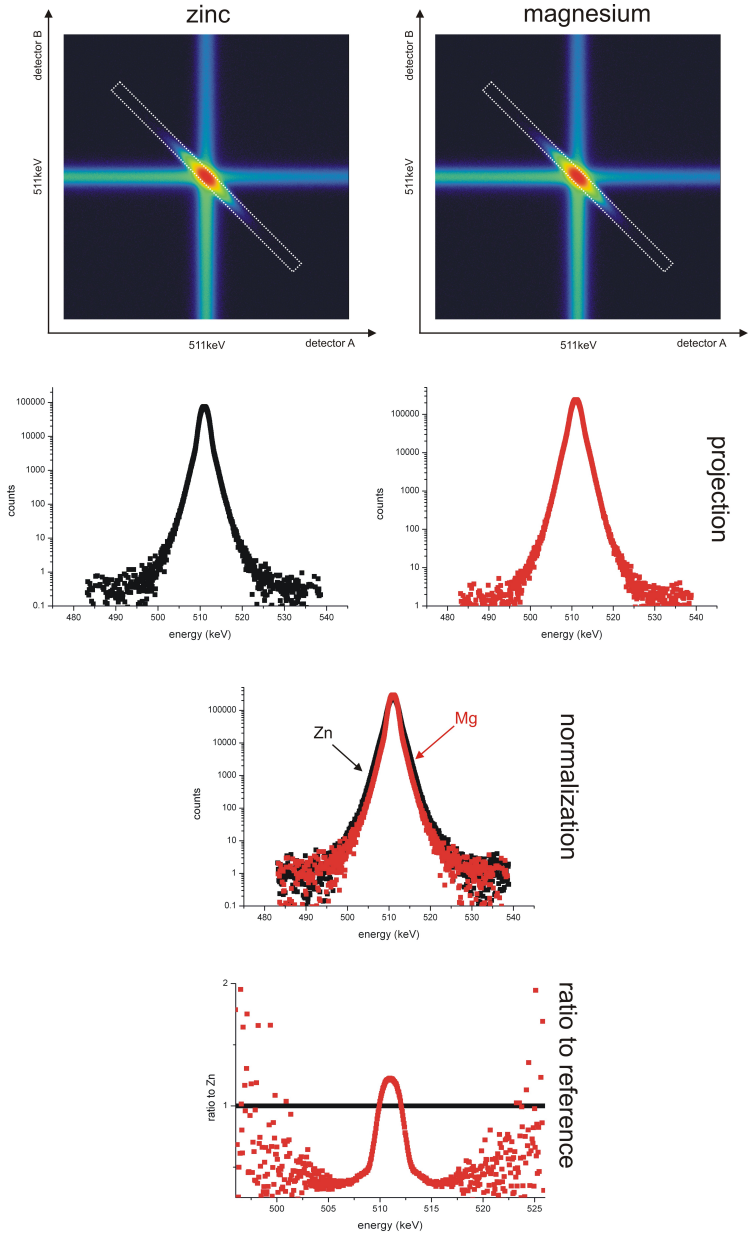

Figure 3.5: Coincident Doppler broadening spectra are analyzed by comparing them with a reference spectrum. In this case, the spectra of Zn and Mg are shown. Firstly, projections from the respective two dimensional spectra are obtained by using the projection tool MSPEC2D. Then, the curves are normalized to equal area and divided channel by channel through the reference spectrum. The characteristic fingerprint of Zn compared to Mg can be then observed very clearly.

4 CDB-spectrometry at NEPOMUC

In October 2004, a CDB-facility at the high intense positron source NEPOMUC was set into operation [17]. This first version of the CDB-spectrometer has been used for many measurements in this work after its characteristics have been extensively tested. Due to the installation of a remoderation facility at NEPOMUC, the spectrometer had to be redesigned. The following chapter describes firstly the measurements concerning the performance of the first version of the CDBS at NEPOMUC (CDBS1). Secondly, a motivation for the improvement of the CDBS1 is given followed by a description of the design of the new CDBS-version (CDBS2) with all necessary simulations.

4.1 Experimental setup of the CDBS1

A detailed description of the CDBS1 can be found in [17] including the design and all simulations. Figure 4.1 shows a schematic view of this spectrometer, which has been in operation until October 2007, when it was replaced by a newer version.
The energy of the primary positron beam provided by NEPOMUC can be adjusted between 15 and 1000 eV. Before the installation of the remoderation stage, the beam energy for CDBS-measurements was set to 1 keV. A longitudinal magnetic field guided the beam through an evacuated beam tube to the CDBS, which had an aperture at the entrance in order to reduce the beam diameter from 20 to 3 mm. Therefore, the beam intensity was decreased from $5 \cdot 10^8$ to roughly $5 \cdot 10^6$ positrons per second, otherwise the energy resolution of the high purity germanium detectors would have been deteriorated due to excessive count rates. In addition, the beam collimation facilitated the subsequent focusing onto the sample, which allowed spatial resolved measurements. Afterward, the beam was magnetically guided to the analysis chamber and non adiabatically released from the longitudinal field by a grounded magnetic field termination consisting of μ-metal. This termination was necessary, since the sample could be set to negative voltages down to −30 kV in order to adjust the mean positron penetration depth. The resulting focusing electrical field lead to an increase of the transversal momentum of the positron beam which would have caused a larger gyration radius an hence a poor focus if a magnetic field was present. In order to achieve a preferably discontinuous transition

from the magnetic guiding field to the field free chamber, the diameter of the field termination was only 3 mm (for a detailed explanation of the principle of magnetic field terminations, refer to section 4.3).
A subsequent electrical Einzel lens and the negative sample potential focused the divergent positron beam onto the sample [17, 18]. Therefore, the lens voltage had to be adjusted together with the sample potential. Samples of $20 \times 20\,\mathrm{mm}^2$ could be moved in x- and y-direction perpendicular to the beam axis with step motors in order to perform two dimensional scans. The sample potential was adjustable between 0 and 30 kV, thus resulting in a positron energy of 1 to 31 keV. Due to the potential at the moving sample, the positron beam had to be prevented from moving with the sample as a result of the resulting distortion of the electrical field. Therefore, a conductive plate beneath the sample was set to the same voltage, such that the shape of the electrical field remained constant independently from the sample holder position.
Two high purity germanium detectors in collinear geometry with an efficiency of 30% measured the annihilation radiation emitted from the sample with an energy resolution between 1.2 and 1.4 keV at 477.6 keV—this gamma energy is emitted from ^{7}Be and was used as a monitor line. The distance between sample and detector was adjustable between 60 and 370 mm. Single photopeak count rates up to 2×2500 cps were achievable without major decrease in energy resolution with an analog signal processing chain until May 2006. After installation of two digital signal processors (DSP 2060) [79] and detectors with transistor reset preamplifiers from Canberra a single photopeak count rate of up to ~ 5500 cps was reached. Both detectors were connected to the multiparameter system MPA3 from FastComTec for data processing [80].

4.2 Characterization of the beam parameters

In [17], the lens voltages as a function of the sample potential were derived from simulations with the particle tracing software SIMION [81]. In order to determine the beam diameter at the sample position experimentally, an aluminum sample with tungsten stripes on the surface was investigated with the CDBS1, since aluminum and tungsten exhibit distinctively different electron momentum distributions due to the higher binding energy of core electrons in W. The sample was moved in such a way that the positron beam crossed the sharp edge between Al and W, while recording the position dependent S-parameter. Due to the lateral extensions of the positron beam, these sharp edges become smooth transitions, whose derivatives allow to estimate the FWHM of the positron beam at the sample.
Since the SIMION-simulations in [17] were performed with an assumed positron beam divergence of 2.56 ° at 1 keV which has not been experimentally measured

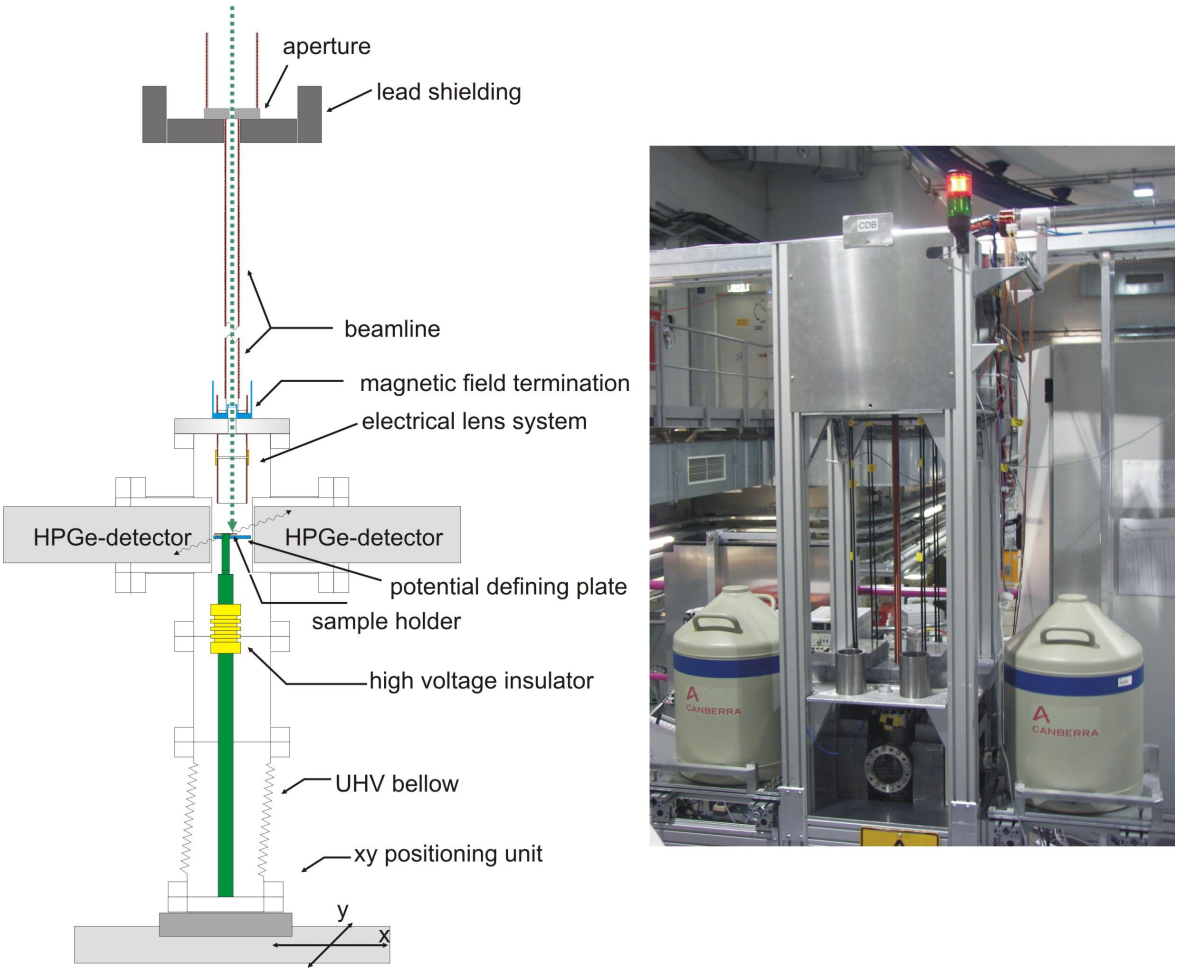

Figure 4.1: Left: Setup of the CDBS1 at NEPOMUC. The positrons are guided magnetically from above through an aperture to reduce the beam and then through a magnetic termination into the sample chamber. An electrical Einzel lens focuses the beam onto the sample which can be set to potentials from 0 down to −30 kV. To achieve spatial resolution, two step motors move the sample in x and y-direction. Two HPGe-detectors measure the annihilation radiation. Right: Picture of the CDBS1.

so far, the values for the lens potentials had to be verified and optimized. An automated routine was programmed, which firstly adjusted the sample potential, secondly set the lens voltage to $U_0 \pm \Delta U$ with $\Delta U \in \{-20\,\mathrm{V}, -10\,\mathrm{V}, 0\,\mathrm{V}, 10\,\mathrm{V}, 20\,\mathrm{V}\}$ with U_0 as determined in [17], and thirdly the sample was scanned in steps of 1 mm in x and then in y-direction over the respective Al-W-edge for each set of voltages. A small focus results in a steep slope of the transient curve. An exemplary measurement is shown in figure 4.2, where this measurement has been performed for −15 kV sample potential with $U_0 = 648\,\mathrm{V}$. This figure shows the measurement in x and y-direction on one single axis. The left transition has been measured in

x-direction and the right one in y. The steepness of the transient curves and their centers increase for lower lens potentials. The smallest focus has been achieved for 608 V lens voltage. Similar measurements have been performed for -1, -10, -20 and −25 kV sample potential and the optimal lens potential in each case has been determined. The set of sample and lens potentials has been fitted with

$$U_{\text{lens}} = 853.385 - 0.016 \cdot U_{\text{sample}} \tag{4.1}$$

with U_{sample} in V. All subsequent measurements with the CDBS1 have been performed with these lens potentials.

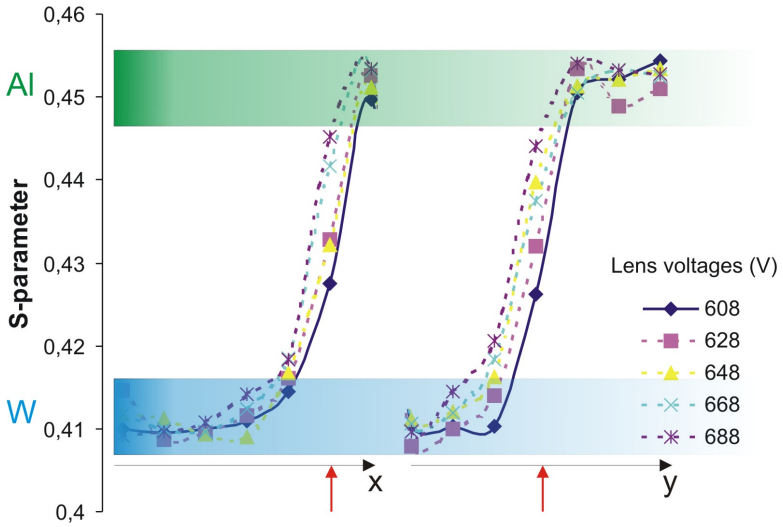

Figure 4.2: Variation of the lens potential while scanning over a Al-W-edge in x- and y-direction at −15 kV sample potential. The distance between the points amounts to 1 mm and the position of the respective edges is denoted with red arrows. The smallest focus has been achieved with 608 V lens voltage.

In order to characterize the beam diameter at various sample and lens potentials and to completely image the structure of the Al-W-sample, first two dimensional scans have been performed with the sample shown in figure 4.3, to ensure that the positron beam hits the sample at the desired position. The resulting S-parameter map is shown in figure 4.4 for the positron energies 2, 11, 19 and 27 keV, where the sample has been scanned with a step size of 1 mm from 1 to 18 mm in each direction [82]. The structure of the sample could be clearly reproduced. Nevertheless, for low positron energies, a focus of only 3.3 mm in y-direction was achievable. This is explained with the geometry of the sample chamber of the CDBS1. Since the grounded chamber together with the potential at the sample act as lenses, the

focusing effect becomes more dominant for lower sample potentials. The derivative of S-Parameter line scans for constant $x = 2.5\,\text{mm}$ and $y = 17.5\,\text{mm}$, respectively, and the FWHM of a Gaussian peak fitted into the resulting curve provide the projections of the beam dimensions in both directions. The results are given in table 4.1. The asymmetry between x- and y-direction is a consequence of the asymmetrically shaped sample chamber.

Figure 4.3: Al-sample with 5 mm wide W-stripes. The size of the sample is $20 \times 20\,\text{mm}$.

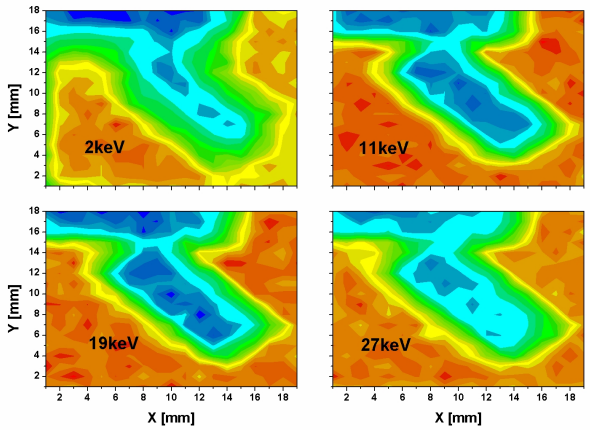

Figure 4.4: Two dimensional S-Parameter scan of the described Al-sample with tungsten stripes at various positron energies.

Table 4.1: Lateral resolution: FWHM of the derivative of S-parameter scans for various positron energies.

energy [keV]	x [mm], FWHM	y [mm], FWHM
2	2.30 ± 0.30	3.30 ± 0.51
11	2.38 ± 0.46	1.43 ± 0.13
19	2.57 ± 0.35	1.54 ± 0.19
27	2.38 ± 0.41	1.61 ± 0.16

The beam structure was investigated in more detail by comparing the S-parameter behavior at an Al-W-edge with a theoretically assumed shape of a Gauss distribution. Since the Gauss distribution is not analytically integrable, a matrix with a symmetrical three dimensional Gauss-function with the FWHM as free parameter has been summed column by column. It's equation is given by:

$$g(i,j) = \frac{1}{\sigma\sqrt{2\pi}} \exp\left[-\frac{1}{2\sigma^2}\left((i-x_0)^2 + (j-y_0)^2\right)\right] \tag{4.2}$$

where $\sigma = \frac{\mathrm{FWHM}}{2\sqrt{2\ln 2}}$ stands for the standard deviation depending on the FWHM. The matrix dimension was 500×500. In order to compare this theoretically assumed beam shape with measurements, a sample with perpendicular tungsten stripes was produced, where the positron beam was scanned at constant $x = 15\,\mathrm{mm}$ over the edge in y-direction from $y = 8$ to $16\,\mathrm{mm}$ with a step size of $1\,\mathrm{mm}$ and a positron energy of $20\,\mathrm{keV}$ (the Al-W-edge was located at $12\,\mathrm{mm}$). Consequently, each bin in the matrix equals to $8/500 = 0.016\,\mathrm{mm}$. To find the best fitting FWHM, the quadratic difference of the measured and the theoretically gained S-parameter curve has been calculated after normalization and minimized.[1] The result is plotted in figure 4.5 together with the least square fitted and integrated Gauss distribution with $\mathrm{FWHM} = 1.12\,\mathrm{mm}$.
The smaller value compared to the measurement in table 4.1 is easy to explain. In the first approach, the derivative of the S-parameter scan has been determined. In order to quantize the width of the beam, a Gauss function has been fitted into this curve. Since the positron beam is not perfectly Gauss-shaped, the FWHM is overestimated by the fitting procedure, whereas in the second approach an ideal curve resulting from a symmetrically shaped Gauss-beam has been fitted to the measured values. The deviations from the ideal Gauss-related curve show, that a small Gauss-shaped center is surrounded by a wider halo. However, this halo can be neglected, since the differences in the halo region (between 8 to 11 mm and 12.5 to 16 mm) amount only to 1/10 of the total deviation between Al and W.

4.3 Improvement of the CDB-spectrometer

The first version of the CDBS as described above has been used until August 2007. Several reasons induced a redesign of this spectrometer:

- The installation of the remoderation facility and a digital signal chain with higher data throughput enforced a new magnetic field termination without annihilation losses.

- In order to investigate magnesium with its shallow positron traps a sample cooling at least down to nitrogen temperature is necessary.

[1] In order to match the measured points with the 500 points of the theoretically assumed curve, the measured curve has been spline interpolated.

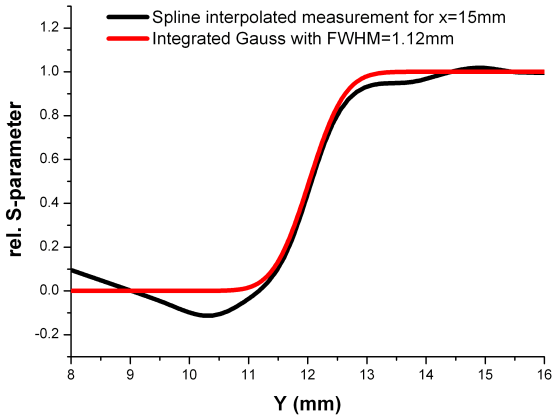

Figure 4.5: Spline interpolation of a S-parameter scan over an Al-W-edge at a positron energy of 20 keV and the expected curve from a homogeneously distributed Gauss shaped beam as determined with a least square fit of the FWHM = 1.12 mm. Apparently, the positron beam consists of a gaussian center with a wider halo as seen from the small deviations at the beam boundaries.

- The horizontally mounted detectors caused an asymmetry in two dimensional S-parameter scans and complicated the extension with more HPGe-detectors due to lack of space.

The following sections elucidate these items in more detail.

Magnetic field termination

As already mentioned in section 4.1, the entrance of the sample chamber of the CDBS1 was equipped with a grounded magnetic field termination with a small diameter of only 3 mm in order to achieve a discontinuously transition from the magnetic guiding field to the field free sample chamber. A detailed description of the fundamental principle of magnetic field terminations is given in section 4.3.1. Although an aperture reduced the diameter of the positron beam prior to the magnetic field termination many positrons still annihilated there. As a consequence, the maximum coincident photo peak count rate was only about 500 cps although the photo peak count rate in a single detector amounted to roughly 5500 cps with the DSP2060 digital signal processors. Assuming, that all detected events resulted from annihilation in the sample between the collinear detectors, one would expect $5500\,\text{cps} \cdot 0.25 \sim 1375\,\text{cps}$, with a peak/total efficiency of 25 % at 511 kV of the HPGe-detector. This discrepancy is explained by the fact, that most of the detected 511 keV photons originated from the annihilation at the magnetic field

termination and not from the sample. This loss in intensity was acceptable for the originally used HPGe-detectors, whose analogue signal chain allowed only moderate total count rates up to 10000 cps, since for higher count rates the energy resolution deteriorated. Within the scope of this work two new HPGe-detectors have been purchased with a digital signal chain, which allows an about three times higher data throughput without a major loss in resolution. In order to guide the positrons more efficiently to the sample, a change of the magnetic field termination became necessary.
Additionally in April 2006 a remoderation facility has been installed at NEPOMUC in order to increase the brightness of the positron beam. The primary 1 keV beam is therefore guided through a magnetic field termination into a μ-metal shielded housing, where electrical and magnetic lenses focus the beam onto a tungsten crystal. The remoderated positrons (see section 2.4.2) leave the tungsten crystal perpendicular to its surface with an energy of 2.9 eV. By applying a voltage between 20 and 200 V to the crystal, the energy of the remoderated beam can be adjusted. However, even for 200 eV beam energy, the focus diameter at the sample position of the CDBS1 increased to > 5 mm at 2 kV sample potential, since the condition for a non-adiabatically release was not longer fulfilled.

Sample cooling

The trapping rate of positrons depends on the temperature of the sample, as explained in section 2.2.2. Within the scope of this work magnesium and the magnesium based alloy AZ31 were to be investigated (see chapter 5) since these materials are cited in the literature as having a low trapping rate and shallow trapping sites [83, 84, 5], a sample cooling became necessary.

Horizontal mounting of the HPGe-detectors

In the first version of the CDB-spectrometer, the HPGe-detectors have been mounted horizontally as sketched in figure 4.1 in order to simplify the setup. This geometry had two main disadvantages. Firstly, the detectors were in one plane which made the extension by further detector pairs difficult due to lack of space. Secondly, a fraction of the detected annihilation radiation had to penetrate a rather large part of the sample and was hence partially screened. Since the sample was moving to achieve spatial resolution, the attenuation and therefore the count rate in the detectors varied depending on the sample position. As mentioned in section 3.2, the energy resolution of HPGe-detectors and the signal chain—analog or digital—depends strongly on the count rate at higher rates which caused a sample position dependent energy resolution and therefore influenced the S-parameter.

This effect is exemplarily shown in figure 4.6. An annealed magnesium sample has been two dimensionally scanned with the positron beam at an energy of 17 keV and a step size of 1 mm. This sample has been treated with an ion beam such that in the center a defect rich region can be detected, as indicated by the increased S-parameter. For detector A the count rate amounted to roughly 8900 cps for the measurement on the right hand side and to about 8500 cps on the left hand side, which is a relative difference of 4.5 %. The measurements of both detectors are shown where apparently an asymmetry depending on the position of the positron beam occurs. Detector A on the left hand side of the sample reveals lower S-values in the S-parameter map on the left side due to less screening which lead to higher count rates and consequently worse energy resolution. In case of detector B, the decreased S-parameter region is on the right hand side according to its position. This measurement has been performed with the analog signal chain and therefore higher count rates were not possible. Although less distinct, the same effect was also observed with the digital signal chain at higher count rates.

4.3.1 Design of the CDBS2

To overcome the above mentioned disadvantages of the first version of the CDBS, the sample chamber including the beam guiding and the detector mounting has been changed. In the following sections, all major changes are presented with the respective simulations and first measurements of the performance of this apparatus are described.

Magnetic field termination

At the entrance of the CDBS2 a magnetic field termination ensures, that no magnetic guiding field penetrates into the sample chamber and aggravates the electrical focusing of the positron beam. The principle of such magnetic terminations for beam guiding has been used in several other systems at NEPOMUC systems like the CDBS1, the positron induced Auger system PAES [50] and the remoderation facility [61]. The fundamental principle is based on non-adiabatic magnetic beam guiding. The positrons are following the magnetic flux lines as long as their gyration length is small compared to the gradient of the magnetic field [85].
Let v_T and v_L be the transversal and the longitudinal component of the positron velocity. The gyration radius r is then given by

$$m\frac{v_\mathrm{T}^2}{r} = qv_\mathrm{T}B \Rightarrow r = \frac{mv_\mathrm{T}}{qB} \ , \tag{4.3}$$

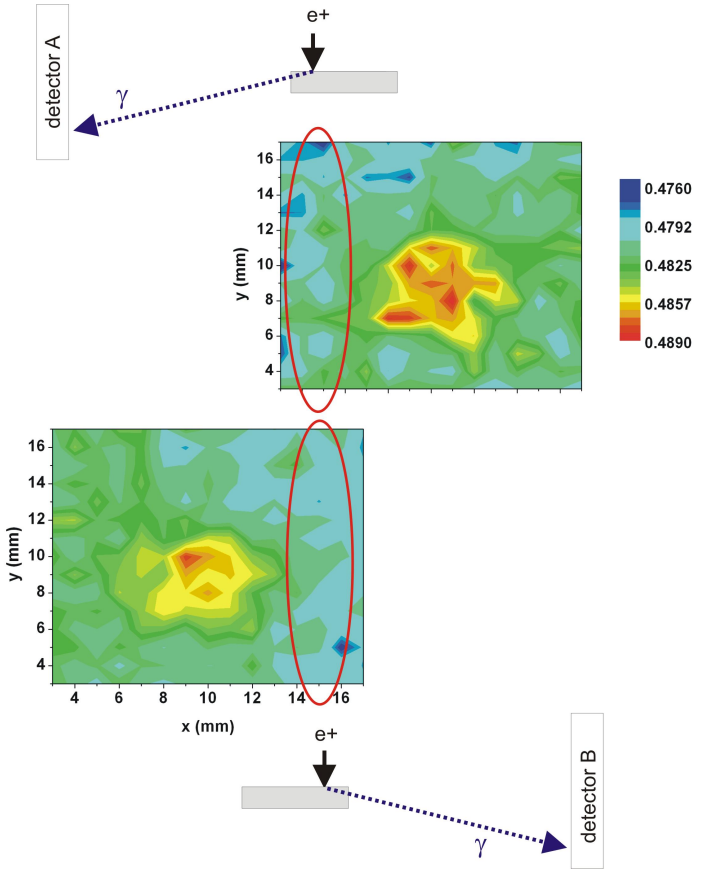

Figure 4.6: Two dimensional S-parameter scan on an annealed magnesium sample with a defect rich region in its center, as indicated by an increased S-parameter. Depending on the position of the positron beam, the sample screens the emitted annihilation radiation as indicated in the sketches and therefore the count rate in the detectors varies by about 4.5 %. Since the energy resolution is count rate dependent, the S-parameter increases, if the positron beam hits the sample on the side closer to the detector, leading to an asymmetry in two dimensional scans as indicated with the red ellipses.

where q represents the charge of the positron and B the magnetic field. Consequently the time for one revolution is given as

$$T = 2\pi \frac{m}{qB} \ . \tag{4.4}$$

The gyration length h depends on the longitudinal velocity component of the positron via

$$h = v_{\mathrm{L}} \cdot T = 2\pi \frac{m v_{\mathrm{L}}}{qB} \ . \tag{4.5}$$

If positrons are to be released from a magnetic field without changing the transversal momentum significantly, two possible solutions can be applied. Firstly, the magnetic field can be changed abruptly, such that the gyration length is much larger than the region where the field changes. This technique has been used in the CDBS1, which was designed for a fast beam with 1 keV energy. In order to change the field rapidly, a μ-metal aperture with a 3 mm hole has been used as described in [17].

Secondly, if the positrons are initially slow and no losses due to a small μ-aperture are acceptable, it is possible to guide them through a hole with bigger diameter, where the B-field changes slower, and to compensate this by accelerating them through the termination according to equation 4.5. The latter principle has been used for the CDBS2, since the remoderated beam is only adjustable in a limited energy range from 20 to 200 eV and intensity losses are not accepted at this point. The design of the magnetic termination is shown in figure 4.7. It consists of a μ-metal aperture which is shaped like an inverse cone with 10 mm diameter on the top and 30 mm on the bottom with a thickness of 14 mm. The cone shape is generally used to overcome saturation effects due to the increasing magnetic flux for larger radial distances. It is lying on a ceramic ring for insulation purposes and is separated from the outer part of the μ-shielding with a gap of 1 mm. A smaller gap is not practical, since it should insulate voltages of the order of a few kV. This setup has been tested in vacuum in order to find the maximum applicable voltage. It must therefore not exceed −3 kV, otherwise electrical sparks between the grounded outer μ-shielding and the inner part may occur. The outer part of the μ-shielding guides the magnetic flux lines back in order to obtain a small as possible field directly below the termination. Since it is mounted on a grounded flange with a thickness of 25 mm, a non-magnetic steel tube just below the termination with the same potential screens the positron beam. In figure 4.7 the parts with −3 kV accelerating voltage appear dotted, i.e. the inner μ-aperture and the potential screen.

The multipurpose FEM-program COMSOL has been used to simulate the magnetic flux density distribution of this structure, if a guiding field of roughly 6 mT is applied as seen in figure 4.8 [86]. Due to the cylindrical symmetry of the geometry, only the half space with positive distance r from the center has been taken into account in order to save computing time. The structure of the field termination is sketched in this figure with black lines and the positrons fly collinear with the z-axis.

According to this simulation, the flux density drops from 5 to 0.6 mT within a distance of 20 mm. At the inner part of the release 3 kV at maximum can be applied which results in a gyration length of max. 23.5 cm, which is an order of magnitude larger than the length scale of the breakdown of the magnetic flux density.

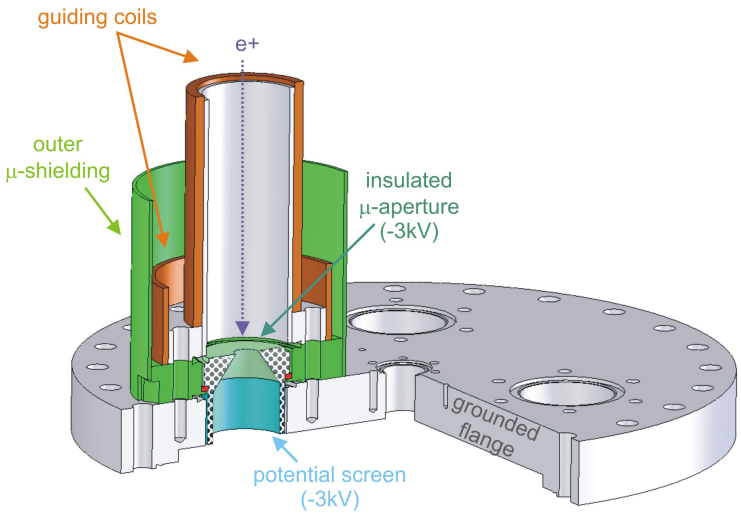

Figure 4.7: Magnetic field termination of the CDBS2. The positrons come from above and are accelerated with −3 kV onto an electrically insulated inverse cone consisting of μ-metal, which is used to abruptly decrease the magnetic guiding field to nearly zero. The increased gyration length of the positrons due to the acceleration and the fast change of the field result in a non-adiabatically release of the positrons from the magnetic guiding field. The inner diameter of the cone increases from 10 to 30 mm in order to pick up the increasing magnetic flux with distance to the center. A steel potential screen ensures, that the positron beam is flying in an electrical field free space since the surrounding grounded flange would distort the positrons trajectories. The parts lying on −3 kV appear dotted in this figure.

The color-coding ends at 10 mT in order to show the small variations within the μ-aperture. A colorless area in the outer μ-shielding is the consequence, where a maximum flux density of 350 mT is reached, which is far away from the saturation flux density of 0.8 T in μ-metal.
The insulated inner part of the termination allows to accelerate the positrons through this magnetic transition in order to fulfill the above mentioned condition for a non-adiabatic release of the positrons. This device consequently allows to non-adiabatically release the beam from the guiding field (detailed simulations of the positron trajectories are presented in section 4.3.1).

Aperture with variable size

The positron beam can be easily focused, if its diameter at the entrance of the focusing system is small and low positron intensities are acceptable. On the other

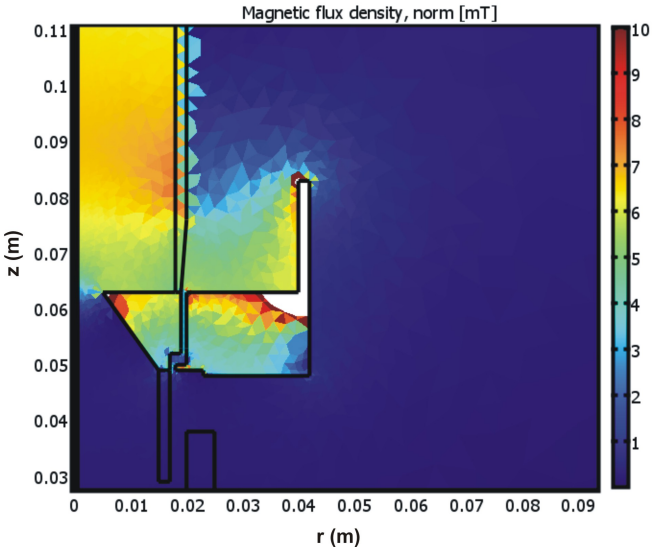

Figure 4.8: COMSOL-simulation of the magnetic field termination in the CDBS2. The positrons are guided from above along the z-axis with a guiding field of 5 to 6 mT flux density. It drops from this value to 0.6 mT within 20 mm at the µ-aperture, which allows a non-adiabatic release of the positron beam from the magnetic guiding field for sufficiently high positron energies. The color-coding ends at 10 mT in order to show the small variations within the µ-aperture.

hand, if the focal diameter for the current measurement is not important, a higher intensity is favorable and an entrance aperture with a bigger diameter is needed. Therefore an aperture with variable size has been designed consisting of a rotatable disc, 185 mm in diameter, with the different boreholes 0.1, 0.5, 1, 2, 3, 4, 6, 8, 10, 12, 16 and 30 mm (see figure 4.9). The larger boreholes could be used for a non-remoderated positron beam with larger diameters if the use of the primary beam of NEPOMUC is desired (see section 2.4.3). The variable aperture is mounted about 5 mm below the magnetic field termination inside the vacuum and manipulated via a rotary feedthrough from atmosphere. By turning the disc, a desired part of the positron beam can be shielded and the beam diameter at the entrance of the focusing system is adjustable.
Since the magnetic field termination is insulated and set on potential, the aperture disc and the first lens of the subsequent lens system are also on the same voltage in order to ensure that the geometry of the aperture does not distort the passing trajectories of the positrons. Otherwise, a set of lens voltages for every possible aperture diameter would have been necessary since the respective electrical field would have been changed.

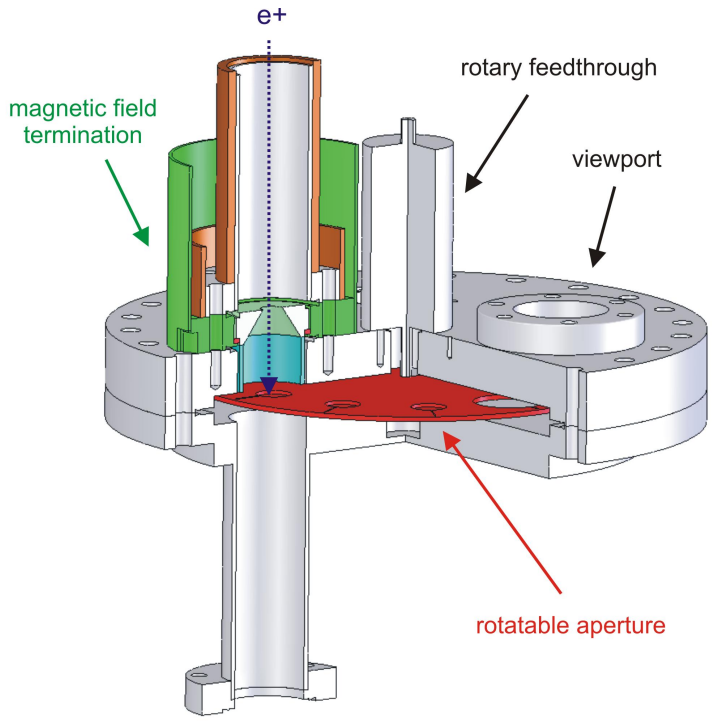

Figure 4.9: Drawing of the variable aperture of the CDBS2. The diameter of the positron beam can be adjusted after the release from the magnetic guiding field with a rotatable disc of 185 mm diameter with 12 boreholes in the range of 0.1 to 30 mm. It is manipulated via a rotary feedthrough from atmosphere and set to the voltage of the magnetic field termination and the subsequent entry lens of the focusing system in order to leave the geometry of the positron trajectories independently from the aperture diameter. The subsequent lens system is not shown here.

Beam guiding with electrical lenses and trajectory simulations

The variable aperture causes a strong background radiation if a borehole with a small diameter is used to reduce the beam size at the entrance of the lens system. It is therefore favorable to increase the distance of the aperture from the sample, in order to keep the aperture induced background in the detectors as small as possible. To fulfill this condition, the lens system has been designed such that the beam is guided electrically over a distance of $\sim 140\,\mathrm{mm}$ before it enters the main part of the sample chamber. It consists of four insulated Al-tubes as Einzel lenses as shown in figure 4.11 where the first three lenses are used to guide the beam into the chamber and the fourth lens focuses the beam onto the sample. Since the sample is set on negative potentials down to $-30\,\mathrm{kV}$ and the surrounding chamber is grounded, an additional focusing is achieved due to the resulting electrical field. The fundamental principle of the lens system is schematically described in figure

4.10. As mentioned above, the magnetic field termination, the variable aperture and the first lens have to be set to the same potential, namely −3 kV in order to achieve an aperture independent geometry of the electrical field. By alternating the potentials between the following lenses, the positron beam can be focused. Every transition from lens to lens encloses focusing and defocusing regions due to the resulting force as shown in the figure. It is crucial, that the positrons have high kinetic energies in the defocusing regions, since the respective influence on the beam is then limited and hence the focusing effect dominates. Between the fourth lens and the sample only focusing occurs, since the sample is set on negative potential.

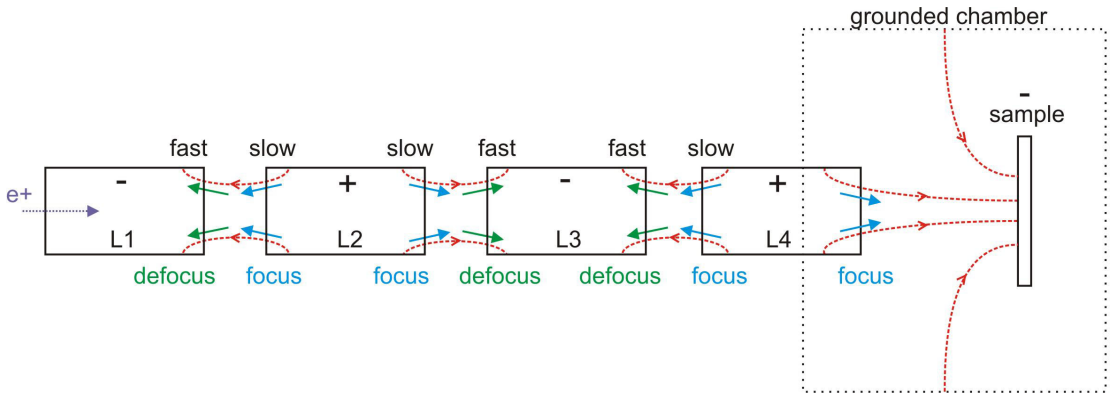

Figure 4.10: Principle idea of the electrical lens system (90 ° rotated); the positrons enter from the left side. Lens 1 (L1) has to be set on −3 kV as explained in the text. By alternating the potentials of the following lenses, the positron beam can be focused. Every transition encloses focusing and defocusing regions, but due to the potential differences, the positrons have lower kinetic energies in the focusing regions, which causes them to dominate the defocusing ones. Between L4 and the sample, the beam is further focused, due to the negative potential at the sample.

The sample can be moved perpendicular to the beam direction, which distorts the electrical field in the chamber. A potential ring below the sample had to be installed in order to homogenize the potential landscape and to make it independent from the position of the sample. It reaches nearly to the inner surface of the chamber and has an inner diameter of 80 mm to leave space for the sample mounting (see section 4.3.1) and the cryostat. The sample holder with 55 mm diameter is 75 mm away from the last lens. In figure 4.11 all other relevant measures for simulations of the electrical field are shown together with a sketch of the sample chamber which has a diameter of 200 mm and is rotationally symmetrical except the fittings for pumping and sample transfer. These fittings are located in one plane to leave as much as possible of the respective half space accessible for the detectors which would be perpendicular to the drawing plane in figure 4.11.

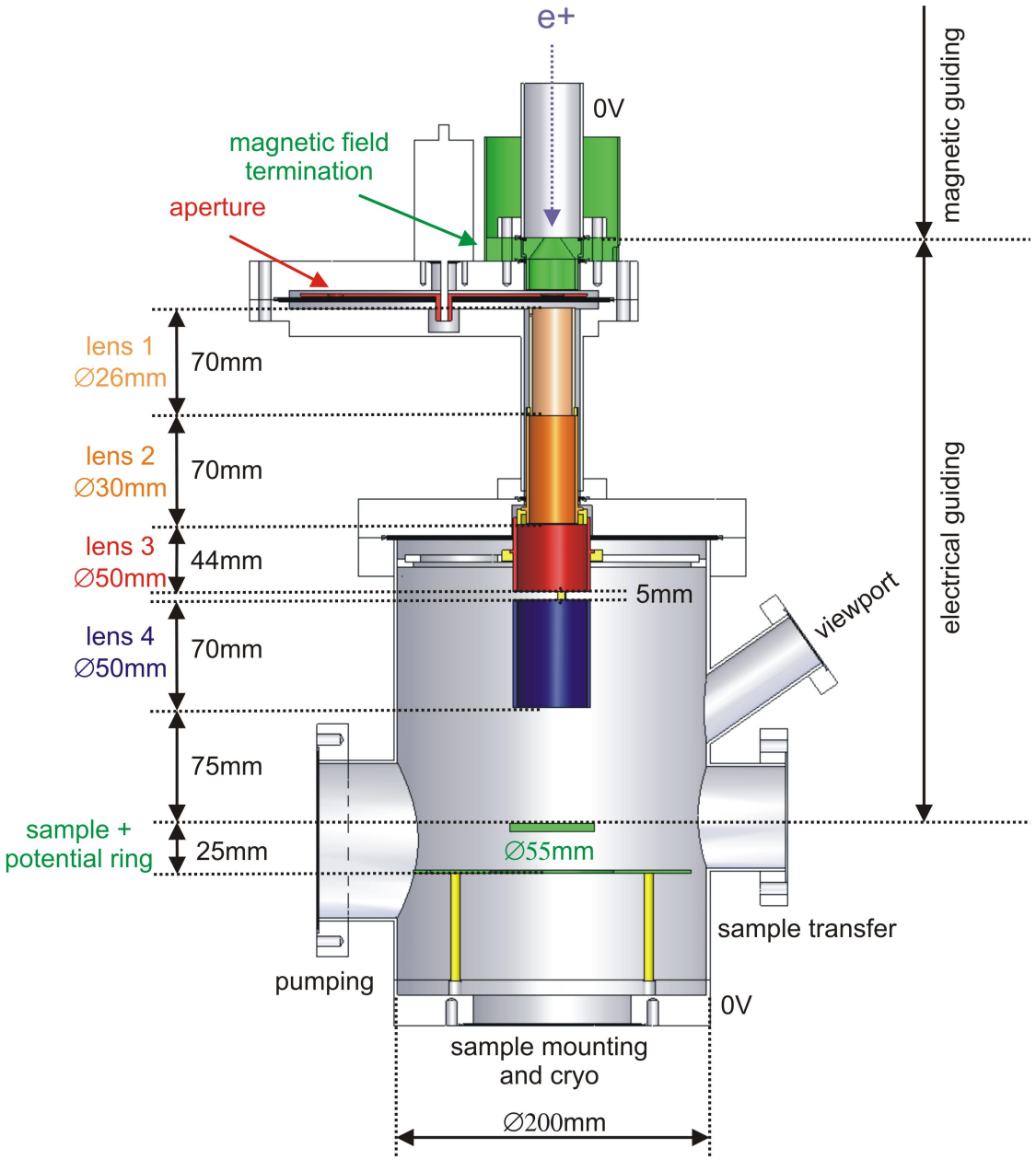

Figure 4.11: Sketch of the sample chamber of the CDBS2. The magnetic field termination, the variable aperture, the lens system, the sample holder and the potential ring are shown together with all relevant measures. The fittings for pumping, the viewport and sample transfer are located in one single plane in order to leave free space for the detectors which are located in a plane perpendicular to the drawing plane.

In order to find the best potentials for the lenses 2 to 4, COMSOL has been used to simulate the positron trajectories. Only a limited number of positrons can be traced through the simulation due to calculation time which complicates an absolute intensity estimation or a quantitative prediction of the FWHM of the beam, but the absolute beam diameter has been determined. In these simulations the magnetic guiding field and the magnetic field termination as well as the electrical field have been taken into account. As a result of these simulations, lenses 2 and 3 can be set to the constant voltages -1 and $-1.8\,\mathrm{kV}$ respectively and only lens 4 has to be adjusted dependent on the sample potential. The result for $-10\,\mathrm{kV}$ sample potential is shown in figure 4.12, where a 5 mm positron beam with 20 eV kinetic energy in beam direction and 0.1 eV transversal energy enters the magnetic field termination from the left (the beam axis is rotated by 90 ° with respect to figure 4.11)[2]. The variable aperture in this simulation has been set to 10 mm, such that the full incoming beam is taken into account. It gyrates through the magnetic guiding field, increases its gyration length due to the acceleration toward the field termination, gets non-adiabatically released from the magnetic field, flies electrostatically guided through the lens system and is finally focused onto the sample, where a focal diameter of 1 mm is achieved, if lens 4 is set to $-645\,\mathrm{V}$. This figure shows also the electrical and magnetic fields in their respective units. Note the electrical potential: In the sample region, the potential ring beneath the sample holder homogenizes the potential landscape according to the beam axis as expected in order to prevent the positron beam from following the moving sample.

These simulations have been used to determine the optimum voltages of the fourth lens depending on the sample potential. The results are presented in table 4.2 with a rough estimation of the achievable total focal diameter. For sample potentials between -20 and $-4000\,\mathrm{V}$ the beam can only be focused down to 3 to 4 mm due to the missing focusing effect of the negative sample itself. By reducing the size of the variable aperture, the focal diameter can be decreased according to the simulations at the expense of count rate.

These values have been used for the CDBS2 control software which in the newer version interpolates linearly between them, in contrary to the CDBS1, where a fit function was used.

[2] These beam parameters are conservative assumptions, since the remoderated beam from NEPOMUC is by a factor of 2.5 smaller [61]. Its transversal energy has not been measured so far, but 0.1 eV is four times larger than the thermal energy spread of the remoderator.

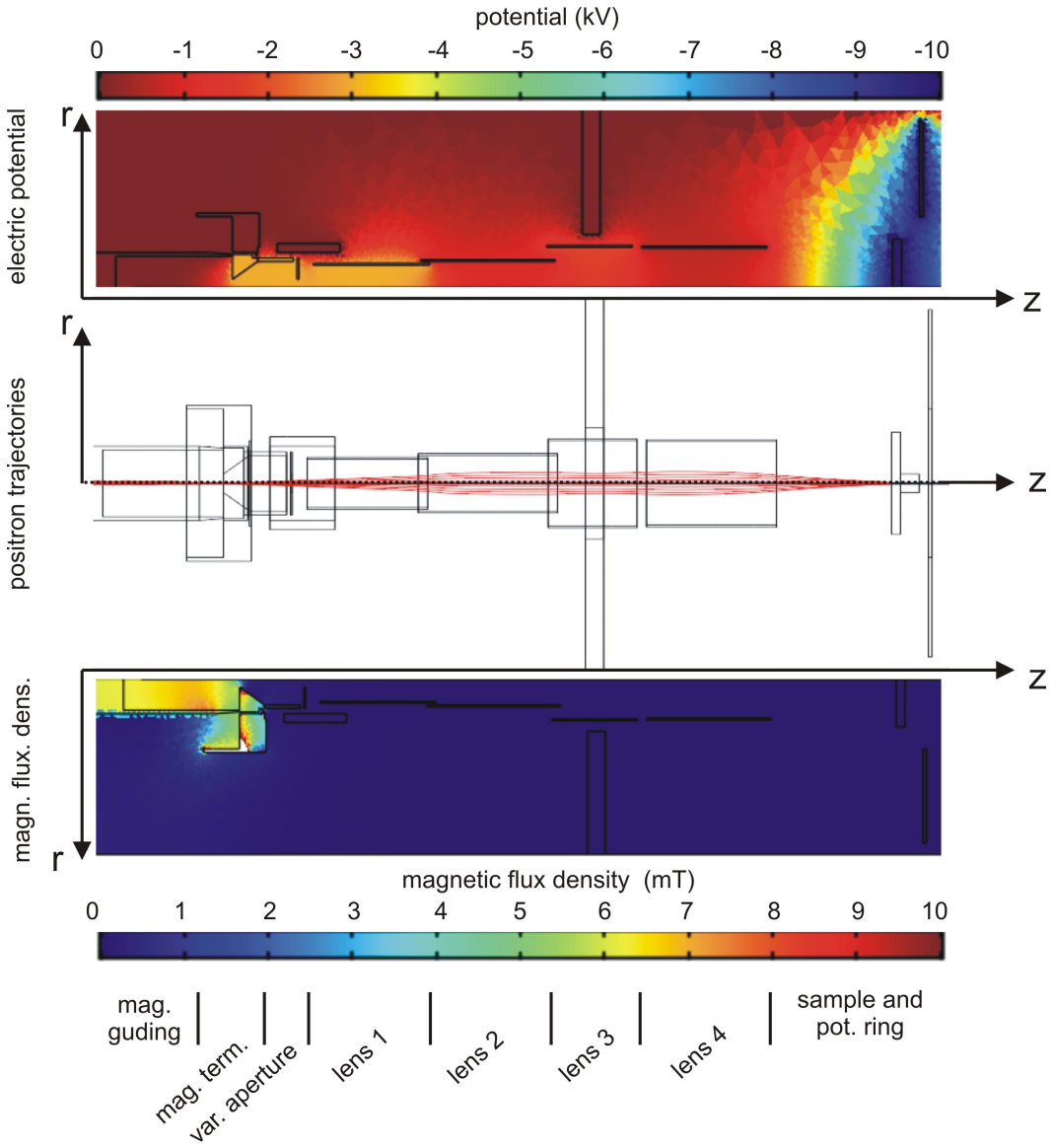

Figure 4.12: Simulation of the electrical and magnetic field with the respective positron trajectories for −10 kV sample potential. A 5 mm positron beam enters the system from the left side with 20 eV and 0.1 eV longitudinal and transversal energy in a guiding field of 5 to 6 mT flux density. It is accelerated toward the magnetic field termination which is together with the variable aperture and the first lens set to −3 kV. The diameter of the variable aperture amounts to 10 mm in this simulation. After the release from the magnetic field, the beam is guided with lenses 2 and 3 which are set to -1 and −1.8 kV respectively. The fourth lens has to be adjusted depending on the sample potential. For −10 kV sample potential, its voltage has to be −645 V in order to achieve a focus of ∼ 1 mm.

sample potential (V)	potential of lens 4 (V)	∼focal diameter (mm)
-20	-400	3 to 4 mm
-200	-405	3 to 4 mm
-2000	-420	2 mm
-4000	-430	2 mm
-6000	-440	1 mm
-8000	-450	1 mm
-10000	-645	1 mm
-12000	-715	1 mm
-14000	-750	1 mm
-16000	-800	1 mm
-18000	-825	1 mm
-20000	-900	1 mm
-26000	-1160	1 mm
-30000	-1500	1 mm

Table 4.2: Voltages of lens 4 for various sample potentials according to a small focus in the COMSOL-simulations. For sample potentials between -20 and −4000 V the focus becomes larger due to the lack of focusing by the negative sample itself.

Sample mounting, cooling and detector geometry

The sample holder of the CDBS2 has to meet four main requirements. Firstly, it should be movable in the vacuum system in order to perform two dimensional scans. Secondly, it has to be insulated to apply an acceleration voltage down to −30 kV for adjusting the positron energy and hence the positron implantation depth. Thirdly, a sample cooling is necessary in order to investigate materials with shallow traps and fourthly only very small amounts of structure material should attenuate the annihilation radiation on its way to the detectors.
A schematic view of the new sample holder with insulator is shown in figure 4.13. It is about 77 mm high and has a diameter of 55 mm. It is capable to hold samples with a footprint of $20 \times 20\,\mathrm{mm}^2$. The sample is distinctively smaller than the diameter of the sample holder in order to achieve an homogeneous as possible electrical field to suppress the effect of moving in an electrical field as described in 4.3.1. As seen from the positron beam, the sample chamber and the sample holder are fully rotationally symmetric in order to achieve a symmetric focusing, except the shape of the sample itself.
The positioning of the sample in the CDBS2 is accomplished with the same step motor unit as in the CDBS1. Nothing had to be changed except an adapter plate

which is used to mount the cryostat.
The electrical insulation is demanding in terms of heat conductivity. Using a simple ceramic insulator as it has been done in the CDBS1 is not possible, since the thermal contact between sample holder and cryostat would then be weak. Therefore, a sapphire insulator has been constructed which ensures a good thermal contact at low temperatures on the one hand and insulates electrically on the other hand. The thermal conductivity of sapphire at 4 K amounts to $\sim 250\,\frac{\mathrm{W}}{\mathrm{mK}}$ and is therefore in the same range as copper at room temperature [87]. It consists of a rod with 8.4 mm diameter furnished with four ribs with 14.4 mm diameter in order to increase the free path on the surface to suppress surface currents. The length of this sapphire crystal is 23.5 mm and therefore its absolute thermal conductivity at 4 K amounts to $\kappa = \frac{250\,\mathrm{W}}{\mathrm{mK}} \cdot \frac{5.5 \cdot 10^{-5}\,\mathrm{m}^2}{23.5 \cdot 10^{-3}\,\mathrm{m}} = 0.59\,\frac{\mathrm{W}}{\mathrm{K}}$. The electrical insulation has been tested in advance by applying $-30\,\mathrm{kV}$ to this insulator in a vacuum chamber at $2 \cdot 10^{-6}\,\mathrm{mbar}$ where no sparks or leak currents occurred.
The cooling of the sample down to liquid nitrogen temperature is performed with a standard cold head RDK-205D from Sumitomo with the respective compressor unit [88]. Its cooling power amounts to 0.4 W at 4 K. The sample holder is manufactured from copper to ensure a good thermal coupling to the cryostat. It consists of three main parts which are screwed together: a base plate fixing the sample holder on the sapphire crystal and the cryostat, a copper rod and the upper plate holding the sample in a small recess. Between the several parts of the sample holder as well as in all gaps between cryostat and sapphire Galinstan has been used to increase the thermal contact[3].
The temperatures at the sample position T_1, between sample holder and insulator T_2 and the cold head T_3 have been measured in vacuum with $2 \cdot 10^{-6}\,\mathrm{mbar}$ (see also figure 4.13) and the respective temperature curves have been determined (figure 4.14). Whereas the cold head reaches at minimum 6 K, the smallest T_2 amounts to 48 K and the according sample temperature T_1 is reduced to 76 K. The temperature differences result from infrared radiation of the surrounding vacuum chamber at room temperature and the high thermal resistance of the junctions between the parts of the sample holder. The fact that the cryostat does not reach the specified 4 K but only 6 K may be a consequence of two facts: heat input to the sample holder by thermal radiation and the high temperature in the experimental hall of the reactor since at the position of the compressor 28 ° are easily reached (the cooling capacity of the cryostat drops by 5% in this temperature range).
In order to leave as little material as possible in the direct view of the detectors, a recess below the sample has been introduced, such that 25 ° tilted detectors obtain a direct sight onto the positron focus. The tilting of the detectors has several advantages. The small angle scattering is reduced and therefore the count rate

[3] Galinstan is a fluid consisting of gallium, tin and indium which solidifies at −19 °C. It is widely used to increase the thermal contact in high vacuum applications [89].

does not depend on the position of the sample. Furthermore, four detectors can be mounted in the same plane in order to save space. This setup allows to place up to 16 detectors around the sample chamber. A schematic view of the CDBS2 and a picture are given in figures 4.15 and 4.16.

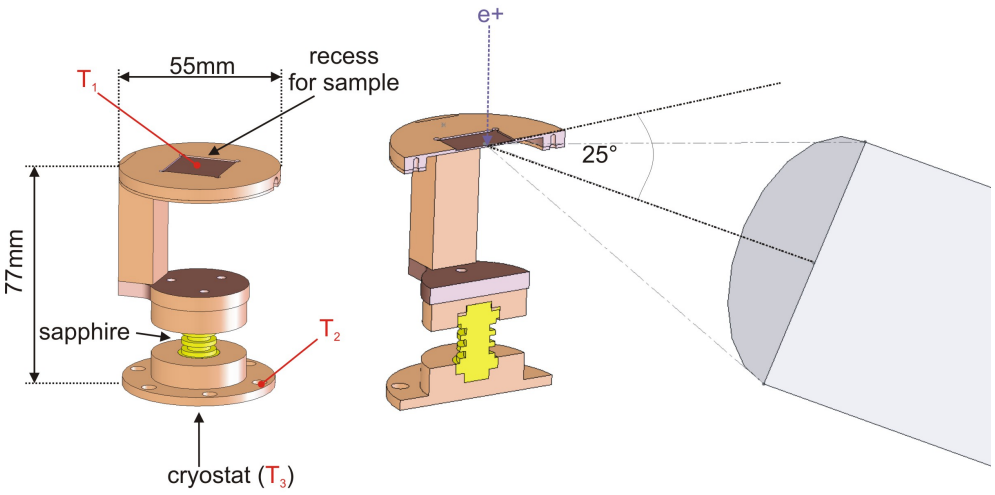

Figure 4.13: Sample holder of the CDBS2 manufactured from copper. It is attached to a cryostat to reach liquid nitrogen temperature at the sample position. A sapphire crystal ensures the electric insulation for voltages down to −30 kV and a good thermal contact. The copper rod outside the direct view of the detectors holds a copper plate on which the sample lies in a small recess. This plate has been milled out from below in order to enable a direct view onto the focus of the positron beam. The solid angle of detectors tilted 25 ° against the plane perpendicular to the positron beam is therefore free from any structure material except the thin copper layer beneath the sample. The red points denoted by T_1 and T_2 show, where the temperature has been measured during the first cooling down in vacuum.

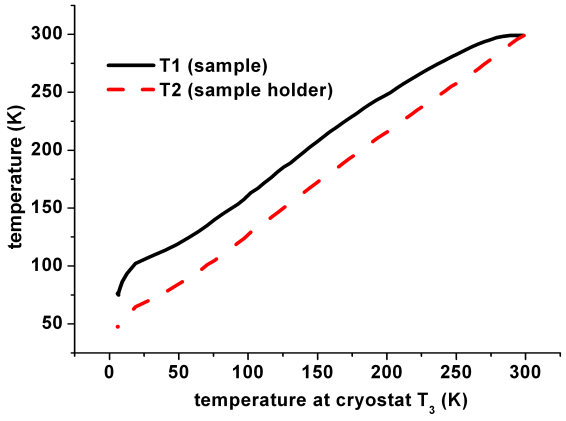

Figure 4.14: Temperature measured at the bottom of the sample holder (T_2) and at the sample position (T_1) as a function of the temperature of the cryostat (T_3). The positions of the temperature measurements are shown in figure 4.13. The lowest achievable sample temperature is 76 K.

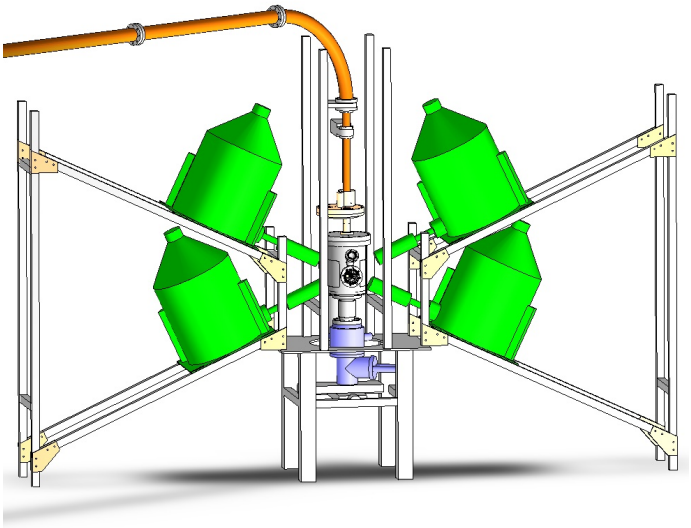

Figure 4.15: Schematic view of the CDBS2. The positron beam is guided magnetically through the tube above the spectrometer. After being released from the magnetic field, the beam enters the chamber of the variable aperture and is then guided further with electrical lenses into the sample chamber which is mounted on a table with the step motor units to position the sample and cryostat in vacuum. Four HPGe-detectors are inclined by 25 ° and directed to the annihilation point of the positron beam on the sample. The side walls of the sample chamber have been thinned to ~ 1 mm in the view of the detectors to reduce absorption and small angle scattering.

Figure 4.16: Photograph of the CDBS2 in the experimental hall of the reactor. The rack on the left side comprises all necessary electronic components.

4.3.2 First measurements of the beam parameters of the CDBS2

The performance of the CDBS2 has been measured firstly in September 2007 with a T-shaped Al-W-sample as shown in figure 4.17 with an aperture size of 12 mm, i.e. full positron beam. Up to this point, only the two Canberra HPGe-detectors with their digital signal chain have been used for the measurements since MSPEC2D is currently limited to the analysis of only two detectors. The total count rate per detector in these measurements amounted to $\sim$ 31000 cps and a photopeak count rate of $\sim$ 7000 cps has been achieved which is about 1.3 times higher than in the CDBS1 although the detectors are due to the larger sample chamber twice as far away, namely $\sim$ 120 mm at minimum. Despite the larger distance between sample and detector compared to the CDBS1, the single photo peak count reaches this higher value since the magnetic field termination has been designed with a larger diameter and therefore no annihilations occur at this point as explained in 4.3.1. However a very important advantage of the new setup becomes apparent. Whereas the CDBS1 only achieved a coincident photopeak count rate of 500 cps at maximum, the CDBS2 reaches 1400 cps, namely 2.8 times larger. The explanation for this is obviously that no annihilation background in case of an open variable aperture pollutes the spectra of the HPGe-detectors. Whereas in the CDBS1 a large amount of detected events in the single spectrum originated from the annihilations in the magnetic field termination which contributed only to the single photopeak count rate but not to the coincident photopeak count rate, all events being detected by the CDBS2 result exclusively from the sample.
The S-parameter depending on the position of the positron beam has been measured for the sample potentials -1, -4, -10, -20, -24 and -30 kV with a step size of 1 mm. The result for 1 kV is plotted in in figure 4.17 where the scanned area is marked with a red rectangular on the picture of the sample. Initially a larger area was supposed to be scanned but due to the failure of a power supply, it barely reached the border between Al and W. This measurement could not be repeated due to lack of beam time. Nevertheless, the spatial extension of the beam can be estimated since the maximum deviation between Al and W is well known. The zero position of the step motor unit was not correctly adjusted during this measurement such that the x-values are shifted by 5 mm but this does not disturb the interpretation in any manner. The measurement was performed with a step size of 1 mm, scanning an area with 6×10 mm and a measurement time of 7 s per point resulting in a measurement time of only 7 min per two dimensional scan!
In order to verify the potentials of lens 4 resulting from the COMSOL-simulations, the initially determined value has been changed with $\Delta U \in \{-75, -25, -10, 10, 25, 75\}$ with a full scan for each value and for all sample potentials. A profile at $x = 12$ mm for 420 V at lens 4 has been derived and

fitted with a Gauss function. The resulting FWHM amounts to 1.85 ± 0.29 mm in accordance with the COMSOL-simulations where the total beam diameter has been determined. In this voltage range the influence of lens 4 is rather limited. The measured position of the border at this sample potential is 9.5 mm. For the lower sample potentials -4, -10, -20, -24 and -30 kV the same measurement has been performed and evaluated. The plots are shown in figure 4.18 denoted with the respective sample potential. The diameter of the beam is again in very good agreement with the COMSOL-simulations and the Gauss fit of its derivative reveals a FWHM of 1.79 ± 0.35 mm for -4 kV and 0.88 ± 0.12 mm, 0.59 ± 0.20 mm, 0.64 ± 0.11 mm and 0.58 ± 0.16 mm for -10, -20, -24 and -30 kV sample potential. Nevertheless, the measured position of the beam is shifted to 10.5 mm for -30 kV.

In order to clarify the sample potential dependent shift of the beam position, COMSOL has been used to simulate the positron trajectories with the same settings as in 4.3.1 but extended with a constant earth magnetic field of 0.2 G tilted 60 ° against the horizontal plane. Figure 4.19 shows the positron trajectories with the same parameters as in section 4.3.1 for -4 and -30 kV sample potential, with and without the constant magnetic field. Obviously, a beam shift in the range of $\sim$ 2mm can be attributed to the presence of this magnetic field. The same beam shift also occurred in the CDBS1 but much less distinct as seen from figure 4.4, since its distance between magnetic field termination and sample was about a third of that in the CDBS2. To overcome this effect, active compensation coils could be used which however would have to be far away from the beam in order to create a sufficiently homogeneous compensation field. Another possibility is to install a µ-metal housing as it has been implemented for example at the positron microscope SPM at the Bundeswehr university in Munich [90], although such a housing would be very expensive. However, this solution is favorable since it also passively screens influences of the big crane in the experimental hall of the reactor which also perturbs the magnetic guiding field and causes a drop in the count rate when passing by.

In order to investigate the influence of the variable aperture, the sample shown in figure 4.17 has been scanned in y-direction for constant $x = 12$ mm at 25 kV sample potential with the aperture set to 0.5, 1 and 10 mm. The result is shown in figure 4.20. The small aperture diameters led to a distinctively reduced count rate and therefore higher S-values due to the better resolution of the γ-spectroscopy system. Consequently the S-curves of all three measurements have been normalized in such a way that their highest S-values amount to 1. Using the 1 or 0.5 mm-aperture reduces the count rate by a factor of 25 or 100 respectively, compared to the 10 mm-aperture where no losses occur.

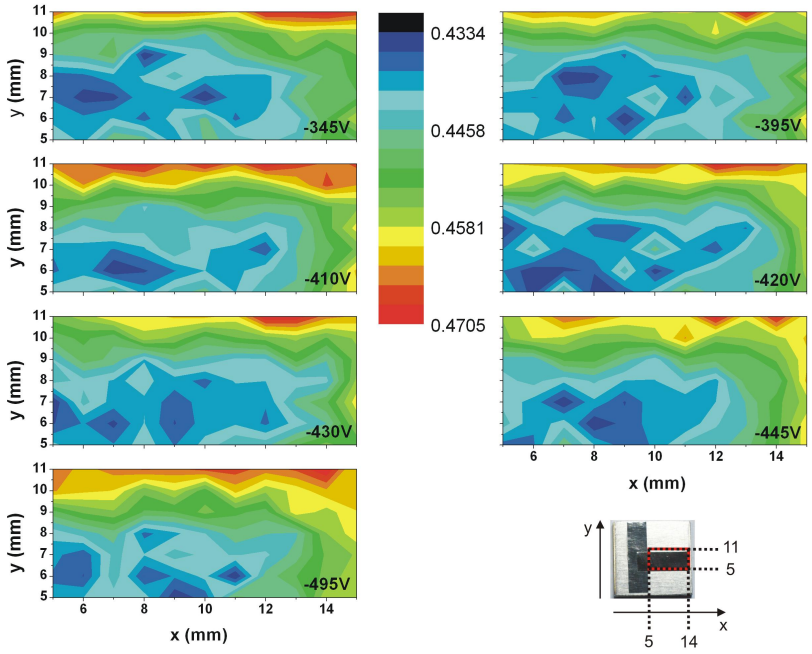

Figure 4.17: S-parameter scan of the Al-W-sample shown in the right lower corner over the marked area at 1 kV sample potential. In order to verify the potentials of lens 4 resulting from the COMSOL-simulations, the lens has been adjusted to the denoted values and a full scan has been performed each. The FWHM of a Gauss fit of the profile at $x = 12\,\text{mm}$ results in 1.85 mm for $-420\,\text{V}$ at lens 4 which is in good aggreement with the COMSOL-simulations where the total beam diameter has been determined to be $\sim 3\,\text{mm}$. The increase of the S-parameter on the right end of the sample is related to the edge of the beginning copper sample holder.

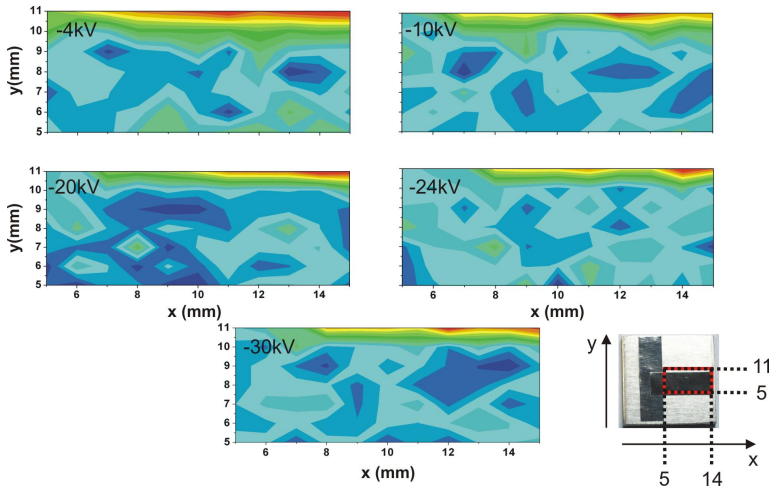

Figure 4.18: S-parameter scans for resolution measurements similar to figure 4.17 for various sample potentials—the potentials of lens 4 are taken from table 4.2. The FWHMs of the Gauss fits of the derivatives of S(y) at $x = 12\,\mathrm{mm}$ result in 1.79, 0.88, 0.59, 0.64 and 0.58 mm for -4, -10, -20, -24 and $-30\,\mathrm{kV}$. Furthermore, the position of the positron beam is shifted to larger y-values for decreasing sample potential which can be explained with the presence of a constant earth magnetic field as shown in figure 4.19.

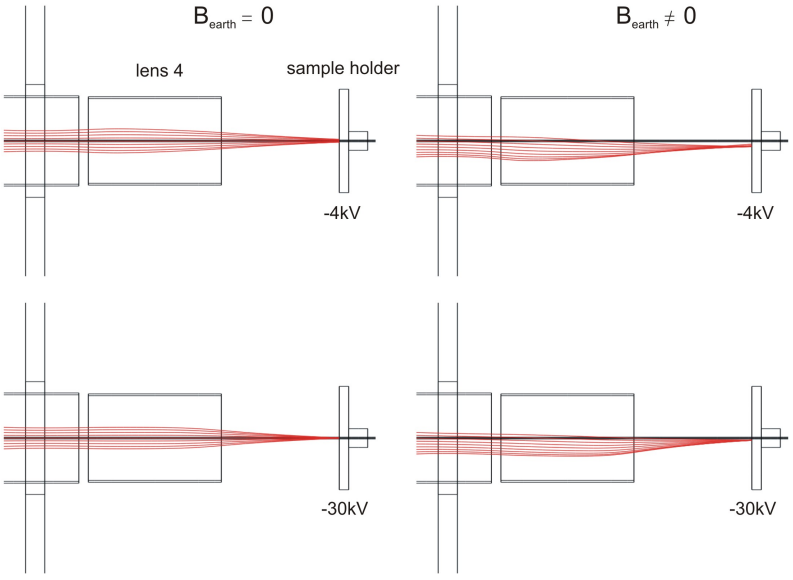

Figure 4.19: COMSOL-simulations of the influence of a constant magnetic field B_{earth} of 0.2 G tilted 60 ° against the horizontal plane as a model for the earth magnetic field on the positron trajectories at different sample potentials. For $B_{\mathrm{earth}} = 0$, the positron beam is focused as denoted in table 4.2 to the center of the sample holder, whereas for $B_{\mathrm{earth}} \neq 0$ a sample potential dependent shift occurs in the range of $\sim 2\,\mathrm{mm}$.

The derivative of the S(y)-curve and the FWHM of its Gauss fit for the 10 mm aperture size have been already determined for 24 kV. For 1 and 0.5 mm (sample potential 25 kV) the FWHMs are 0.25±0.08 and 0.32±0.08 mm thus showing that a further reduction of the aperture size does not decrease the achieved focal diameter which may be related to the transversal momentum of the incoming positron beam. Table 4.3 compares the beam dimensions of the CDBS1 (d_{CDBS1}) in y-direction with the values achieved with the CDBS2 (d_{CDBS2}). It shows, that the resolution of the CDBS2 has been significantly improved compared to the CDBS1.

Table 4.3: Lateral resolution of the positron beam in the CDBS1 and 2: FWHM in mm of the derivatives of the S(y)-curves.

CDBS1 26 kV	CDBS2 24 kV Aperture 10 mm	CDBS2 25 kV 1 mm	CDBS2 25 kV 0.5 mm
1.61 ± 0.16	0.64 ± 0.11	0.25 ± 0.08	0.32 ± 0.08
$d_{\mathrm{CDBS1}}/d_{\mathrm{CDBS2}}$	2.5	6.4	5

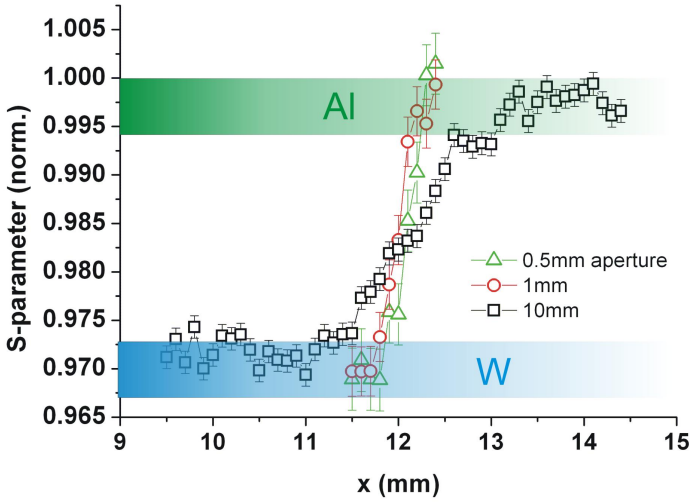

Figure 4.20: S-parameter scan over an Al-W-edge at 24 and 25 kV sample potential with the variable aperture set to 0.5, 1 and 10 mm, respectively. The derivative of this curve and a respective Gauss fit reveal FWHMs of 0.3 mm for the two small apertures and 0.7 mm. for the 10 mm aperture. For details see table 4.3 and text.

The sample from figure 4.6 has been scanned with the CDBS2 at 17 kV sample potential and a step size of 1 mm in order to investigate whether an asymmetry between two opposed detectors occurs. The respective S-parameter measurement is

shown in figure 4.21. The total count rate per detector does not vary between $x = 5$ and $x = 17$ mm within the statistical error. It amounts to 27300 cps independently from the sample position. Consequently the S-parameter maps measured by detectors A and B are very similar and no asymmetry occurs showing that the geometry of the newly designed sample holder has no influence on the annihilation radiation. Since the zero adjustment of the sample holder was not correct at that time, the defected area on the sample indicated by a region with higher S-parameters lies 3 mm too far on the right hand side. Therefore a region with lower S-parameter occurs on the left which has not been detected in figure 4.6.

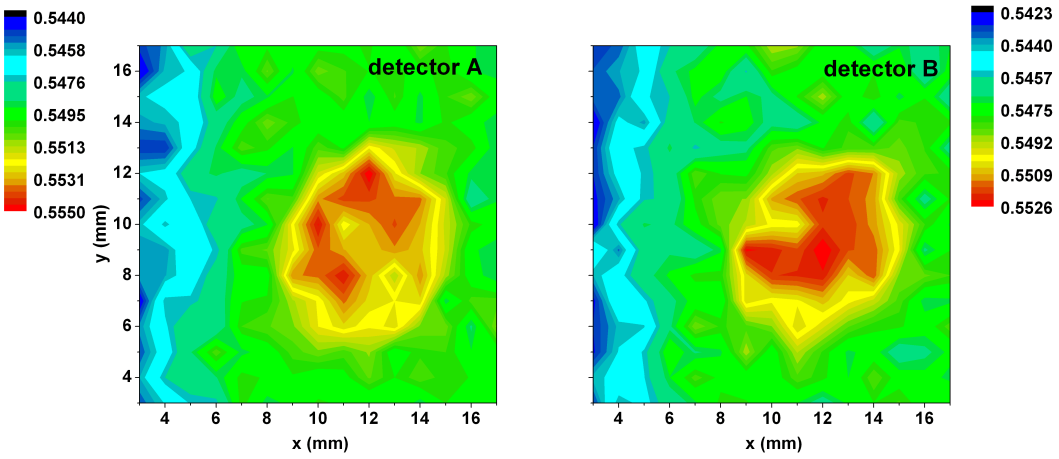

Figure 4.21: S-parameter scan of the sample which has been already measured with the CDBS1 in figure 4.6 at 17 kV sample potential and a step size of 1 mm. The analyzed data from both detectors A and B are shown, proofing that no sample position dependent variation of the count rate and therefore no asymmetry is observed with the CDBS2.

5 Measurements and discussion: ion irradiated Mg and AZ31

5.1 Motivation

Magnesium based alloys experience an increasing interest in industrial applications due to their low density and high rigidity. These parameters are not only crucial in car industry and aerospace engineering where energy efficiency enforces the use of light materials but also for the development of lightweight but durable portable electronic devices such as digital cameras, laptops and cell phones. Nevertheless the low plasticity of Mg-based alloys is one major drawback which prevents these materials from being more commonly used [91]. The macroscopic properties of these materials are strongly correlated with the microscopic structure, i. e. grain size, precipitates and particularly with defects and their chemical vicinity. CDBS is an ideal tool to investigate the latter, because changes of the stoichiometry in the vicinity of open volume defects result in variations of the characteristic electron momentum distribution.
However, Mg and its alloys are challenging materials for defect spectroscopy with positrons since it has been shown, that in Mg the positron trapping rate in defects is relatively low [83, 84] and the trapping sites are shallow [5]. Whereas the defect induced variation of the S-parameter, usually lies in the range of $4-5\,\%$ in metals such as Cu or Al, thermally induced defects in Mg only cause an increase of $0.6\,\%$ in the S-parameter [92].
The goal of this work is to investigate the chemical surrounding of defects in the magnesium based alloy AZ31 which consists of Mg with 3 wt. % Al and 1 wt. % Zn. Therefore a well known defect distribution has to be created in the respective samples. This has been performed by implanting ions. The near equilibrium solubility of atoms in light metals and the high mobility of point defects [93] lead to the educated guess, that ion bombardment of AZ31 with Mg-ions could cause the formation of defect clusters with a chemical vicinity deviant from the bulk material. A similar effect has been observed for reactor pressure vessel steels, where the irradiation with fast neutrons induces mobile defects, which encounter Cu atoms and form vacancy-Cu complexes [11].
The investigation of defect containing ternary alloys such as ion irradiated AZ31

with CDBS is not straight forward, since the elemental contribution of three different elements and the changes in the electron momentum distribution due to defects have to be thoroughly separated as explained in 3.3. In order to measure changes of the stoichiometry in the vicinity of defects in AZ31, samples of pure Mg have been irradiated with Mg-ions in order to create exclusively defects and to observe the respective change of the 511 keV-annihilation line. Another set of Mg-samples has been irradiated with Al- and Zn-ions to investigate the shape change of the annihilation line, if these atoms agglomerate in the vicinity of open volume defects. A comparison with Mg-ion irradiated AZ31-samples should then reveal possible changes of the stoichiometry in the vicinity of defects.

5.2 The physical properties of Mg and AZ31

Magnesium as a pure metal exists in hexagonal closed packed structure with the lattice constants $a_{\mathrm{RT}} = 0.321$ and $c_{\mathrm{RT}} = 0.521\,\mathrm{nm}$. The melting temperature is $T_{\mathrm{m}} = 650\,^{\circ}\mathrm{C}$ [94]. Compared to Al, the density of Mg is by a factor of 1.55 smaller, namely $1.738\,\mathrm{g/cm^3}$. Since pure Mg from casting only has a tensile strength of $107\,\mathrm{N/mm^2}$, alloy constituents have to be added in order to increase this value. By adding for example 3 wt. % Al, the tensile strength increases to $245\,\mathrm{N/mm^2}$. The addition of Zn does not further increase the tensile strength but the ductility such that a maximum strain of 14 % is achievable with 1 wt. % Zn. An example for such a system is the wrought alloy AZ31 with an elastic limit of $177\,\mathrm{N/mm^2}$, a tensile strength of $265\,\mathrm{N/mm^2}$ and a maximum possible strain of 14 % [95].
The grain size of annealed AZ31 varies between 50 µm and 700 µm in contrast to rapidly quenched AZ31 where values below 1 µm are typical [96]. These Zn-containing grains are surrounded by a so called perlit phase, which consists of $Mg_{17}Al_{12}$. Since the positron diffusion length of $\sim 100\,\mathrm{nm}$ is orders of magnitudes smaller than the grain size, the influence of positron trapping in grain boundaries is negligible.

5.3 Sample preparation

Samples of pure Mg and AZ31 have been used for the investigations of the present work. From the as received materials, pieces with $20 \times 20 \times 3\,\mathrm{mm^3}$ were produced which fit into the sample holder of the CDBS1- and CDBS2-spectrometers at NEPOMUC. Every sample has been polished with 4000 grit abrasive SiC-paper. Subsequently the AZ31-samples and one Mg-sample were Syton-polished (SiO_2-

particles), whereas all other Mg-samples were polished with diamond polish paste (grainsize between 1 and 3 µm). These polishing procedures may cause defects at the surface. Nevertheless, the presented measurements are still valid, since the bulk properties of the samples remain unchanged, as it has been observed in energy dependent DBS-measurements (see section 5.4.1). In order to ensure, that all samples are defect free before the ion implantation (despite the surface), they have been annealed in a CO_2-atmosphere with a pressure of 1 bar for 1 h. The temperature was set to 693 K for the Mg-samples, whereas the AZ31-samples were annealed at 653 K. For temperatures higher than 400 K even defect clusters are completely removed in Mg [94]. Rapid quenching of the samples after annealing as a solution treatment has been avoided, since this treatment could lead to thermally induced formation of defects which then may remain present and would perturb the measurements. The annealing of AZ31 without quenching leads to a distinct grain growth [97].
The penetration depth of positrons is given by the Makhovian profile for low energies as described in section 2.2.1:

$$\bar{z} = \frac{A}{\rho} \cdot E_+^n$$

where A and n are theoretically determined material dependent parameters, and E represents the energy of the positrons in keV. For the presented measurements on Mg and AZ31 the values for aluminum $A = 3.7\,\mu g/cm^2 keV^{-n}$ and $n = 1.67$ have been used [3]. With the density $\rho = 1.74\,g/cm^3$ of magnesium the mean penetration depth of positrons lies in the range between 0.02 and 6.3 µm for positron energies between 1 and 31 keV.
The ion irradiation was performed at the 3 MeV-Tandetron in Rossendorf [98], where a maximum mean implantation depth for Zn-ions into Mg and AZ31 of 2.3 µm was achievable as shown in figure 5.1. The depth range of this vacancy and ion distribution is covered with both versions of the CDBS, since their sample potential is adjustable between 0 and −30 kV. The figure was obtained by simulating the ion and vacancy distribution in a Mg-sample with the program SRIM-2003 [99]. Additionally the Makhovian profile for positrons with 17 keV is plotted as a solid line. In order to achieve an equally shaped ion distribution for the Mg- and Al-ions, the respective energy of the ion beam was set to 1.4 and 1.6 MeV (see figure 5.2).

Since both versions of the CDBS-facility at NEPOMUC allow spatially resolved measurements with a lateral resolution of 1 to 2 mm, the diameter of the ion beam was reduced to 5 mm by an aperture in order to irradiate exclusively the central region of the samples (figure 5.3). However, with this small beam diameter the ion dose could not be measured with the permanently installed Faraday cup in the implantation chamber of the Tandetron for the described samples, since it has been

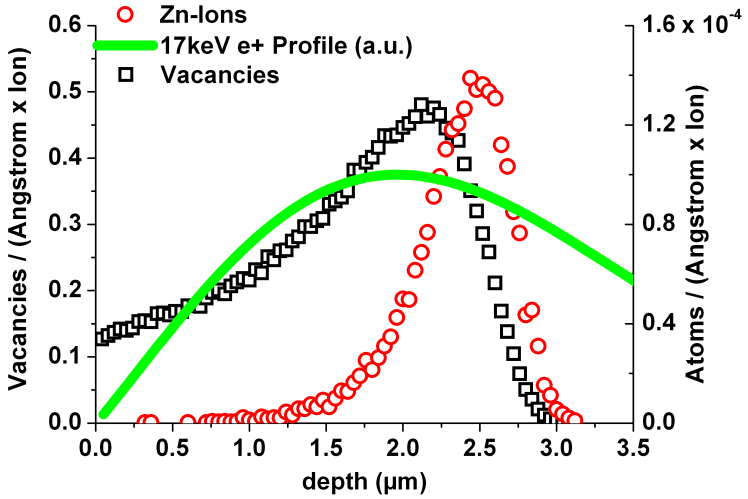

Figure 5.1: Vacancy and Zn-ion distribution in Mg as simulated with SRIM (energy of the ions: 3 MeV). The solid line represents the Makhovian implantation profile of 17 keV-positrons.

optimized for scanning the ion beam over wafers with a diameter of 50.8 mm for implanting and doping purposes. Using a simple aperture with a 5 mm hole and adjusting the scanning area of the ion beam such that the Faraday cup is included would increase the necessary beam time unacceptably. Therefore an aperture was constructed which consists of 4 plates with 7-, 10-, 5- and 8 mm-holes (see figure 5.4). The different sizes of the holes in the first and third plate allow a reliable dose measurement via measuring the current at the third plate. The second and the fourth plate are used to screen secondary electrons by applying a potential of -60 V.

For the present work the four doses $3\cdot10^{13}$, $3\cdot10^{14}$, $3\cdot10^{15}$ and $3\cdot10^{16}$ ions/cm^2 have been applied to four samples each as denoted in table 5.1 which lists all produced samples together with the labels used in this text. In table 5.1 these irradiated samples except the reference materials are listed together with labels, which are used in the text.

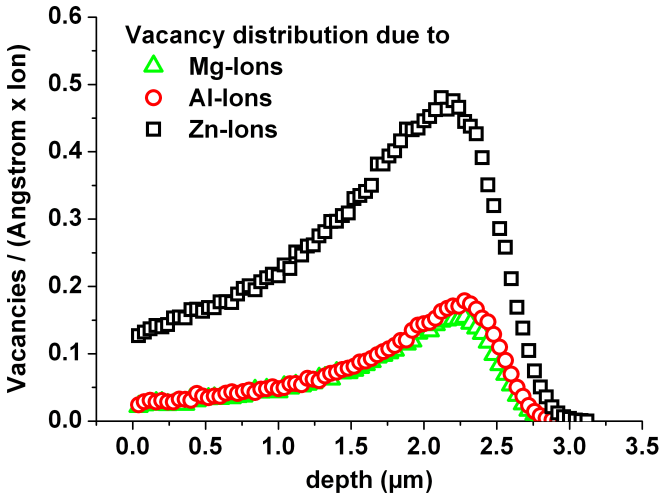

Figure 5.2: Vacancy distribution in Mg as simulated with SRIM after irradiation with Mg-, Al- and Zn-ions. The Zn-ions cause the highest vacancy concentration.

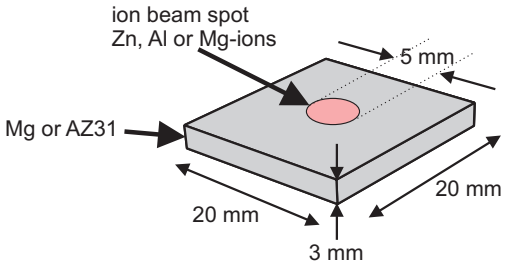

Figure 5.3: Schematic drawing of the ion irradiated samples. The polished and annealed Mg-samples were irradiated with Al-, Zn- and Mg-ions, whereas the AZ31 sample was irradiated only with Mg-ions. For each ion type and sample material doses between $3{\cdot}10^{13}$ and $3 \cdot 10^{16}$ ions/cm^{-2} have been applied (see table 5.1).

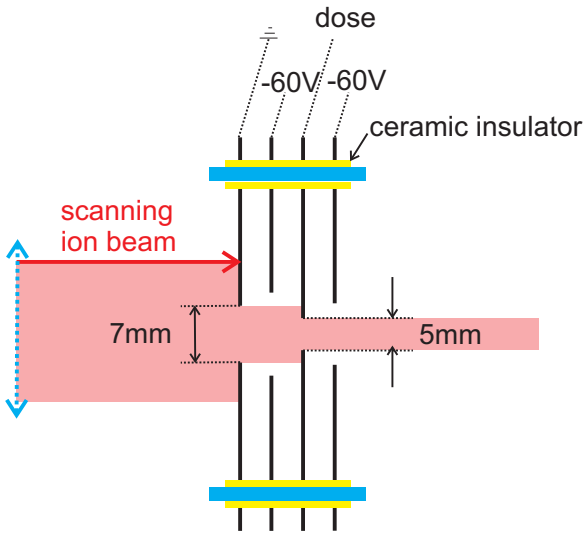

Figure 5.4: Schematic view of the 4-plate aperture. The different sizes of the holes in the first and third plate allow a reliable dose measurement, while the second and the fourth plate reduce the secondary electron background.

Table 5.1: List of all samples except the reference materials with labels, which are used in the text.

Ion Type	Dose (cm^{-2})	Sample	Label
Mg^+ (1.4 MeV)	$3 \cdot 10^{13}$	Mg	Mg_{13}/Mg
Al^+ (1.6 MeV)		Mg	Al_{13}/Mg
Zn^+ (3.0 MeV)		Mg	Zn_{13}/Mg
Mg^+ (1.4 MeV)		AZ31	Mg_{13}/AZ31
Mg^+	$3 \cdot 10^{14}$	Mg	Mg_{14}/Mg
Al^+		Mg	Al_{14}/Mg
Zn^+		Mg	Zn_{14}/Mg
Mg^+		AZ31	Mg_{14}/AZ31
Mg^+	$3 \cdot 10^{15}$	Mg	Mg_{15}/Mg
Al^+		Mg	Al_{15}/Mg
Zn^+		Mg	Zn_{15}/Mg
Mg^+		AZ31	Mg_{15}/AZ31
Mg^+	$3 \cdot 10^{16}$	Mg	Mg_{16}/Mg
Al^+		Mg	Al_{16}/Mg
Zn^+		Mg	Zn_{16}/Mg
Mg^+		AZ31	Mg_{16}/AZ31

5.4 Measurements with the CDBS1

The major part of the measurements described in the following section has been published in [76]. Firstly, DBS-measurements have been performed with the CDBS1 on all samples, as a function of the positron energy, i.e. the S-parameter S(E) reveals depth dependent information within the Makhov-profile. Secondly, spatially resolved two-dimensional S-parameter scans with respect to the position of the positron beam on the sample S(x,y) with a stepsize of 1 mm have been performed. After that, each sample has been investigated with CDBS. The positron energy for the latter measurements was set to 17 keV in order to maximize the overlap with the ion implantation induced defect distribution.

5.4.1 DBS-Measurements as a function of the positron energy - S(E)

Measurements of the S-parameter as a function of the positron energy in the irradiated area as well as in the untreated region were performed for all samples, listed in table 5.1. The energy resolution at 477.6 keV was 1.3 keV. For the 511 keV annihilation line the photopeak count rate was typically 2500 cps (total count rate: 14000 cps). Hence about $5 \cdot 10^5$ counts were collected during a measurement time of 3 min. Figure 5.5 compares the untreated with the Zn-ion irradiated region of the Zn_{14}/Mg-sample, which has been polished like the AZ31-samples. The shape of this curve for low positron energies between 1 and 10 keV was found to be strongly dependent on the polishing procedure. However, for bulk investigations this positron energy range is not relevant.

The S-parameter differs at the sample surface (between 1 and roughly 4 keV) and for larger positron penetration depths (between 9 and 29 keV). This is ascribed to defects which have been created during the irradiation procedure. Since the defect profile stretches to the surface as shown in figure 5.2, the positrons are trapped in defects and hence detained from diffusing back to the surface which reduces the rising of the S-parameter at low sample potentials, i.e. low energies and therefore very small positron penetration depths. According to figure 5.2, the defect density is five times smaller at the surface than in the bulk, thus proofing that also for these reduced defect concentrations an effect is detectable.
In the bulk region, the defects result in a higher S-parameter compared to the untreated bulk region, since defects cause a smaller line shape and hence an increase of the S-parameter [100].
The difference between the two curves reaches its maximum between 13 and 21 keV, whereas for higher positron energies it starts to decrease, which is ascribed to the

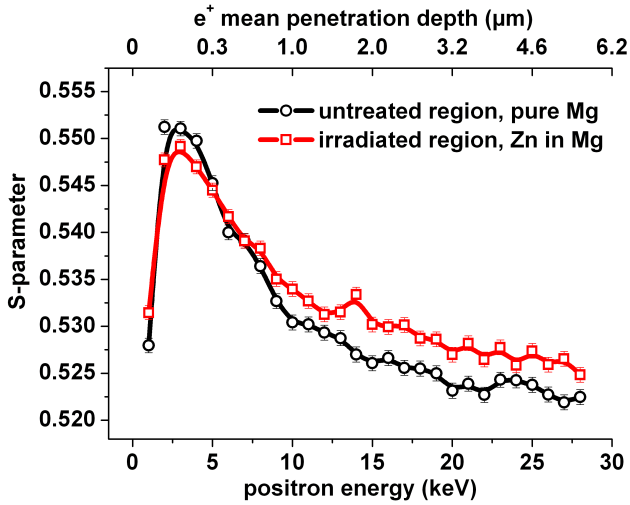

Figure 5.5: S-parameter as a function of the positron energy measured for the Zn_{14}/Mg-sample in comparison to untreated pure Mg. The two curves differ at the surface (between 1 and roughly 4 keV) and for greater positron penetration depths (between 9 and 28 keV). The latter behavior is attributed to the irradiation induced defect distribution as shown in figure 5.2. The solid lines serve as an eye guide.

shape of the vacancy distribution as shown in figure 5.2 with a maximum defect concentration at 2.3 µm equal to 17 keV positron energy. The samples Mg_{14}/Mg, Al_{14}/Mg and Mg/$AZ31_{14}$ show a similar behavior in the bulk region but less distinct in agreement with the smaller produced vacancy distribution according to figure 5.2.
Since the applied ion dose and the resulting vacancy distribution are correlated, S(E)-curves have been measured on the Mg_i/Mg-samples with i = 13, 14, 15. The samples with the highest dose, i. e. $3 \cdot 10^{16}$ ions/cm^{-2}, have been excluded from this particular study since due to the extreme dose amorphization and local annealing occurred as will be explained later in this section. Whereas the Mg/Mg_{13}-sample reveals no significant increase of the S-parameter for positron energies larger than 8 keV, the Mg_{14}/Mg-sample deviates from annealed Mg between 12 and 22 keV by $\sim 0.5\,\%$ due to the created defect distribution (see figure 5.6). The effect gets more pronounced for the higher implantation dose of the Mg_{15}/Mg-sample on which beginning at 8 keV the deviation from annealed Mg increases to $\sim 0.5\,\%$ at maximum. These results are in very good agreement with the simulated defect distribution with a maximum created defect concentration at $\sim 2.3\,\mu$m. For positron energies below 10 keV the slopes of the curves could be a consequence of the increasing positron beam diameter in this energy range, thus leading to a partial annihilation of positrons in ion-unaffected sample material.

Due to the partial annealing of monovacancies in Mg and the presence of an unknown quantity of defect clusters—which survive up to 400 K [94]—a determination of the actual defect concentration is not possible with these S(E)-curves. For this purpose positron lifetime measurements are necessary.
The shapes of the S(E)-curves in figures 5.5 and 5.6 do not match for low positron energies which is a consequence of the different polishing procedures of the respective samples as explained in 5.3.

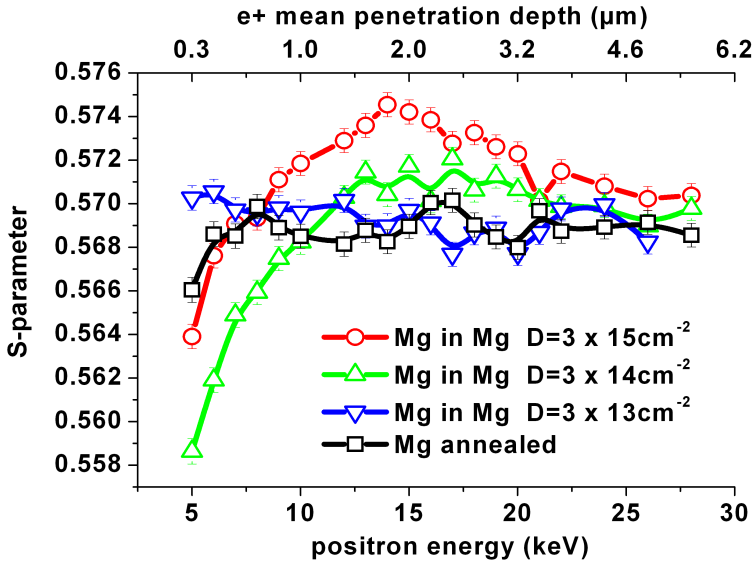

Figure 5.6: S(E)-curves measured from 5 to 28 keV on the Mg/Mg_i-samples with i = 13, 14, 15 in order to show the effect of varying ion dose. Whereas the Mg/Mg_{13}-sample reveals no significant increase of the S-parameter for positron energies larger than 8 keV, the S(E)-curves from the Mg_{14}/Mg- and Mg_{14}/Mg-samples deviate significantly from annealed Mg in the bulk region.

5.4.2 Laterally resolved DBS-measurements - S(x,y)

In order to image the irradiated region on the samples, the S-parameter has been recorded depending on the position of the positron beam for all samples at various potentials. A region of 15 × 15 mm^2 has been scanned with a step size of 1 mm. The measurement time per point was 3 min with a count rate of 2800 cts/s in the 511 keV-photopeak resulting in the same energy resolution as in the above mentioned S(E)-measurements. The result for the Zn_{14}/Mg-sample is shown in figure 5.7, for which the difference between the irradiated and the untreated region is very distinct. In order to suppress the asymmetry of the CDBS1 (refer to section 4.3), the S-parameters from both detectors have been used to calculate a mean

S-parameter. This procedure does not interfere with the initial intention of this measurement, namely imaging the ion beam spot. The minimum S-parameter value is set to 0.54 for every picture, and the color map ranges up to 0.547. At 5 kV sample potential (6 keV positron energy) the irradiated region is almost not visible besides an area with slightly decreased S-parameter as expected from the S(E)-measurements (figure 5.5). For 10 kV sample potential the area affected by the ion beam spot is clearly detectable. The maximum S-parameter deviation in this picture amounts to 1 %, whereas for 20 kV the irradiated region is even more distinctly reproducible with a maximum S-parameter contrast of 1.3 %. Also the diameter of the irradiated area matches the size of the ion beam of 5 mm within the spatial resolution of the CDB-spectrometer. Since trapping in monovacancies in Mg is expected to be inefficient [84, 5, 83, 101], the visibility of the ion affected area in figure 5.7 most probably results from trapping in defect clusters.

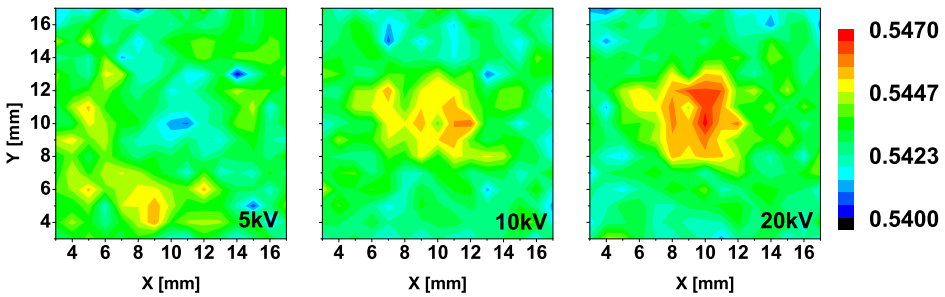

Figure 5.7: S-parameter as a function of the positron beam position on the Zn_{14}/Mg-sample at various sample potentials (step size 1 mm). The minimum S-parameter for every picture was set to 0.54 in order to use an identical color scale which ranges from 0.54 to 0.547 in arbitrary units. At 5 kV the ion beam spot is not detectable, whereas at 10 kV the irradiated region already becomes visible (max. S-deviation 1 %). For 20 kV the ion beam spot is clearly reproducible as expected from the above described S(E)-measurements.

For the samples with the highest dose, this measurement revealed an unexpected behavior as shown exemplary on the Mg_{16}/AZ31-sample in figure 5.8 where the S-parameter has been recorded as a function of the lateral position with a step size of 2 mm. In contrary to figure 5.7 the S-parameters are plotted in three dimensional plots. The tendency to lower S-values for higher positron energies results from the shape of the S(E)-curve, which is similar to the S(E)-curve of the Zn_{14}/Mg-sample due to the same polishing. Besides that, an ion beam induced change of the S-parameter can only be found for low positron energies, i.e. smaller than 6 keV. Above this energy, no significant variation of the S-parameter between

the irradiated and the untreated area is detectable. This effect is ascribed to the very high ion dose which has led to local annealing effects and therefore the SRIM-simulated defect distribution do not represent the defect distribution [82]. Therefore, the samples with the highest irradiation dose have not been used for the interpretation of the results of this work.

5.4.3 Coincident Doppler broadening measurements - CDBS

Firstly, polished and annealed samples of pure Mg, Al, Zn and AZ31 have been investigated with CDBS in order to record the characteristic shape of the annihilation line and in particular the high momentum region for each material. A sample potential of 25 kV for the light materials ensured, that all positrons annihilate in the bulk, whereas the sample potential for the Zn-measurement was set to 28 kV, because S(E)-measurements on annealed Zn showed, that at 25 kV the bulk S-parameter was not fully reached. In order to increase statistics, both sides of the symmetric photopeak are used for data treatment, i.e. the red shifted side ($E < E_0 = 511\,\mathrm{keV}$) of the peak is mirrored at E_0 and added to the blue shifted side ($E > E_0$). Afterward, ratio curves have been calculated as described in section 3.3 with respect to annealed Mg. The error bars are determined by applying the Gaussian error propagation law to the described data treatment. In order to minimize the large error bars due to low statistics for momenta higher than $15 \cdot 10^{-3}\,\mathrm{m_0c}$, the bin size is increased from 56.7 eV/bin to 283.5 eV/bin. The spectra contain $1 - 2 \cdot 10^7$ counts and were recorded with 1.3 keV energy resolution at 477.6 keV for each detector.
In figure 5.9 the CDB-ratio curves (signatures) of the annealed pure elements Al, Zn and the annealed alloy AZ31 are shown with respect to annealed Mg as a reference. The signatures of Zn and Al are clearly distinguishable from Mg, especially Zn reveals a large intensity for momenta higher than $7 \cdot 10^{-3}\,\mathrm{m_0c}$. The distinct peak in the Al-curve at $6.6 \cdot 10^{-3}\,\mathrm{m_0c}$ (according to 512.7 keV) is a consequence of the mismatching Fermi energies of Al and Mg (7.08 and 11.7 eV respectively) which lead to a Doppler shift of 1.3 and 1.7 keV respectively. A zoomed view of figure 5.9 is plotted in figure 5.10, which shows a slight deviation of the AZ31-signature with respect to pure Mg toward Zn and Al. This deviation is attributed to the presence of Zn and Al-atoms in the annealed AZ31.

Figure 5.11 presents the three CDB-curves of the irradiated Mg_{14}/Mg-, Al_{14}/Mg- and Zn_{14}/Mg-samples relative to untreated Mg. All three signatures reveal a reduced contribution of high momentum electrons, as expected due to the irradiation induced defects [100]. Hence a decline between 5 and $18 \cdot 10^{-3}\,\mathrm{m_0c}$ is observed with respect to the reference spectrum of annealed Mg. The signatures

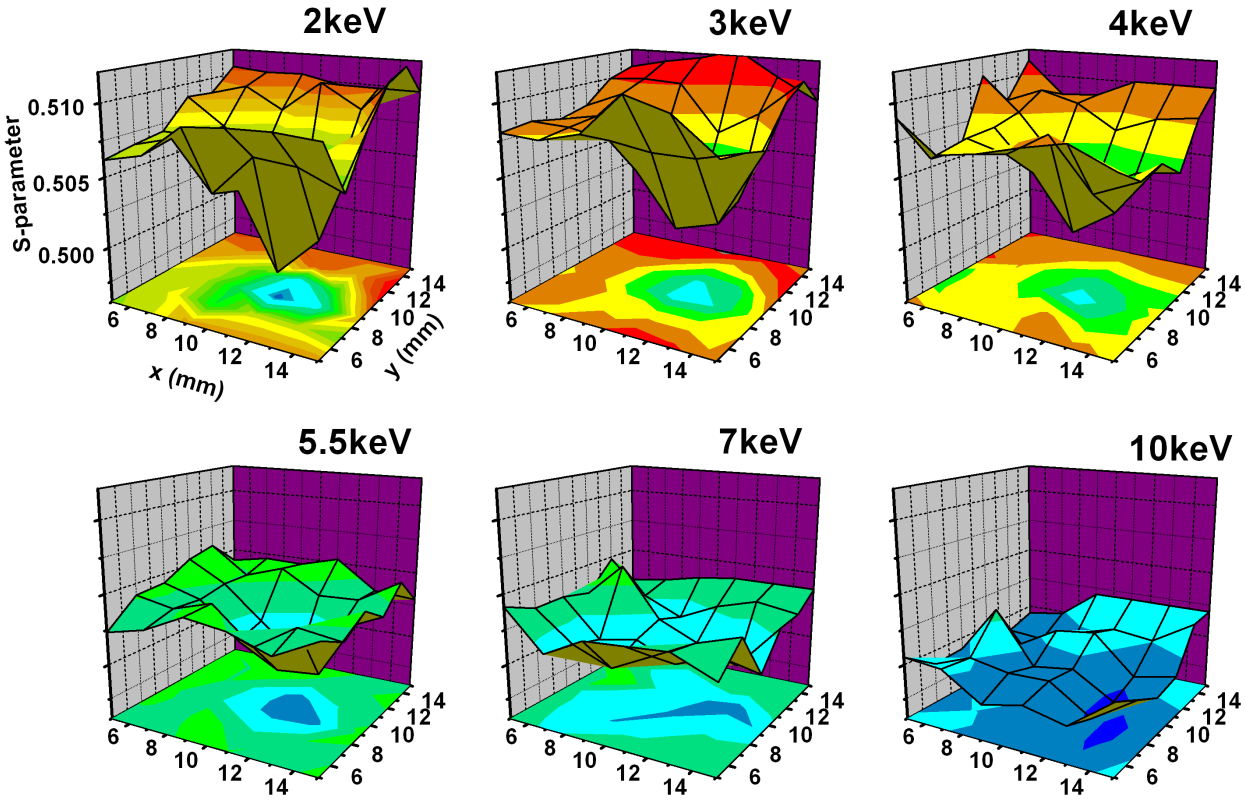

Figure 5.8: S-parameter as a function of lateral position measured on the Mg_{16}/AZ31-sample. In contrary to figure 5.7, the color map has not been shifted to equal values. Besides the tendency to lower S-values for higher positron energies according to the shape of the S(E)-curve in AZ31, the ion beam spot is detectable only for the surface region, i.e. positron energies lower than 6 keV. This effect is ascribed to the very high ion dose which has led to local annealing effects and therefore the SRIM-simulated defect distribution do not represent the defect distribution [82].

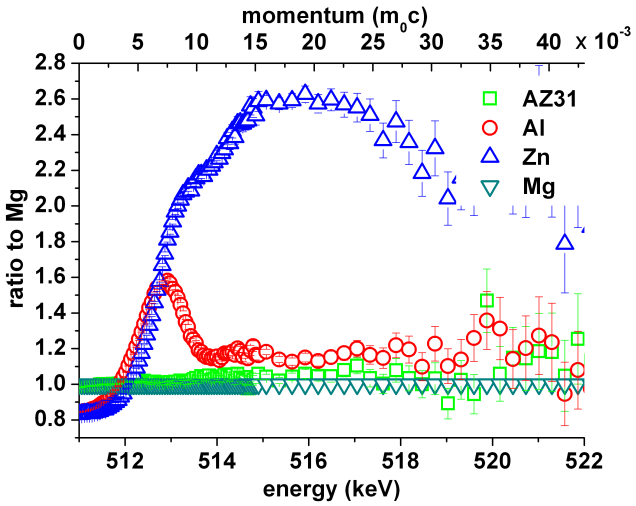

Figure 5.9: CDB ratio curves of pure and annealed Al, Zn and AZ31 relative to Mg at a sample potential of 25 kV for Mg, Al, AZ31 and 28 kV for Zn. The elements are clearly distinguishable, since Al and Zn show increased intensities in the high momentum region ($> 10 \cdot 10^{-3}\,m_o c$). The Zn-signature dominates this region.

of the Mg_{14}/Mg- and the Al_{14}/Mg-sample are similar and the Zn_{14}/Mg-sample reveals the most distinct deviation. This could be ascribed to the irradiation induced vacancy distribution, which was calculated with SRIM (see figure 5.1) in advance. The differences from unity of the Mg_{14}/Mg- and the Zn_{14}/Mg-curve scale approximately by a factor of two which is at least roughly represented by the simulated vacancy distributions. Nevertheless, SRIM only computes the initial vacancy distribution without taking annealing effects into account. Since monovacancies in Mg without a decoration with solute atoms or hydrogen anneal already below room temperature [101], but vacancy clusters survive up to 400 K, deviations occur from the direct proportionality of the simulated vacancy distributions and the differences of the measured ratio curves [94]. For a quantitative interpretation, positron lifetime measurements have to be performed in future to reveal the concentration and type of vacancies.

The Makhov-Profile as plotted in figure 5.2 shows, that 70 % of the positrons annihilate outside the ion distribution and hence only 30 % of the implanted positrons annihilate in a region, where the ion-distribution is not zero. Nevertheless, if the implanted ions accumulated in the vicinity of the created defects, the trapped positrons should also annihilate with the respective core electrons of the implanted ions and therefore the characteristic signatures should be detectable

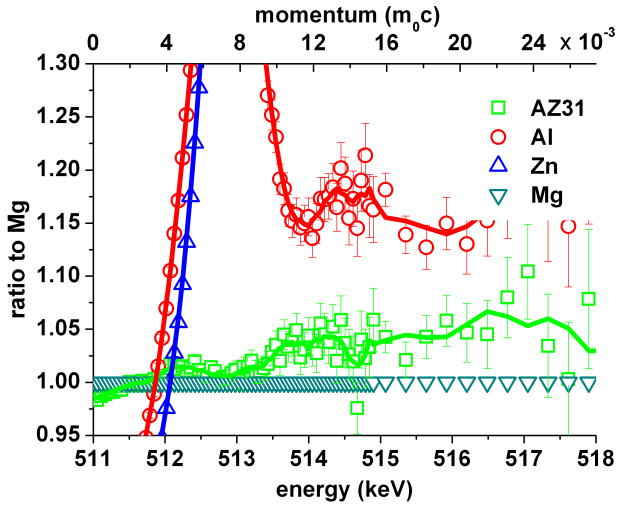

Figure 5.10: Zoom into figure 5.9. The AZ31-signature reveals a higher intensity for momenta greater than $5 \cdot 10^{-3}\,m_0c$ which is attributed to the contribution of Zn- and Al-atoms. The solid lines serve as an eye guide.

with CDBS. Due to the similar masses of Al- and Mg-ions, the resulting vacancy distributions are nearly the same according to the SRIM-simulations and hence, a similar behavior of the Al_{14}/Mg- and the Mg_{14}/Mg-curve in the high momentum region is expected. Nevertheless, due to a significant difference in this region, a decoration of the irradiation induced defects with Al-atoms is observed. In order to investigate this observation in more detail, the Mg_{14}/Mg-spectrum and the annealed Al-spectrum have been linearly combined such that the resulting curve matches the high momentum region of the Al/Mg-curve (dotted line in fig. 5.11). The pronounced peak between 4 and $10 \cdot 10^{-3}\,m_0c$ in the linearly combined curve results not from confinement of the positrons in defects, but from the mismatch of the Fermi energies as explained above, since no significant confinement peaks are visible in none of the three curves [75]. However, this analysis does not lead to quantitative results since the effect of defects in Al are neglected in this consideration.
The signature of Zn_{14}/Mg does not reveal any contribution of localized Zn-electrons, since no increase for high electron momenta is observed as expected for Zn (figure 5.9) but rather a decrease due to defects in Mg by Zn-irradiation. Moreover, its shape is similar to the Mg_{14}/Mg-curve within the statistical accuracy and only the amplitude of the deviation varies. This remarkable fact leads to the conclusion, that no Zn-ions are agglomerating in the vicinity of the irradiation induced defects. Consequently, a defect-independent distribution of the implanted ions is assumed since CDBS does not detect the respective signature due to

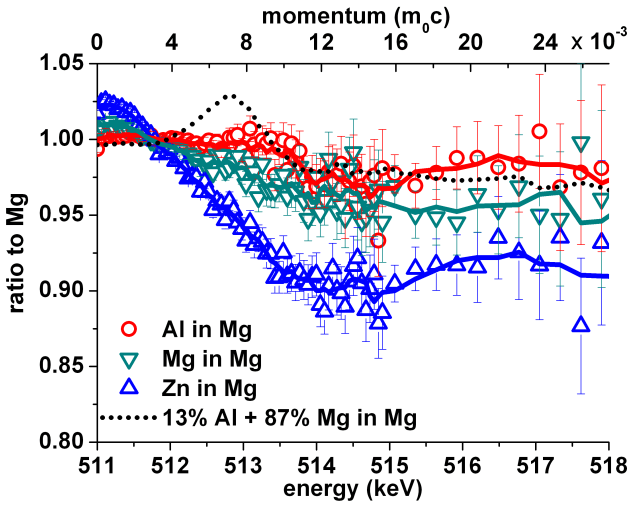

Figure 5.11: CDB ratio curves of the Mg-, Al- and Zn-ion irradiated samples with untreated Mg as a reference at 25 kV sample potential each with $3 \cdot 10^{14}\,\mathrm{cm}^{-2}$ dose. The Zn in Mg signature is more pronounced which is attributed to a higher concentration of vacancy clusters. The dotted line represents a linear combination with 13% of the pure Al-spectrum and 87% of the Mg_{14}/Mg-spectrum (see text). The solid lines serve as an eye guide.

the rather low concentration of the implanted ions. The ion concentration in the respective region amounts to $2 \cdot 10^{18}\,\mathrm{cm}^{-3}$, which equals 0.005 at % only and is hence not measurable with CDBS, since in annealed AZ31 the room temperature equilibrium concentrations of 1 % Zn are barely detectable. The same measurements have been performed on the samples with $3 \cdot 10^{15}\,\mathrm{cm}^{-2}$ irradiation dose. Besides a more pronounced appearance of the above described observations as expected from the measurements shown in figure 5.6, the same effects have been revealed.
Figure 5.12 shows the CDBS-signatures of the Mg_{14}/AZ31-sample and annealed AZ31 with annealed Mg as a reference. Both curves are identical within the error bars from 2 up to $6 \cdot 10^{-3}\,m_0c$. For higher momenta the irradiated sample reveals a distinct decline due to the created defects.

In order to account for the contribution of defects to the annihilation line of the Mg/AZ31-sample, the spectrum of Mg/AZ31 has been normalized to the Mg_{14}/Mg-spectrum. This normalization cancels out the contribution of defects in pure Mg in the high momentum region. The respective curve is plotted in figure 5.13 together with the signature of annealed AZ31 with annealed Mg as a reference. It is clearly

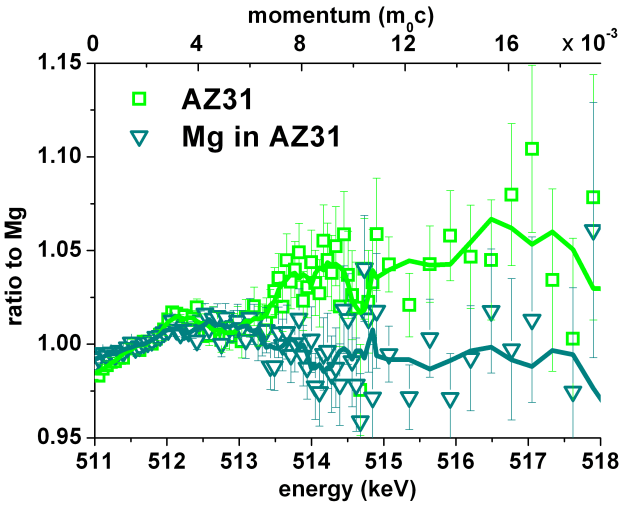

Figure 5.12: CDB ratio curve of annealed AZ31 and the Mg_{14}/AZ31-sample normalized to annealed Mg. The irradiated sample reveals a defect induced decline of the curve in the high momentum region as expected. The solid lines serve as an eye guide.

visible, that for momenta higher than $10 \cdot 10^{-3}\,m_0c$ the two curves are the same within the statistical error. The visible effects for smaller momenta are resulting from changes in the momentum distribution of the conduction electrons due to varying defect concentrations and can therefore not be used to characterize the chemical vicinity of defects.
Thus, the high momentum part of the ratio curve between annealed AZ31 and Mg does not change significantly, if both samples are irradiated with the same dose of Mg-ions. This behavior shows, that neither Zn- nor Al-atoms agglomerate in the vicinity of ion irradiation induced defects in AZ31, otherwise a significant increase in the high momentum region would be detectable, since the high momentum parts of the Zn- and Al-curves reveal higher intensities than Mg as shown in figure 5.9. Consequently, within the accuracy of the measurement, the chemical vicinity of crystal defects produced by Mg-ion irradiation remains unchanged compared to the annealed bulk material. Despite the high defect mobility in light metals, no ion-irradiation induced change of the stoichiometry in the vicinity of defects was found.
The same measurements have been performed on the samples with $3 \cdot 10^{15}\,cm^{-2}$ irradiation dose. In agreement with the above observations, no agglomeration of Zn- nor Al-atoms has been detected.

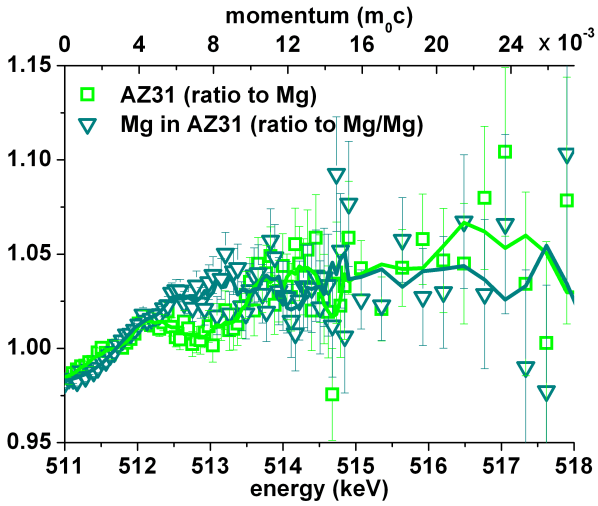

Figure 5.13: CDB ratio curve of annealed AZ31 (with annealed Mg as a reference) and the Mg_{14}/AZ31-sample (with Mg_{14}/Mg as a reference). Both signatures are identical within the statistical error. For interpretation see text. The solid lines serve as an eye guide.

5.5 Measurements with the CDBS2 at 76 K

After the CDBS2 has been set into operation in October 2007, it has been used for first measurements on the ion irradiated Mg- and AZ31-samples described in section 5.3. The main purpose was the reduction of the sample temperature in order to overcome the low trapping rate of positrons in monovacancies in Mg due to their shallowness [83, 84, 5, 101].

5.5.1 DBS-Measurements as a function of the positron energy - S(E)

The measurements on the Zn_{14}/Mg-sample have been repeated with the CDBS2 at room temperature and at 76 K in order to achieve temperature dependent S(E)-curves which can be directly compared (see figure 5.14). At room temperature, the S(E)-curves of the ion irradiated and the unaffected region on the Zn_{14}/Mg-sample behave similar to the measurements performed with the CDBS1. Besides a pronounced peak between 1 and 8 keV which stems from the near surface defect layer due to polishing, a distinct difference between both regions can be observed between 8 and 30 keV. Since at least for positron energies above 5 keV a focal diam-

eter of 1 mm has been measured, the earth magnetic field induced beam shift does not play a role due to the 5 mm diameter of the irradiated region. The curves measured with the CDBS2 appear more clearly than in the CDBS1 measurement. For example at 17 keV positron energy, the relative difference amounts to 1.3 % whereas in the CDBS1-measurement shown in figure 5.5 this value was only 0.8 %. This is attributed to the optimized detector and sample holder geometry, less small angle scattering and the sample position independent resolution of the γ-spectroscopy system.

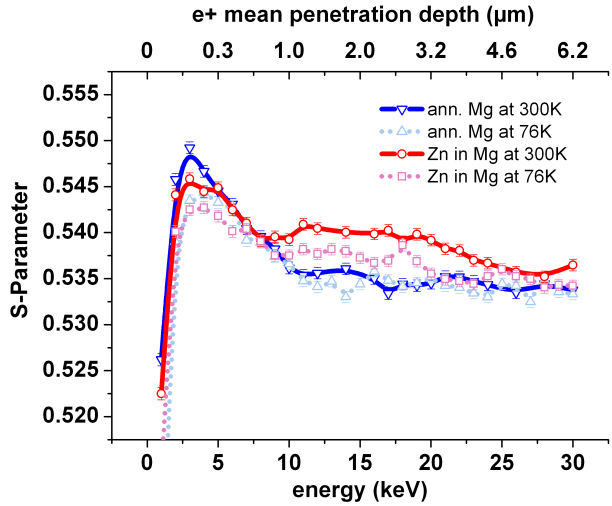

Figure 5.14: S(E)-measurement on the Zn_{14}/Mg-sample with the CBDS2 at room temperature and at 76 K. At room temperature, the S(E)-curves of the irradiated and the untreated region on the Zn_{14}/Mg-sample behave similar to the measurements performed with the CDBS1. Furthermore, the curves of the untreated regions (annealed Mg) at room temperature and at 76 K are nearly identical between 6 and 30 keV. This behavior shows, that the decreased lattice constant at 76 K does not have a major influence on the S-parameter. Due to the less pronounced deviation of the irradiated region from annealed Mg at 76 K compared to room temperature, an influence of the Zn-atoms and monovacancies has to be taken into account. For further explanations see text.

At 76 K the following observations have been made: The curves of the untreated regions (annealed Mg) at room temperature and at 76 K are nearly identical between 6 and 30 keV. This behavior shows, that the decreased lattice constant at 76 K does not have a major influence on the S-parameter. The adsorption of rest gas on the surface of the sample is expected to be low (pressure: $\sim 5 \cdot 10^{-7}$ mbar). However, the differences for low positron energies between room temperature and 76 K in the ion unaffected region stem from this effect.
Whereas the irradiated region at room temperature differs strongly from the an-

nealed Mg-curve due to the created defects, the same measurement at 76 K leads to a much smaller deviation. This is remarkable since a more efficient trapping of positrons is expected for low temperatures and the diffusion length of positrons is increased by a factor of 1.5 to roughly 150 nm as explained in section 2.2.2 thus leading to a more pronounced probability for positrons to diffuse to a defect. The contrary is observed which may be due to two different effects. Firstly one can assume that besides defect clusters also monovacancies are present which should not influence measurements at room temperature due to their shallowness. For low temperatures, i.e. low enough to trap positrons therein, hydrogen-decorated monovacancies [101] have to be taken into account, thus leading to a higher contribution of high momentum electrons—namely a lower S-parameter[1]. Secondly, the contribution of Zn-atoms could play a role, assuming that solute monovacancy complexes are formed consisting of Zn-atoms and monovacancies. The distinctively higher momenta of the Zn core electrons lead to a more dominant contribution of high momentum electrons and consequently to a lower S-parameter. S(E)-measurements are not capable to distinguish between these contributions; this has been performed with CDBS in section 5.5.3.

5.5.2 Laterally resolved DBS-measurements - S(x,y)

The Zn_{14}/Mg-sample has been two dimensionally scanned at 76 K for 7, 14 and 22 keV positron energy in order to verify the above mentioned S(E)-measurements (see figure 5.15). As expected from these measurements, a slightly decreased S-parameter at the irradiated region according to the reduced surface values is revealed for 7 keV positron energy and for 14 keV the irradiated area is most distinctively visible. For 22 keV the ion beam spot could not be reproduced.
Two dimensional scans with the CDBS2 at room temperature on the same sample are shown in figure 4.21.

5.5.3 Coincident Doppler broadening measurements - CDBS

In order to clarify whether the observation from the S(E)-measurements at 76 K on the Zn_{14}/Mg-sample result solely from positron trapping in hydrogen-decorated monovacancies or from an increased contribution of Zn-atoms in the vicinity of vacancies, CDBS-measurements have been performed at 17 keV positron energy with the CDBS2 at 76 K as shown in figure 5.16. The contribution of high momentum electrons is clearly reduced for the low temperature measurement as ex-

[1] Since monovacancies are geometrically smaller compared to defect clusters, the annihilation with localized core electrons becomes more dominant.

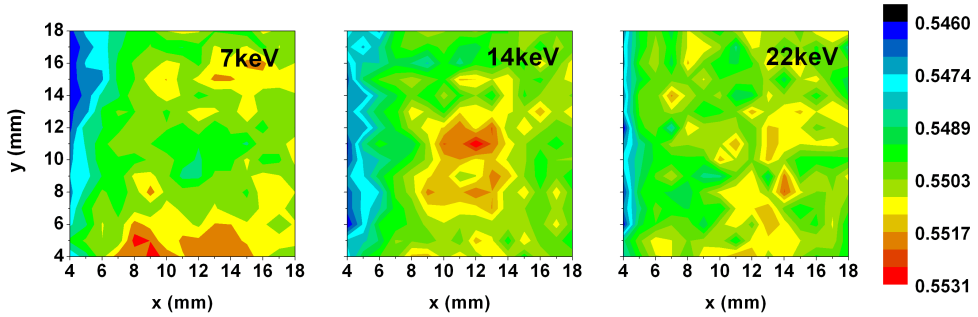

Figure 5.15: Two dimensional scan on the Zn_{14}/Mg-sample at 76 K. Similar to the measurement presented in figure 5.7, the color scale has been shifted to equal values. As expected from the S(E)-curves in figure 5.14, the ion beam spot is clearly detectable for 14 keV positron energy, in contrary to 22 keV. At 7 keV a slightly decreased S-parameter is observed in the irradiated region according to the S(E)-curves.

pected from the respective S(E)-curve. Besides that the Zn-characteristic dominant increase of the ratio curve between 5 and $15 \cdot 10^{-3}\, m_0c$ is not detectable in the low temperature ratio curve of the Zn_{14}/Mg-sample, thus showing, that no Zn-monovacancy complexes have been formed in this sample during the irradiation procedure. The smaller S-parameter in the irradiated region as it has been observed in figure 5.14 could be therefore a consequence of the annihilation of positrons in hydrogen-decorated monovacancies without a decoration with Zn-atoms.
Due to the limited beam time, the other irradiated samples have not been measured so far with the CDBS2 at low temperatures. Especially the investigation of the Mg_i/AZ31-samples would be very interesting since a Zn-monovacancy complex in AZ31 has not been excluded so far.

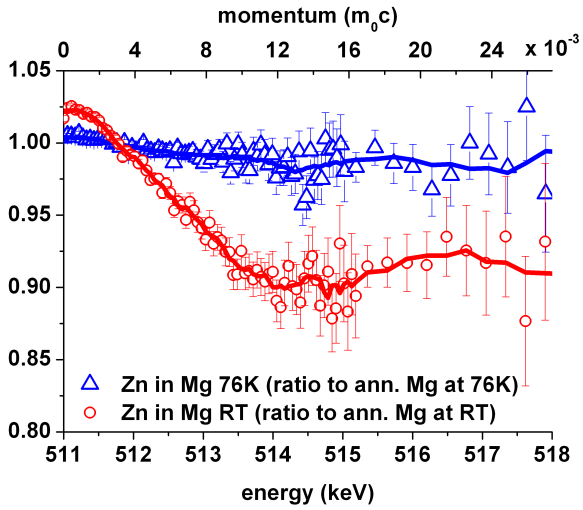

Figure 5.16: CDBS-measurement of the Zn_{14}/Mg-sample normalized to annealed Mg at 76 K. Compared to the measurement at room temperature, the ratio curve is shifted to higher momenta toward Zn. Nevertheless, the characteristic signature of Zn, i.e. a significant increase between 5 and $10 \cdot 10^{-3}\,m_0c$ is not detectable.

6 Conclusion and outlook

The irradiation of Mg- and AZ31-samples with Mg-, Al- and Zn-samples leads to a change in the width of the annihilation line in Doppler broadening measurements as shown in the previous chapter with spatial resolved measurements. The ion beam spot could be clearly reproduced in agreement with the resolution of the CDB-spectrometer. By adjusting the positron energy and therefore their mean penetration depth up to 5.5 µm, the ion irradiation induced vacancy distribution was found to be in good agreement with the previously performed SRIM-simulations. Furthermore, the deviation from non-irradiated Mg in the energy dependent Doppler broadening curves is directly correlated with the applied ion dose. Nevertheless, a quantitative estimation of the resulting vacancy concentration is hindered by the annealing behavior of Mg at room temperature.
Coincident Doppler broadening measurements on the pure and annealed metals Mg, Al and Zn revealed clearly separable CDB-ratio curves. Moreover the ratio curve of AZ31 is distinguishable from pure and annealed Mg due to the small fractions of Al and Zn.
Ion irradiated Mg has been examined with CDBS in order to investigate, whether the irradiation induced defects in annealed Mg form vacancy clusters and furthermore, whether the implanted ions are agglomerating in their vicinity. It was shown, that the implantation with Mg- and Al-ions led to a less distinct change of the shape of the annihilation line compared to the irradiation with Zn-ions. This was explained qualitatively with the aid of SRIM-simulations, which clearly showed, that the Zn-ions create a two times higher integrated vacancy concentration due to their larger mass. The characteristic signature of Zn was not observed in these spectra which leads to the conclusion, that within the accuracy of the measurement the implanted Zn-ions do not agglomerate in the vicinity of the defect clusters, whereas a decoration of the irradiation induced defects with Al-atoms was observed.
The Mg-ion irradiation induced defects in AZ31 were analyzed with CDBS as well. The ratio curves distinctively revealed, that the defects led to a change in the shape of the annihilation line. In order to account for this defect contribution, the annihilation line of the Mg-ion irradiated AZ31 was normalized to Mg-ion irradiated Mg, which exclusively contains defects with no other elemental signature. The resulting ratio curve is in the high momentum region (above the Fermi energy where only core electrons contribute to the annihilation process) no longer

distinguishable from the ratio curve of annealed AZ31 normalized to annealed Mg. In contrast to reactor pressure vessel steels, where neutron damage leads to Cu aggregations in the Fe matrix [11], this result shows that in annealed AZ31 neither Al nor Zn agglomerate in the vicinity of the ion irradiation induced defects within the accuracy of the measurement, despite the high mobility of defects in light metals. Ab-initio calculations would help to gain a more theoretical understanding of the results. However, due to the hcp-structure of Mg and the presence of vacancy clusters in the samples such computations are very demanding [78].
With the improved and extended version of the CBDS energy dependent Doppler broadening measurements have been performed at 76 K sample temperature in order to overcome the low trapping rate and the shallowness of monovacancies in Mg. The difference of the positron energy dependent Doppler broadening curves S(E) in Zn-ion irradiated Mg turned out to be less pronounced than at room temperature which was explained with the presence of two different defect types, namely hydrogen-decorated monovacancies and defect clusters, thus leading to a temperature dependent trapping. Since the contribution of high momentum electrons in monovacancies is increased compared to defect clusters, the Doppler broadening leads to a wider annihilation line and therefore smaller differences to the bulk material. It has been shown with CDBS measurements at low temperatures that this effect does not result from annihilations with Zn-atoms, otherwise the characteristic shape of Zn in the high momentum range of the annihilation line would have been detected in this measurement.
Since it is not straight forward to distinguish between different defect types and the absolute defect concentration with Doppler broadening measurements, positron lifetime spectroscopy has to be applied. The pulsed low energy positron system PLEPS [102] has been recently installed at the positron source NEPOMUC and will be soon set into routine operation. It is planned to use it for further investigation on the samples described in this paper. Lifetime measurements are capable to distinguish between different defect types which is crucial to substantiate the observations from the measurements at 76 K with the second version of the CDBS, which lead to the assumption that at least two different types of defects are present in the ion irradiated Mg-samples.

A The statistical error in S-parameter measurements

Error calculation of the S-parameter is based on Gaussian error propagation. Let A and B be the central region and the remaining part of the annihilation line respectively as indicated in figure 3.3. The error of S is then given as

$$\Delta S = \sqrt{\left(\frac{dS}{dA}\right)^2 (\Delta A)^2 + \left(\frac{dS}{dB}\right)^2 (\Delta B)^2} = \tag{A.1}$$

$$= \sqrt{\left(\frac{dS}{dA}\right)^2 A + \left(\frac{dS}{dB}\right)^2 B} \tag{A.2}$$

since $\Delta A = \sqrt{A}$ and $\Delta B = \sqrt{B}$ according to Poisson statistics. With the identities $N = A + B$, $B = N(1 - S)$ and $1 - S = \frac{B}{A+B}$ follows

$$\Delta S = \sqrt{\frac{AB^2}{(A+B)^4} + \frac{A^2 B}{(A+B)^4}} \tag{A.3}$$

$$= \sqrt{\frac{S(1-S)}{N}} \,. \tag{A.4}$$

The smallest error of S is achieved, if

$$\frac{d(\Delta S)}{dS} = \frac{1 - 2S}{S\sqrt{NS(1-S)}} \stackrel{!}{=} 0 \tag{A.5}$$

and therefore $S = 0.5$. This means, that the width of the central region $2E_S$ should be chosen such, that the S-parameter values of a series of measurements are roughly 0.5 in order to obtain a maximum accuracy.

B The statistical error in CDBS-measurements

Let $N_{\mathrm{h,i}}$ be the number of counts in channel i of the spectrum h with $\mathrm{h} = 1, 2$. The ratio of counts in channel i in the CDB spectrum is then given as

$$N_{\mathrm{ratio,i}} = \frac{xN_{1,\mathrm{i}}}{N_{2,\mathrm{i}}} \ , \tag{B.1}$$

where x stands for the normalization factor to equal area of the 511 keV annihilation peak:

$$x = \frac{N_{2,\mathrm{tot}}}{N_{1,\mathrm{tot}}} = \frac{\sum\limits_{\mathrm{j}\neq\mathrm{i}} N_{2,\mathrm{j}} + N_{2,\mathrm{i}}}{\sum\limits_{\mathrm{j}\neq\mathrm{i}} N_{1,\mathrm{j}} + N_{1,\mathrm{i}}} \tag{B.2}$$

with the total number of counts $N_{\mathrm{h,tot}}$ in the spectra.
The error in each bin is then given as

$$\Delta N_{\mathrm{ratio,i}} = \sqrt{\left(\frac{dN_{\mathrm{ratio,i}}}{dN_{1,\mathrm{i}}}\right)^2 N_{\mathrm{N1,i}} + \left(\frac{dN_{\mathrm{ratio,i}}}{dN_{2,\mathrm{i}}}\right)^2 N_{2,\mathrm{i}}} \tag{B.3}$$

with the derivatives

$$\frac{dN_{\mathrm{ratio,i}}}{dN_{1,\mathrm{i}}} = \frac{x}{N_{2,\mathrm{i}}}\left(1 - \frac{N_{1,\mathrm{i}}}{N_{1,\mathrm{tot}}}\right) \tag{B.4}$$

and

$$\frac{dN_{\mathrm{ratio,i}}}{dN_{2,\mathrm{i}}} = \frac{N_{1,\mathrm{i}}}{N_{1,\mathrm{tot}}}\left(\frac{1}{N_{2,\mathrm{i}}} - \frac{N_{2,\mathrm{tot}}}{N_{2,\mathrm{i}}^2}\right) \ . \tag{B.5}$$

It consequently amounts to

$$\Delta N_{\mathrm{ratio,i}} = \sqrt{\frac{x^2}{N_{2,\mathrm{i}}^2}\left(1-\frac{N_{1,\mathrm{i}}}{N_{1,\mathrm{tot}}}\right)^2 N_{1,\mathrm{i}} + \frac{N_{1,\mathrm{i}}^2}{N_{1,\mathrm{tot}}^2}\left(\frac{1}{N_{2,\mathrm{i}}}-\frac{N_{2,\mathrm{tot}}}{N_{2,\mathrm{i}}^2}\right)^2 N_{2,\mathrm{i}}}\ . \tag{B.6}$$

Acknowledgments

In the first place I would like to thank Dr. Christoph Hugenschmidt for his confidence in my doings and his continuous support. The door to his office was always open and he gave me the feeling that I can count on his impressing competence and help everytime. His outstanding commitment concerning the projects in the positron group and the very enjoyable and highly motivating atmosphere were invaluable for my work and this thesis. He has the impressing ability to have fun and to laugh even in challenging situations.
Furthermore, I would like to thank Prof. Dr. Klaus Schreckenbach for the support and the backing of this work. He gave me crucial hints and advices in many fruitful discussions and I especially would like to thank him for his profound knowledge about how to publish in refereed journals. He read the manuscript for the publication in Phys. Rev. many times and gave me countless helpful and important hints and remarks.
Prof. Dr. Peter Böni supported me financially during the first year of my work as a graduate student. I am very thankful for this invaluable support since he made the beginning of it possible. He impressed me with his high competence and the very friendly atmosphere he managed to create in the E21-group. It was a great joy to discuss with him physical topics and to work for E21.
Many parts for the CDBS2 have been bought with the funding from FRM-II and therefore I would like to thank its administration for the money they gave me. Especially the new HPGe-detectors helped a lot.
The extremely enjoyable and friendly atmosphere in the positron group had a very balancing effect on me. I really liked to work with my colleagues Thomas Brunner, Stefan Legl, Benjamin Löwe, Jakob Mayer, Christian Piochacz and Philip Pikart. We had so much fun during work and I knew that they are always open to my problems. I got the feeling that I can count on them and I am sure that there are not many physics groups with a comparable good atmosphere. Many thanks for the funny time we had! I especially would like to thank Jakob, Christian and Philip for proofreading the manuscript of this work and for their help with my Tex-Problems.
Special thanks also to Reinhard Repper who managed to solve every mechanical problem within a very short time. His unbelievable experience and his helpfulness where extremely important for the setting up of the new spectrometer. The CDBS2

definitely would not have been set up in such a short time without him. Thanks a lot!
Besonders möchte ich auch den Leuten der Herzog-Werkstatt danken, allen voran Christian Herzog, der, auch wenn die Werkstatt ausgebucht war, schnell und unkompliziert meine Teile dazwischen schob. Michael Fuß, Andreas Scharl, Robert Schlecht, Mario Tessaro und Andreas Huber danke ich für die immer freundliche Atmosphäre in der Werkstatt. Ich habe in der ganzen Zeit nie gehört, dass etwas nicht geht, was mich sehr beeindruckt hat. Außerdem möchte ich Herrn Manfred Pfaller stellvertretend für das Team der Zentralwerkstatt danken, da sie immer schnell alle Probleme gekonnt gelöst und die Probenkammer sowie den Probenhalter des CDBS2 äußerst genau angefertigt haben.
I also would like to thank Dr. Manfred Friedrich and his team from the FZR Rossendorf in Dresden for making the 3 MeV Tandetron available and for their very helpful support during the beam time. Furthermore, I gratefully acknowledge the work of Dr. Matz Haaks from the HISKP in Bonn. His S-parameter analyzing tool MSPEC and the projection obtaining program MSPEC2D saved a lot of time and he always changed the program according to our demands. Many thanks!
Werner Egger has to be gratefully acknowledged for preliminary measurements of the ion-irradiated Mg-samples at PLEPS.
The working students Timo Buttler, Joe Duris and Adele Schwab helped me a lot with my work. Adele developed a γ-scanning stage, Joe managed to deal with COMSOL and Timo helped me with designing the detector mountings for the CDBS2. I wish you good luck for your future career and thanks again!
Meinem Bruder Wolfgang und seiner Freundin Steffi möchte ich für unser sehr gutes Verhältnis danken.
Zu guter letzt bin ich meinen lieben Eltern zu Dank verpflichtet, ohne deren Unterstützung und Ermutigung mein Studium undenkbar gewesen wäre. Sie haben die Fertigstellung dieser Arbeit leider nicht mehr erlebt, obwohl genau das ihr größter Wunsch gewesen ist. Meine Dankbarkeit für ihre Hilfe über all die Jahre lassen sich nicht in Worte fassen. Ich vermisse sie sehr und werde die Erinnerung an sie für immer in mir tragen.

Bibliography

[1] A. Dupasquier and A. P. Mills. *Positron Spectroscopy of Solids*. IOS Press, Amsterdam, 1995.

[2] R. N. West. Positron studies of condensed matter. *Adv. Phys.*, 22:263, 1973.

[3] M. J. Puska and R. M. Nieminen. Theory of positrons in solids and on solid surfaces. *Rev. Mod. Phys.*, 66:841, 1994.

[4] P. J. Schultz and K. G. Lynn. Interaction of positron beams with surfaces, thin films, and interfaces. *Rev. Mod. Phys.*, 60:701, 1988.

[5] T. E. Jackman, C. W. Schulte, J. L. Campbell, P. C. Lichtenberger, I. K. MacKenzie, and M. R. Wormald. Positron annihilation gamma ray lineshapes in metals. *J. Phys. F: Metal Phys.*, 4:L1, 1974.

[6] R. Krause-Rehberg and H. S. Leipner. *Positron Annihilation in Semiconductors*, page 16. Springer-Verlag Berlin, Heidelberg, 1999.

[7] Werner Brandt and Irwin Spirn. Positron lifetime spectra in molecular substances. *Phys. Rev.*, 142(1):231–237, Feb 1966.

[8] M. Alatalo, H. Kauppinen, K. Saarinen, M. J. Puska, J. Mäkinen, P. Hautojärvi, and R. M. Nieminen. Identification of vacancy defects in compound semiconductors by core-electron annihilation: Application to InP. *Phys. Rev. B*, 51(7):4176–4185, Feb 1995.

[9] P. Asoka-Kumar, M. Alatalo, V. J. Ghosh, A. C. Kruseman, B. Nielsen, and K. G. Lynn. Increased elemental specificity of positron annihilation spectra. *Phys. Rev. Lett.*, 77(10):2097–2100, Sep 1996.

[10] J. Kuriplach, A. L. Morales, C. Dauwe, D. Segers, and M. Šob. Vacancies and vacancy-oxygen complexes in silicon: Positron annihilation with core electrons. *Phys. Rev. B*, 58(16):10475–10483, Oct 1998.

[11] Y. Nagai, Z. Tang, M. Hassegawa, T. Kanai, and M. Saneyasu. Irradiation-induced cu aggregations in fe: An origin of embrittlement of reactor pressure vessel steels. *Phys. Rev. B*, 63:134110, 2001.

[12] Y. Nagai, T. Toyama, Z. Tang, M. Hasegawa, S. Yanagita, T. Okhubo, and K. Hono. Embedded ultrafine clusters investigated by coincidence doppler broadening spectroscopy. *Mat. Sci. For.*, 445-446:11, 2004.

[13] J. Čížek, O. Melikhova, I. Procházka, J. Kuriplach, I. Stulíkova, P. Vostrý, and J. Faltus. Annealing process in quenched al-sn alloys: A positron annihilation study. *Phys. Rev. B*, 71:064106–1, 2005.

[14] N. W. Ashcroft and N. D. Mermin. *Solid State Physics*, page 38. Saunders College Publishing, Orlando, 1976.

[15] G. P. Williams. Electron binding energies of the elements. In D. R. Lide, editor, *Handbook of Chemistry and Physics*, pages 10–205. CRC Press LLC, Boca Raton, 84 edition, 2003.

[16] C. Hugenschmidt, G. Kögel, R. Repper, K. Schreckenbach, P. Sperr, B. Straßer, and W. Triftshäuser. The neutron induced positron source at munich-nepomuc. *Nucl. Instr. Meth. B*, 221:160, 2004.

[17] M. Stadlbauer. Aufbau eines ortsauflösenden Doppler-Koinzidenzspektrometers zur Untersuchung der Positronenzerstrahlung in Festkörpern. Diplomathesis, TU München, 2004.

[18] M. Stadlbauer, C. Hugenschmidt, C. Piochacz, B. Straßer, and K. Schreckenbach. Spatially resolved investigation of thermally treated brass with a coincident Doppler broadening spectrometer. *Appl. Surf. Sci.*, 252:3269, 2006.

[19] P. A. M. Dirac. A theory of electrons and protons. *Proc. Roy. Soc.*, A126:360, 1930.

[20] Carl D. Anderson. The positive electron. *Phys. Rev.*, 43(6):491–494, Mar 1933.

[21] Carl D. Anderson. Energies of cosmic-ray particles. *Phys. Rev.*, 41(4):405–421, Aug 1932.

[22] C. D. Anderson. The apparent existence of easily deflectable positives. *Science*, 76:238, 1932.

[23] Thomas Beier, Hartmut Häffner, Nikolaus Hermanspahn, Savely G. Karshenboim, H.-Jürgen Kluge, Wolfgang Quint, Stefan Stahl, José Verdú, and Günther Werth. New determination of the electron's mass. *Phys. Rev. Lett.*, 88(1):011603, Dec 2001.

[24] `http://physics.nist.gov/cgi-bin/cuu/Value?eqmec2mev|search_for=electron+mass`.

[25] H. Pilkuhn. *Properties and Production Spectra of Elementary Particles*, volume 6 of *Landolt-Börnstein - Group I Elementary Particles, Nuclei and Atoms*. Springer-Verlag, 1972.

[26] E. Bellotti, M. Corti, E. Fiorini, C. Liguori, A. Pullia, A. Sarracino, P. Sverzellati, and L. Zanotti. A new experimental limit on electron stability. *Physics Letters B*, 124:435, 1983.

[27] R. A. Ferrell. Theory of positron annihilation in solids. *Rev. Mod. Phys.*, 28(3):308, Jul 1956.

[28] A. Ishii. Theory of positronium formation at metal surfaces. *Phys. Rev. B*, 36(4):1853, Aug 1987.

[29] A. Rich. Recent experimental advances in positronium research. *Rev. Mod. Phys.*, 53(1):127, Jan 1981.

[30] C. Hugenschmidt, K. Schreckenbach, M. Stadlbauer, and B. Straßer. Low-energy positrons of high intensity at the new positron beam facility NEPOMUC. *Nucl. Instr. Meth. A*, 554:384–391, 2005.

[31] A. Perkins and J. P. Carbotte. Effect of the positron-phonon interaction on positron motion. *Phys. Rev. B*, 1(1):101, Jan 1970.

[32] J. Oliva. Inelastic positron scattering in an electron gas. *Phys. Rev. B*, 21(11):4909, Jun 1980.

[33] A. F. Makhov. *Sov. Phys. Solid State*, 2:1934, 1961.

[34] S. Valkealahti and R. M. Nieminen. Monte carlo calculations of kev electron and positron slowing down in solids. *Appl. Phys. A*, 35:51, 1984.

[35] J. Bardeen and W. Shockley. Deformation potentials and mobilities in non-polar crystals. *Phys. Rev.*, 80(1):72, Oct 1950.

[36] B. Bergersen, E. Pajanne, P. Kubica, M. J. Stott, and C. H. Hodges. Positron diffusion in metals. *Solid Sate Commun.*, 15:1377, 1974.

[37] M. Bertolaccini, A. Bisi, G. Gambarini, and L. Zappa. Positron states in ionic media. *Journal of Physics C: Solid State Physics*, 4(6):734–745, 1971.

[38] R. M. Nieminen and M. Manninen. In P. Hautojärvi, editor, *Positrons in Soilds*, number 12 in Topics in current physics, page 145. Springer-Verlag, Berlin, 1979.

[39] G. Kögel, D. Schödlbauer, W. Triftshäuser, and J. Winter. Investigation of micropores in amorphous hydrogenated carbon by a pulsed positron beam. *Phys. Rev. Lett.*, 60(15):1550–1553, Apr 1988.

[40] D. W. Gidley, A. Rich, E. Sweetman, and D. West. New precision measurements of the decay rates of singlet and triplet positronium. *Phys. Rev. Lett.*, 49(8):525–528, Aug 1982.

[41] G. Schatz and A. Weidinger. *Nukleare Festkörperphysik*. B. G. Teubner Stuttgart, 1997.

[42] W. Puff. The influence of several parameters on the lifetimes and intensities of positron lifetime spectra of metals. *Appl. Phys. A*, 18:165, 1979.

[43] M. Eldrup, Y. M. Huang, and B. T. A. McKee. Estimates of uncertainties in analysis of positron lifetime spectra for metals. *Appl. Phys. B*, 15:65, 1978.

[44] T. E. M. Staab, B. Somieski, and R. Krause-Rehberg. The data treatment influence on the spectra decomposition in positron lifetime spectroscopy part 2: The effect of source corrections. *Nucl. Instr. Meth. A*, 381:141, 1996.

[45] P. Willutzki, J. Störmer, G. Kögel, P. Sperr, D. T. Britton, R. Steindl, and W. Triftshäuser. An improved pulsed low-energy positron system. *Meas. Sci. Technol.*, 5:548, 1994.

[46] A. v. Veen, H. Schut, and P. E. Mijnarends. Depth profiling of subsurface regions, interfaces and thin films. In P. Coleman, editor, *Positron Beams*, chapter 6.2, page 198. World Scientific Publishing Co. Pte. Ltd., 1 edition, 2000.

[47] R. N. West. In A. Dupasquier and A. P. Mills, editors, *Positron spectroscopy of solids*, page 75. IOS, Amsterdam, 1995.

[48] P. G. Coleman. The generation and transport of positron beams. In P. G. Coleman, editor, *Positron beams*, chapter 2.2, page 17. Word Scientific Publishing Co. Pte. Ltd., 2000.

[49] H. M. Weng, Y. F. Hu, C. D. Beling, and S. Fung. An apparatus used to make 22na sources for use in low-energy positron beams. *Appl. Surf. Sci.*, 116:98, 1997.

[50] B. Straßer. *Aufbau einer Anlage zur positroneninduzierten Auger-Elektronenspektroskopie*. Dissertation, TU München, 2001.

[51] J. R. Oppenheimer and M. S. Plesset. On the production of the positive electron. *Phys. Rev.*, 44(1):53, Jul 1933.

[52] C. M. Davisson. Interaction of gamma-radiation with matter. In K. Siegbahn, editor, *Beta- and gamma ray spectroscopy*, chapter 2, page 45. Interscience Publishers Inc., 1 edition, 1955.

[53] W. Stoeffl, P. Asoka-Kumar, and R. Howell. The positron microprobe at llnl. *Appl. Surf. Sci.*, 149:1, 1999.

[54] R. Krause-Rehberg, S. Sachert, G. Brauer, A. Rogov, and K. Noack. Epos– an intense positron beam project at the elbe radiation source in rossendorf. *Appl. Surf. Sci.*, 252:3106, 2006.

[55] A. v. Veen, F. Labohm, H. Schut, J. de Roode, T. Heijenga, and P.E. Mijnarends. Testing of a nuclear-reactor-based positron beam. *Appl. Surf. Sci.*, 116:39, 1997.

[56] B. Krusche and K. Schreckenbach. Intense positron sources by pair creation with neutron capture y-rays. *Nucl. Instr. Meth. A*, 295:155, 1990.

[57] C. Hugenschmidt, G. Kögel, R. Repper, K. Schreckenbach, P. Sperr, and W. Triftshäuser. First platinum moderated positron beam based on neutron capture. *Nucl. Instr. Meth. B*, 198:220, 2002.

[58] D. M. Chen, K. G. Lynn, R. Pareja, and B. Nielsen. Measurement of positron reemission from thin single-crystal W(100) films. *Phys. Rev. B*, 31(7):4123, Apr 1985.

[59] A. P. Mills. Efficient generation of low-energy positrons. *Appl. Phys. Lett.*, 35:427, 1979.

[60] C. Piochacz. Entwicklung und Aufbau eines Transmissionsremoderators für Positronen. Diplomarbeit, TU München, 2005.

[61] C. Piochacz, G. Kögel, W. Egger, C. Hugenschmidt, J. Mayer, K. Schreckenbach, P. Sperr, M. Stadlbauer, and G. Dollinger. Positron remoderator for the high intensity positron source NEPOMUC. *submitted to Appl. Sur. Sci*, 2007.

[62] B. Löwe, K. Schreckenbach, and C. Hugenschmidt. Gas moderation of positrons. *submitted to Appl. Surf. Sci.*, 2007.

[63] C. Hugenschmidt, G. Kögel, R. Repper, K. Schreckenbach, P. Sperr, B. Straßer, and W. Triftshäuser. Intense positron source at the munich research reactor frm-ii. *Appl. Phys. A*, 74:S295, 2002.

[64] C. Hugenschmidt, G. Kögel, R. Repper, K. Schreckenbach, P. Sperr, B. Straßer, and W. Triftshäuser. Monoenergetic positron beam at the reactor based positron source at frm-ii. *Nucl. Instr. Neth B*, 192:97, 2002.

[65] C. Hugenschmidt, T. Brunner, S. Legl, J. Mayer, C. Piochacz, M. Stadlbauer, and K. Schreckenbach. Positron experiments at the new positron beam facility NEPOMUC at FRM-II. *Phys. Stat. Sol.*, 4:3947, 2007.

[66] H. Stöcker. *Taschenbuch der Physik*. Harri Deutsch, 1998.

[67] K. O. Jensen and A. Weiss. Theoretical study of the application of positron-induced auger-electron spectroscopy. *Phys. Rev. B*, 41(7):3928, 1990.

[68] Z. Tang, M. Hasegawa, Y. Nagai, and M Saito. Density functional study on metastable bcc copper: Electronic structure and momentum density of positron-electron pairs. *Phys. Rev. B*, 65(19):195108, Apr 2002.

[69] G. F. Knoll. *Radiation detection and measurement*, chapter 11, page 355. John Wiley & Sons, Inc., 2000.

[70] G. F. Knoll. *Radiation detection and measurement*, chapter 12, page 405. John Wiley & Sons, Inc., 2000.

[71] A. v. Veen, H. Schut, and P. E. Mijnarends. Depth profiling of subsurface regions, interfaces and films. In P Coleman, editor, *Positron beams and their applications*, page 194. World Scientific, London, 2000.

[72] Performance of digital signal processors for gamma spectrometry. Application note, Canberra Industries, 1997.

[73] `http://www.iskp.uni-bonn.de/gruppen/material/software/software.php`.

[74] M. Haaks, T. E. M. Staab, and K. Maier. Analyzing the high-momentum part of positron annihilation doppler spectra with a single germanium detector. *Nucl. Instr. Meth. A*, 569:829, 2006.

[75] A. Calloni, A. Dupasquier, R. Ferragut, P. Folegati, and M. M. Iglesias. Positron localization effects on the doppler broadening of the annihilation line: Aluminum as a case study. *Phys. Rev. B*, 72:054112–1, 2005.

[76] M. Stadlbauer, C. Hugenschmidt, K. Schreckenbach, and P. Böni. Investigation of the chemical vicinity of crystal defects in ion-irradiated Mg and a Mg-Al-Zn alloy with coincident Doppler broadening spectroscopy. *Phys. Rev. B*, 76:174104, 2007.

[77] P. Folegati, I. Makkonen, R. Ferragut, and M. J. Puska. Analysis of electron-positron momentum spectra of metallic alloys as supported by first-principles calculations. *Phys. Rev. B*, 75:054201–1, 2007.

[78] P. Folegati, 2007. private communication.

[79] M. J. Koskelo, I. J. Koskelo, and B. Sielaff. Comparison of analog and digital signal processing systems using pulsers. *Nucl. Instr. Meth. A*, 422:373, 1999.

[80] `www.fastcomtec.com`.

[81] `www.simion.com`.

[82] M. Stadlbauer, C. Hugenschmidt, and K. Schreckenbach. Characterization of the chemical vicinity of open volume defects in magnesium and AZ31 with coincident Doppler broadening spectroscopy. *Phys. Stat. Sol.*, 4:3489, 2007.

[83] G. M. Hood. Comments on positron annihilation and the vacancy properties of mg. *Phys. Rev. B*, 26:1036, 1982.

[84] A. Seeger. Investigation of point defects in equilibrium concentrations with particular reference to positron annihilation techniques. *J. Phys. F: Metal Phys.*, 3:248, 1973.

[85] L. D. Landau and E. M. Lifschitz. *Klassische Feldtheorie*, chapter III, page 64. Akademie-Verlag Berlin, 1973.

[86] `www.femlab.com`.

[87] M. W. Wolfmeyer and J. W. Dillinger. The thermal conductivity of sapphire between 0.4 and 4 K. *Phys. Lett. A*, 34:247, 1971.

[88] `http://www.shicryogenics.com/index.php?option=com_content&task=view&id=95&Itemid=248`.

[89] `http://www.geratherm.de/de/technologie_galinstan`.

[90] A. David, G. Kögel, P. Sperr, and W. Triftshäuser. Lifetime measurements with a scanning positron microscope. *Phys. Rev. Lett.*, 87(6):067402, Jul 2001.

[91] P. Skubisz, J. Sinczak, and S. Bednarek. Forgeability of Mg-Al-Zn magnesium alloys in hot and warm closed die forging. *J. Mat. Proc. Tech.*, 177:210, 2005.

[92] D. Segers, M. Dorikens, and L. Dorikens-Vanpraet. Evidence for positron trapping in magnesium from Dopplerbroadening measurements. *Sol. Stat. Comm.*, 36:943, 1980.

[93] J. S. Williams. Materials modification with ion beams. *Rep. Prog. Phys.*, 49:491, 1986.

[94] P. Erhart. In H. Ullmaier, editor, *Landolt-Börnstein - Atomic defects in metals*, volume III/25, page 274. Springer Verlag Berlin, Heidelberg, 1991.

[95] W. Buchmann. *Magnesium und seine Legierungen*, page 155. Springer-Verlag Berlin Heidelberg New York, 2nd edition, 1939.

[96] F. Pravdic, H. Kilian, M. Brandecker, C. Woegere, and G. Traxler. The grain size evolution of az31 profiles as a function of different casting conditions. *Mat. Sci. For.*, 488-489:349, 2005.

[97] M. T. Perez-Prado and O. A. Ruano. Texture evolution during annealing of magnesium az31 alloy. *Scripta Mat.*, pages 149–155, 2002.

[98] M Friedrich, W Bürger, D Henke, and S. Turuc. The rossendorf 3 mv tandetron: a new generation of high-energy implanters. *Nucl. Instr. Meth. A*, 382:357, 1996.

[99] J. F. Ziegler. Srim-2003. *Nucl. Instr. Meth. B*, 219-220:1027, 2004.

[100] A. v. Veen, H. Schut, and P. E. Mijnarends. Depth profiling of subsurface regions, interfaces and films. In P Coleman, editor, *Positron beams and their applications*, page 191. World Scientific, London, 2000.

[101] P. Hautojärvi, J. Johansson, A. Vehanen, J. Yli-Kauppilla, J. Hillairet, and P. Tzanetakis. Trapping of positrons at vacancies in magnesium. *Appl. Phys. A*, 27:49, 1981.

[102] W. Bauer-Kugelmann, P. Sperr, G. Kögel, and W. Triftshäuser. Latest version of the munich pulsed low energy positron system. *Mat. Sci. For.*, 363-365:529, 2001.

List of publications

- M. Stadlbauer, C. Hugenschmidt, and K. Schreckenbach. New design of the CDB-spectrometer at NEPOMUC for T-dependent defect spectroscopy in Mg. *Appl. Surf. Sci.*, accepted, 2008

- C. Hugenschmidt, P. Pikart, M. Stadlbauer, and K. Schreckenbach. High elemental selectivity to Sn submonolayers embedded in Al using positron annihilation spectroscopy. *Phys. Rev. B*, accepted, 2008

- M. Stadlbauer, C. Hugenschmidt, K. Schreckenbach, and P. Böni. Investigation of the chemical vicinity of crystal defects in ion-irradiated Mg and a Mg-Al-Zn alloy with coincident Doppler broadening spectroscopy. *Phys. Rev. B*, 76:174104, 2007.

- M. Stadlbauer, C. Hugenschmidt, and K. Schreckenbach. Characterization of the chemical vicinity of open volume defects in magnesium and AZ31 with coincident Doppler broadening spectroscopy. *Phys. Stat. Sol.*, 4:3489, 2007.

- C. Hugenschmidt, J. Mayer, and M. Stadlbauer. Investigation of the near surface region of chemically treated and Al-coated PMMA by Doppler broadening spectroscopy. *Radiat. Phys. Chem.*, 76:217, 2007.

- P. Pikart, c. Hugenschmidt, J. Mayer, M. Stadlbauer, and K. Schreckenbach. Depth resolved Doppler broadening measurements of layered Al-Sn-samples. *Appl. Surf. Sci.*, accepted, 2007.

- C. Piochacz, G. Kögel, W. Egger, C. Hugenschmidt, J. Mayer, K. Schreckenbach, P. Sperr, M. Stadlbauer, and G. Dollinger. Positron remoderator for the high intensity positron source NEPOMUC. *Appl. Surf. Sci.*, accepted, 2007.

- C. Hugenschmidt, T. Brunner, S. Legl, J. Mayer, C. Piochacz, M. Stadlbauer, and K. Schreckenbach. Positron experiments at the new positron beam facility NEPOMUC at FRM-II. *Phys. Stat. Sol.*, 4:3947, 2007.

- C. Hugenschmidt, K. Schreckenbach, M. Stadlbauer, and B. Straßer. First positron experiments at NEPOMUC. *Appl. Surf. Sci.*, 252:3098, 2006.
- S. Mühlbauer, P. Böni, U. Filges, C. Schanzer, M. Stadlbauer, and J. Stahn. Performance of an elliptically tapered neutron guide. *Physica B*, 385:1247, 2006.
- M. Stadlbauer, C. Hugenschmidt, C. Piochacz, B. Straßer, and K. Schreckenbach. Spatially resolved investigation of thermally treated brass with a coincident Doppler broadening spectrometer. *Appl. Surf. Sci*, 252:3269, 2006.
- C. Hugenschmidt, K. Schreckenbach, M. Stadlbauer, and B. Straßer. Low energy positrons of high intensity at the new positron beam facility NEPOMUC. *Nucl. Instr. Meth. A*, 554(1-3):384, 2005.